Study of thermomechanical couplings in nanostructured superelastic nickel-titanium wires

Henrique Martinni Ramos de Oliveira

Communauté
UNIVERSITÉ Grenoble Alpes

THÈSE

Pour obtenir le grade de

DOCTEUR DE LA COMMUNAUTE UNIVERSITE GRENOBLE ALPES

Spécialité :**Matériaux, Mécanique, Génie Civil, Electrochimie**

Arrêté ministériel : 25 mai 2016

Présentée par

Henrique MARTINNI RAMOS DE OLIVEIRA

Thèse dirigée par **Denis FAVIER, Professeur ,Université Grenoble Alpes**, et
codirigée par **Hervé LOUCHE, Professeur, Université de Montpellier**

préparée au sein du **Laboratoire TIMC-IMAG**
dans **l'École Doctorale IMEP2 : Ingénierie Matériaux Mécanique, Environnement, Energétique, Procédés, Production**

Etude des couplages thermomécaniques dans des fils super-élastiques nanostructurés nickel-titane

Study of thermomechanical couplings in nanostructured superelastic nickel-titanium wires

Thèse soutenue publiquement le **« 5 octobre 2018 »**,
devant le jury composé de :

M. Jean-Benoît LECAM
Professeur Université de Rennes 1 (Président)
Mme. Shabnam ARBAB CHIRANI
Professeur, Ecole Nationale d'Ingénieurs de Brest (Rapporteur)
M. Xavier BALANDRAUD
Professeur, Institut Pascal, Clermont-Ferrand (Rapporteur)
M. Nathanael CONNESSON
Maitre de Conférences, Université Grenoble Alpes (Examinateur)
M. Denis FAVIER
Professeur Université Grenoble Alpes (Directeur de thèse)
M. Hervé LOUCHE
Professeur Université Montpellier (Co-Directeur)

Study of thermomechanical couplings in nanostructured superelastic nickel-titanium wires

Henrique Martinni Ramos de Oliveira

December 28, 2018

ACKNOWLEDGEMENTS

I would like to address my deep gratitude to my supervisors Prof. Denis Favier and Prof. Herve Louche for always being available to discuss and explain things clearly. With their patience, enthusiasm and inspiration, they guided me through this thesis, which was a big challenge for me. I would like to thank to the thesis committee members, Prof. Shabnam Arbab Chirani, Xavier Balandraud and Jean-Benoit Lecam for taking time to read this thesis manuscript.

I also want to thank my friends from team BioMMat (Christopher, Quentin, Guilherme, Francois, Gabriel, Ali, Yves, Vincent, Thierry, Gregory, Nathanael, Ana, Anais, Mohammed, Khouloud, Maxime and Edouard) for providing a great stimulating and fun environment through these years. I would like to give special thanks to some of them: to Chris, for being always available and providing information about everything, really everything. To Quentin, for his company and knowledge, from which I also learned a lot of French expressions and vocabulary. To Thierry, for being always available to discuss my endless doubts about everything and for teaching me to climb. To Ali, for all the discussions and time we spent in the lab and also for his availability and kindness when receiving me at his home in Iran. To Greg, for his kindness and advices through these years. I would like to especially thank Prof. Carlos Jose de Araujo, who was my advisor in Federal University of Campina Grande in Brazil during my master degree. I had a great experience working with him and it was thanks to his advices and encouragement that I came to do my thesis in France.

I would specially thank my love, Estephanie, for being always present and with whom I could discuss about my thesis, my personal dilemmas, my doubts about martensite transformation, kitesurf, bike, snowboard, etc. She gave me extra strength and made me a happier person in every moment. I would like to thank my entire family for providing a loving environment for me. Firstly to my parents Jose Nilton de Oliveira and Maria de Fatima Ramos de Oliveira, for their unconditional love and for believing in me. Not with all words in the world I could describe my love and gratitude to them. To my sister Silva Ramos de Oliveira, for her support and presence. And last but not least, to my cousins, uncles and aunts, Davidson, Luma, Caique, Tales, Tulio, Salete, Cristovao, Guia, Albert Einstein, Terezinha, Neto, Vandui and Luis Carlos, each with their own way of supporting me.

This thesis was funded with the support of CNPq, National Council of Scientific and Technological Development - Brazil.

RESUME

Cette thèse est une étude expérimentale du comportement thermo-mécanique superélastique d'un fil nanocristallin $Ti-50.9\,at.\%\,Ni$ en alliage à mémoire de forme (SMA) (diamètre 0.5 mm), après subir un cold work (CW). Les AMF sont capables d'induire des changements de température importants lorsqu'ils sont chargés mécaniquement. Ce phénomène est dû à un important couplage thermomécanique présent dans cette transformation de phase solide entre les phases Austénite (A) et Martensite (M). La chaleur latente par unité de masse (ΔH) tout au long de la transformation de phase est l'énergie responsable de cette variation de température. La détermination de ΔH est généralement effectuée par calorimétrie à balayage différentiel (DSC). Cependant, pour les SMA nanocristallins, les résultats DSC obtenus ne sont pas concluants sur la détermination de cette propriété.

Dans ce travail, une méthode utilisant la corrélation d'image numérique (DIC) et les mesures de champ thermique (TFM) a été utilisée pour analyser les couplages thermomécaniques lors d'une transformation de phase induite par contrainte. Des champs cinématiques et thermiques ont été acquis lors d'essais de traction superélastiques réalisés sur des fils CW NiTi soumis à différentes températures de traitements thermiques (TTT) allant de 523 à 598 K pendant 30 min. Un tel traitement thermique à basse température favorise une boucle totalement superélastique sans plateau de contrainte et sans déformation de type Lüders. En supposant un modèle thermique uniforme, les sources de chaleur impliquées lors du chargement cyclique ont été estimées. Cette puissance thermique par unité de masse a été comparée à la puissance mécanique et intégrée au fil du temps pour obtenir l'équilibre énergétique. De plus, grâce à une analyse thermodynamique basée sur l'énergie libre de Gibbs, les valeurs de ΔH, ainsi que la fraction de martensite, ont été estimées au cours des transformations de phase A-M directe et inverse M-A. L'analyse des résultats a conduit aux conclusions suivantes: (1) Les puissances et énergies thermiques et mécaniques présentaient une dépendance significative vis-à-vis du TTT. (2) Malgré l'effet important des valeurs du TTT sur les réponses mécaniques et thermiques, les ΔH obtenues étaient très proches pour tous les TTT et dans la même gamme de valeurs fondée dans la littérature pour un alliage $Ti-50.9\,at.\%\,Ni$ entièrement recuit testé par technique DSC. (3) Pour une deformation donnée, la fraction de martensite augmente avec l'augmentation de TTT. (4) Pour une contrainte imposée de 4,5%, la fraction de martensite augmente de 30% à 40% en augmentant le TTT de 523K à 598K.

Mots clefs: *Mesure des champs cinématique et thermique, fils nanostructurées NiTi, puissances thermiques et mécaniques, chaleur latente spécifique, fraction martensitique.*

ABSTRACT

This PhD thesis is an experimental study of the thermomechanical superelastic behaviour of a $Ti - 50.9\,at.\%\,Ni$ Shape Memory Alloy (SMA) nanocrystalline thin wire (diameter 0.5 mm), in a Cold Worked (CW) state. SMAs are capable of inducing important temperature change when they are mechanically loaded. This phenomenon is due to an important thermomechanical coupling present in this solid phase transformation between Austenite (A) and Martensite (M) phases. The latent heat per unit of mass (ΔH) throughout the phase transformation is the energy responsible of this temperature variation. The determination of ΔH is generally performed by differential scanning calorimetry (DSC). However, for nanocrystalline SMAs, the obtained DSC results are non conclusive on the determination of this property.

In this work, a method using digital image correlation (DIC) and thermal field measurements (TFM) was used to analyze the thermomechanical couplings during a stress induced phase transformation (SIPT). Kinematics and thermal full fields were acquired during superelastic tensile tests performed on the CW NiTi wire submitted to different heat treatments temperatures (HTT) ranging from 523 K to 598 K during 30 min. Such a heat treatment at low temperature promoted a fully superelastic loop without stress plateau and no Luders-like deformation. Assuming a uniform thermal model, the heat sources involved during the cyclic loading were estimated. This thermal power per unit of mass was compared to the mechanical one and integrated over the time to get energy balance. Further, through a thermodynamic analysis based on the Gibbs free energy, the values of ΔH, as well as the martensite fraction, were estimated during the forward A-M and reverse M-A phase transformations. The analysis of the results led to the following conclusions: (1) Thermal and mechanical powers and energies presented a significant dependence on the HTT. (2) Despite the strong effect of the values of the HTT on mechanical and thermal responses, the obtained ΔH were very close for all HTT and in the same range of values founded in the literature for a fully annealed $Ti - 50.9\,at.\%\,Ni$ alloy tested via DSC technique. (3) For a given strain, martensite fraction increases with increasing HTT. (4) For an imposed strain of 4.5%, the martensite fraction increases from 30% to 40% when increasing HTT from 523K to 598K.

Keywords: *Full-field kinematics and thermal measurements, nanostructured NiTi wires, thermal and mechanical powers, heat balance, specific latent heat, martensite fraction..*

Without experience nothing can be known enough. There are two ways of acquiring knowledge: by reason or by experience. Reasoning leads us to draw a conclusion that we hold for certain, but does not eliminate the doubt. And the spirit will not rest in the light of truth if it does not acquire it through experience.

Roger Bacon (1214 - 1294), Opus Majus, vol. II, p. 583.

CONTENTS

LIST OF FIGURES

LIST OF TABLES

GENERAL INTRODUCTION

The NiTi shape memory alloys (SMA) are part of a material class exhibiting particular properties like shape memory effect (SME) and superelasticity (SE). Such properties are due to a martensite phase transformation taking place in a solid state. These effects have large potential to be used in a variety of fields such as aeronautical, mechanical engineering and biomedical. Because of that, an increasing interest in the study of their thermomechanical behaviour has been recorded.

Phase transformation can be induced by temperature variations (Thermal Induced Phase Transformation - TIPT) and/or by mechanical loading (Stress Induced Phase Transformation – SIPT). The superelasticity is the result of the austenite to martensite (A-M) (or the martensite to austenite (M-A)) phase transformation when the material is mechanically loaded (or unloaded). The complete recovery of strain is achieved at the end of unloading. The classic stress – strain curve obtained during an uniaxial tensile test is a hysteretic loop with two stress plateaus: an upper stress plateau during loading and a lower one during unloading. Thanks to phase transformation, strain levels achieve up to 10% under tension.

Temperature variations are generally observed during a SIPT. They are due to the latent heat of phase transformation, positive (exothermic heat source) during A-M and negative (endothermic heat source) during M-A. These temperature variations are depending on these heat sources but also on the different parameters of the thermal problem (heat losses, geometry, etc.). The dependence of the plateau level on temperature is known as a thermomechanical coupling between the thermal and mechanical states. The Clausius Clapeyron relation, leading to a linear dependence between the transformation stress and the temperature, describes it. The temperature can then be used to change, locally, the mechanical response of a material. Another interest of this thermomechanical coupling is to obtain thermal powers (positive or negative) from a mechanical loading. Recent applications of this elastocaloric effect (Tušek et al., 2015; Pataky et al., 2015; Wu et al., 2017) of NiTi alloys for cooling systems use such mechanical to thermal energy conversion. One interest of these materials is to obtain, locally, important temperature variations in relatively short times.

The study of the thermomechanical behaviour for modeling the cooling potential, requires the knowledge of the latent heats of A-M and M-A phase transformations. Different experimental techniques have been used to measure these heats per unit of mass. The most known, but limited to TIPT is DSC (Differential Scanning Calorimetry). For example, DSC has been used to determine the latent heat of phase transformation in different NiTi alloy compositions (Frenzel et al., 2015), and in NiTi alloys submitted to

ageing heat treatments (Xiao et al., 2017). During a SIPT, calorimetric technique is a solution to obtain these energies. For example Friend and Planes 1991 measured the entropy and enthalpy of transformation in a CuZnAl SMA. Another technique, available for SIPT, is to estimate the energies form the internal heat sources. Several methods, based on different thermal models (0D, 1D or 2D), have been proposed to obtain heat source estimations from the temperature measurements of the material. They were applied to study energy balances in CuZnAl materials (Peyroux et al., 1998a; Chrysochoos et al., 1996; Balandraud et al., 2005), to study the homogeneous (Favier et al., 2007) or localized (Schlosser et al., 2007) thermomechanical behaviour of NiTi tubes, and to compare to DSC results (Delobelle, 2012).

The material studied in this PhD thesis was a commercial cold worked (CW) NiTi wire of d=0.5 mm diameter with a composition of $Ti - 50.9\,at.\%\,Ni$. The material was submitted to a heat treatment for 30 min, at different temperatures (from 523K to 598K), which were below the recrystallization temperature (623K). Such low heat treatment temperatures promotes a fully superelastic loop without stress plateau and no Luders-like deformation. In addition, according to the material fabrication history and consequently the material microstructure (amorphous or nanostructured materials), DSC tests may show inconclusive results (Ahadi and Sun, 2014; Li et al., 2008; Chang et al., 2006).

The context of this thesis is the study of the thermomechanical couplings during a SIPT of a nanocrystalline NiTi SMA. For that the objectives of this work are the following:

- To propose a method to estimate the thermal power and energy during a SIPT of a nanostructured superelastic NiTi wire.
- To investigate the thermal and mechanical energies involved in the SIPT.
- To estimate the latent heat of phase transformation during a SIPT in a material that shows inconclusive results when submitted to a DSC test.
- To calculate the martensite fraction in function of strain and stress during a SIPT.
- Finally, to study the influence of heat treatments on the latent heat of phase transformation and martensite fraction.

For that, the present thesis report is organized in four chapters:

The first chapter presents a brief bibliography on the shape memory alloys with the generalities of the mechanism of phase transformation and the consequent thermomechanical behaviour. Also, the thermomechanical coupling during superelasticity and some engineering applications are presented. A thermodynamic framework used to analyze the involved energies on the phase transformation is shown. Finally, some specificities of NiTi alloys and the influence of its crystallographic microstructure on the thermomechanical behavior is presented.

The second chapter details the experimental aspects of the set-up. The used material, the performed heat treatments and tests are first described in this chapter. Some basic elements of the full field measurements techniques, namely Digital Image Correlation (DIC) and Infrared Thermography, as well as the experimental issues of these techniques,

are presented. Data post processing used to analyze the mechanical and thermal data are also detailed in this chapter. Finally, a short investigation of the repeatability of the performed tests is presented.

The third chapter is written in a paper format ready to be submitted. It presents the first results of the thermomechanical coupling analysis on a $Ti - 50.9\,at.\%\,Ni$ cold worked wire submitted to a heat treatment of 598 K for 30 min. In this chapter, the method proposed to estimate thermal and mechanical power during a SIPT is presented. Further, using a thermodynamic framework based on the Gibbs free energy the specific, latent heat of phase transformation is determined. Also the estimation of the martensite fraction in function of strain and stress is presented and discussed.

The objective of the fourth chapter was to study the influence of the heat treatment temperature on the latent heat of phase transformation and on the martensite fraction. For that, the $Ti - 50.9\,at.\%\,Ni$ CW wire was submitted to four heat treatments at 523 K, 548 K, 573 K and 598 K for 30 min. Using the thermomechanical approach given in the previous chapter, the thermal and mechanical powers and energies associated with the SIPT, were first estimated. Then, the specific latent heat, as well as the martensite fraction in function of strain and stress, were determined and analyzed.

CHAPTER

ONE

BIBLIOGRAPHY

Contents

1.1 Shape Memory Alloys (SMA)

Shape memory alloys (SMAs) are a class of materials which presents the "ability" of recovering large amount of deformation. At "high" temperature levels the deformed material has the ability of recovering its initial form just after being stress released. This phenomenon is called Superelasticity or Superelastic effect (SE) Fig.1.1.a. At "low" temperatures, upon heating, the material also recovers its previous shape driven by a phenomenon called Shape Memory Effect (SME) as shown in Fig.1.1.b.

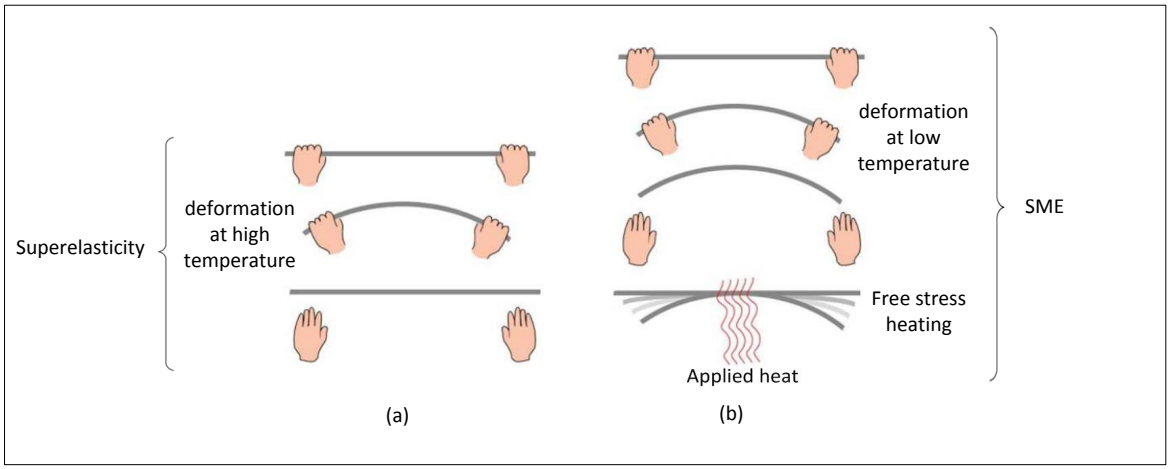

Figure 1.1: *Schematic illustration of the Superelasticity or Superelastic Effect (SE) (a), and Shape Memory Effect (SME) (b) (Adapted from Schlosser, 2008).*

These phenomena put this type of material into the class of active materials once they have the ability to respond mechanically to non-mechanical stimuli. The stimuli may be of different natures, such as thermal, electrical or magnetic. Thanks to these unique characteristics, the SMA's have been used in a large range of applications. They are present in biomedical devices (Mohd Jani et al., 2013), such as stents (Antherieu, 2016) controllable medical needle (Alonso, 2015),endodontic instruments (Arbab-Chirani et al., 2011), prosthetic devices (Chee Siong Loh et al., 2005), device for ophthalmic correction (Khmelevskaya et al., 2008); in safety devices on automotive industry (Gheorghita et al., 2013) and in active composites on aerospace industry (Yang et al., 2006)

1.1.1 Mechanism of phase transformation

The phenomena of superelasticity and shape memory effect are governed by a phase transformation between Austenite (A) and Martensite (M) phases. During phase transformation the atoms move at short distances by changing the structure of the crystalline lattice. They move cooperatively with displacement on the order of 1/10 of the inter-atomic distance. This phase transformation is characterized to be diffusionless and happens in a solid state.

On a direct phase transformation, where austenite phase transforms into martensite phase (A-M), the martensitic crystal can be created in two different structures: a self-accommodated martensite (also called twinned), which is formed shortly after the cooling of the material in the absence of applied stress; and an oriented martensite (also called detwinned), which occurs when the material, in austenite phase, undergoes the application of a stress. The reverse transformation, where the martensite transforms into austenite (M-A), can be thermally induced through heating the martensite phase, or mechanically induced by unloading the stress induced martensite. Both the direct and reverse phase transformations arise from the interaction of temperature and stress on the alloy (Leo et al., 1993). Figure 1.2 shows schematically the behaviour of the crystalline lattice when it is subjected to thermal or mechanical external stimuli.

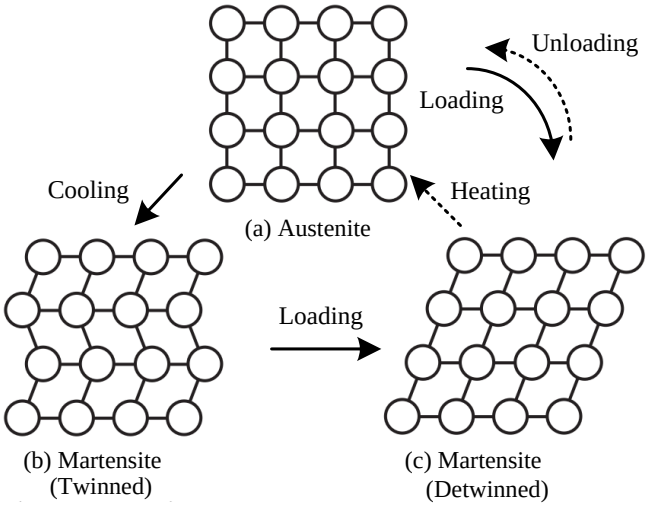

Figure 1.2: *Schematic illustration of thermal and mechanical induced phase transformation showing the (a) austenite, (b) twinned martensite and (c) detwinned martensite phases (Adapted from Cismasiu, 2010).*

1.1.2 Thermally-induced phase transformation

The temperatures responsible for the phase change are known as critical temperatures of phase transformation. In a direct thermally-induced phase transformation, the material begins to transform at the martensitic transformation start temperature (M_s) and completes its transformation when the final temperature of martensitic transformation (M_f) is reached. Similarly, in the reverse phase transformation, the material begins its transformation at the start austenitic transformation temperature (A_s) and completes it when the final austenitic transformation temperature (A_f) is achieved. In a free stress state, the austenitic structure transforms into a twinned martensite upon cooling as shown in Fig. 1.3. This mechanism is responsible for the shape memory effect.

The critical temperatures may be obtained from the analysis of physical properties as electrical resistivity, specific heat and storage modulus. Different techniques are used to

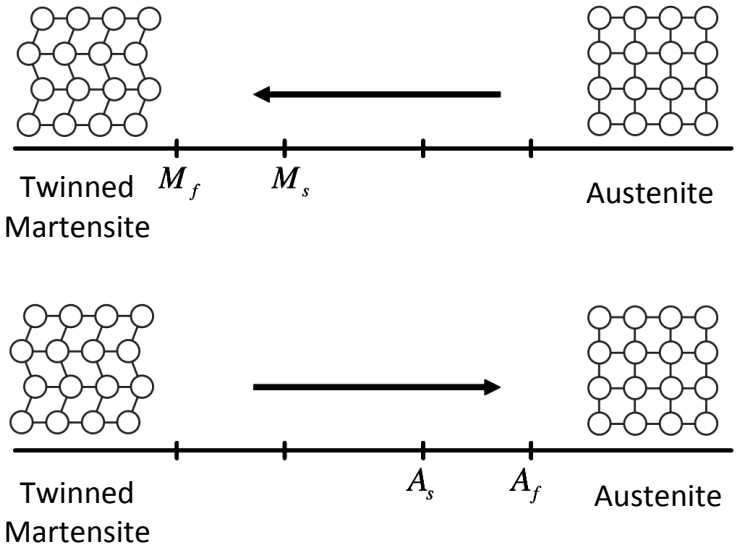

Figure 1.3: *Schematics of the thermal-induced phase transformation (adapted from Lagoudas, 2008).*

obtain these properties. Differential Scanning Calorimetry (DSC) and Dynamic Mechanical Analysis (DMA) are techniques commonly used to obtain the critical transformation temperatures through the analysis of the specific latent heat and the storage modulus, respectively.

1.1.3 Stress-induced phase transformation

The martensitic phase transformation can also be mechanically induced. With the material initially in the austenitic phase, the martensitic transformation can be initiated by mechanically loading above the critical stress of martensitic transformation (σ_{M_s}). The transformation finalizes when the final critical stress of martensitic transformation (σ_{M_f}) is achieved. Due to the reversibility nature of the phenomenon, the reverse transformation initiates at the critical starting stress of austenitic transformation (σ_{A_s}), finalizing once the final critical stress of austenitic transformation (σ_{A_f}) is reached. Figure 1.4 presents a schematic representation of this phenomenon.

The stress induced phase transformation (SIPT) is responsible for the superelastic effect, which generates macroscopic deformation during the loading with a subsequent recovery upon unloading. This behavior takes place at sufficiently high temperatures where the austenite phase is stable, i.e. above A_f.

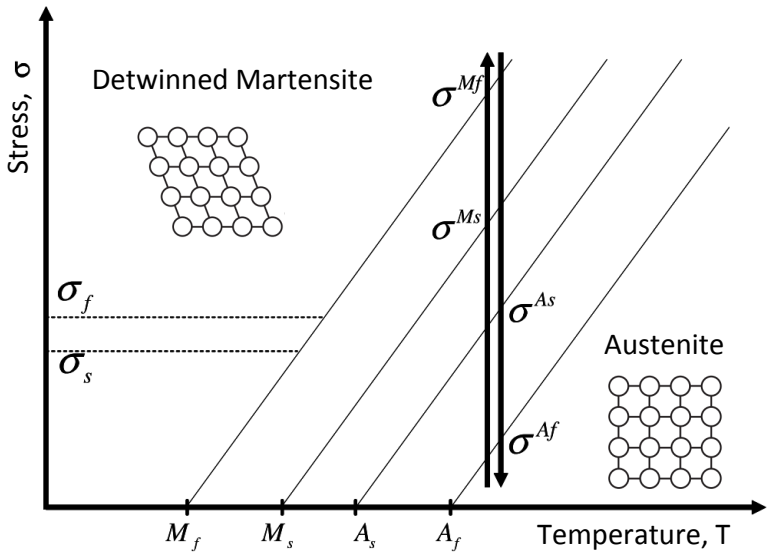

Figure 1.4: *Schematics of the stress-induced phase transformation (adapted from Lagoudas, 2008).*

1.1.4 Shape Memory Effect

Shape memory effect occurs when the SMA is deformed at a temperature below M_f while the material presents a twinned martensitic structure. The imposed deformation promotes the formation of a detwinned martensite structure which can be further reversely transformed to austenite upon heating.

Figure 1.5 presents in detail a schematic representation of the shape memory effect with its characteristic mechanical behavior. Starting from the austenite phase (point A in Fig. 1.5), when cooled in a stress-free state the material transforms into twinned martensite phase (point B) after reaching a temperature below M_f. Upon loading, the twinned martensitic structure starts its detwinning process at (σ_s) with the growth of favorably oriented martensite variants in the loading direction. The stress level necessary to perform the reorientation of these martensite variants is far lower than the stress to induce plastic deformation. The detwinning process is completed when the stress reaches (σ_f). After (σ_f) up to the point C, only elastic deformation is observed. Between the points C and D the material is elastically unloaded and retains an important pseudoplastic deformation. Upon heating, the reverse phase transformation starts at temperature A_s (point E) and finishes when the A_f temperature is achieved. With the absence of plastic deformation during the detwinning process the material's initial shape is recovered.

The reverse phase transformation (M-A) can also occur in the presence of a constant external applied stress. In other words, during reverse transformation, the SMA is capable of applying a force (F) to displace a body on a distance "d". This process is possible when the stress level achieved by the SME is high enough to produce the necessary force

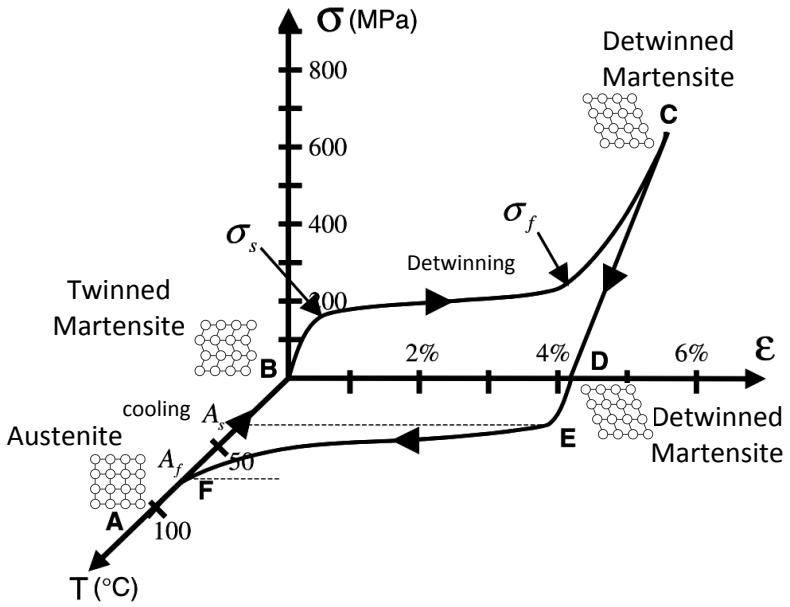

Figure 1.5: *Schematics representation of the shape memory effect on a NiTi SMA (adapted from Lagoudas, 2008).*

(F) to displace a body. Due to this ability, the SMA's are largely used as actuators in several devices.

1.1.5 Superelasticity

Superelasticity is the ability of the SMA to recover large deformation levels only upon releasing the applied stress. Also known as a pseudoelastic effect, this phenomenon is due to the stress induced phase transformation and occurs exclusively when the SMA is above its final austenitic transformation temperature A_f. Figure 1.6 shows a typical SMA superelastic loop.

Generally, the following interpretation of this mechanical response is proposed. Upon loading, the material describes an elastic path between points A and B, until reaching its critical starting stress of martensitic phase transformation σ^{M_s}. Between points B and C, the applied stress promotes the phase transformation inducing the apparition of detwinned martensite phase. The martensitic phase is completed at the final critical stress for martensite transformation σ^{M_f} (point C). Between the points C and D, it is usually assumed that elastic deformation of the detwinned martensite phase takes place. From the point D to E, elastic unloading of martensitic phase takes place, reaching the starting critical stress of austenitic phase transformation σ^{A_s}. With further unloading, the reverse phase transformation is completed when the stress level achieves the final critical stress for austenitic transformation named σ^{A_f}. Finally in the absence of plastic deformation, a total recovery can be achieved at the end of unloading. For some polycrystalline SMA, the stress induced phase transformation may cause up to 8% strain in

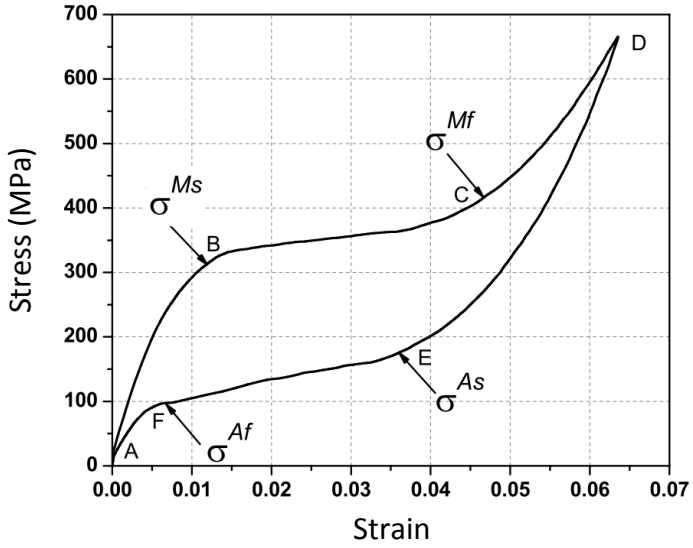

Figure 1.6: *A typical SMA superelastic loop (adapted from Lagoudas, 2008).*

tension reaching 12% strain in shear (Orgéas and Favier, 1998).

Due to the higher stress level of the superelastic plateau during loading than during unloading, a mechanical hysteresis is observed on superelasticity. This hysteresis represents a mechanical energy dissipation. Because of that, the shape memory alloys are largely used as active element in damping devices.

1.2 Thermomechanical coupling in superelasticity

The thermomechanical coupling is a complex interaction between thermal and mechanical effects present on the martensitic phase transformation. During direct phase transformation (A - M) latent heat is released to the ambient, while during the reverse phase transformation (M - A) it is absorbed from the ambient. Also called enthalpy change, the latent heat is positive during direct phase transformation $\Delta H_{released} > 0$ and negative during the reverse phase transformation $\Delta H_{absorbed} < 0$. Figure 1.7 shows a schematic representation of the latent heat behavior during a stress induced phase transformation.

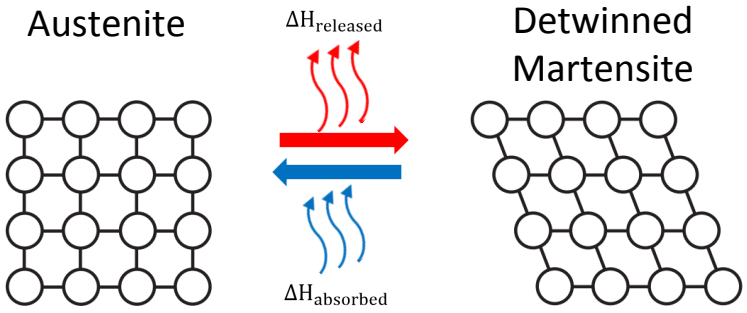

Figure 1.7: *Schematic showing the latent heat released/absorbed on a stress induced phase transformation.*

During a SIPT the latent heat is released during loading and due to the reversible characteristic of the phenomenon it is absorbed during unloading. On a tensile test, the loading rate plays an important role on the materials temperature due to the presence of the released/absorbed latent heat. If loading/unloading is performed slowly enough, heat transfer processes will remove the additional heat without any noticeable temperature variation. However if loading/unloading is applied rapidly, the temperature will rise during loading and fall during unloading, misleading any isothermal assumption.

Moreover, the rise in temperature leads to a rise of the critical transformation stress levels. This variation happens to be linear and is described by the Clausius-Clapeyron Eq.1.1 which states this variation as a constant (C) and relates with the entropy of phase transformation per unit of volume (ΔS), enthalpy of phase transformation per unit of volume (ΔH), test temperature (T) and transformation strain (ε_{tr})(Otsuka and Wayman, 1998).

$$C = \frac{\mathrm{d}\sigma}{\mathrm{d}T} = -\frac{\Delta S}{\varepsilon_{tr}} = -\frac{\Delta H}{\varepsilon_{tr} T} \tag{1.1}$$

Figure 1.8 present a schematic representation of both isothermal (slow strain rate) and non-isothermal (high strain rate) tensile stress-strain behavior. During an isothermal SIPT (low strain-rate, see Fig.1.8a) the heat transfer is strong enough to avoid the material's temperature increase. Because of that, the direct SIPT (from point B to C in Fig.1.8a) presents a well defined stress plateau as well as the reverse SIPT (from point E to F in Fig.1.8a). In another situation, increasing the strain-rate in the presence of a weak heat transfer rate (see Fig.1.8b), the SIPT takes place with a non-isothermal response. In this case, the phase transformation no longer happens in a well defined stress plateau but shows a monotonic variation of the critical transformation stress level. A monotonic increase is observed on the critical stress level during loading (from point B' to C' in Fig.1.8b) and a monotonic decrease on the critical stress level during unloading (from point E' to F' in Fig.1.8b).

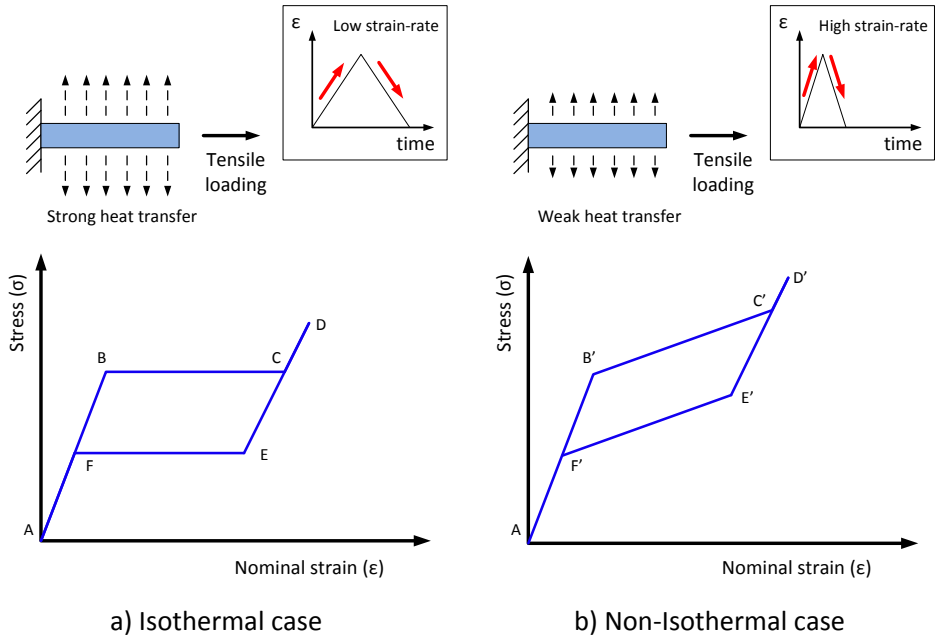

Figure 1.8: *(a) Schematic stress-strain response in isothermal tension (very low strain rate and/or strong heat transfer); (b) and in non-isothermal tension (high strain rate and/or weak heat transfer)(adapted from He and Sun, 2011).*

The first studies on the latent heat and the related temperature change in superelastic SMA were performed focusing on the strain-rate impact and the origin of these thermal effects (Rodriguez and Brown, 1980; Brown, 1981; Mukherjee et al., 1985; McCormick et al., 1993). Recent studies have also continued on the investigation of this phenomenon using advanced measurement methods such as digital image correlation (DIC) and infrared images to acquire local strain and temperature fields, respectively (Schlosser, 2008; Delobelle, 2012; Pieczyska, 2010; Zhang et al., 2010; Xie et al., 2016). Also, the study of this phenomenon has been accompanied by several constitutive models to present an appropriate description of the superelastic effect when subjected to thermomechanical coupling (Schmidt, 2006; Zhu and Zhang, 2007; Yin and Sun, 2012; Roh, 2014).

Some engineering applications based on the thermomechanical coupling are presented in Section 1.2.1. Also, theoretical and experimental aspects present in literature in order to help understanding this phenomenon will be further discussed in the sections 1.2.2 and 1.2.3 respectively.

1.2.1 Engineering applications based on thermomechanical coupling in NiTi superelasticity

Due to the potential use of the SMA superelastic effect in engineering applications, several studies have been performed to improve knowledge on the thermomechanical coupling present on this phenomenon. Among other applications, they have been used

as damping actuators to mitigate vibration amplitudes (Pan and Cho, 2007; Amarante and Cismasiu, 2011; Dieng et al., 2013; Yin et al., 2014; Gur et al., 2016) and as solid state elastocaloric cooling devices as a potential material to replace vapor compression refrigerators (Pataky et al., 2015; Ossmer et al., 2015; Qian et al., 2016b; Tušek et al., 2015; Tušek et al., 2016a).

The influence of the thermomechanical coupling in damping application and its use in elastocaloric cooling devices will be further discussed in sections 1.2.1.1 and 1.2.1.2 respectively.

1.2.1.1 Damping Applications

The mechanical hysteresis present on a superelastic cycle represents a mechanical energy dissipation and can be used to reduce vibration amplitude in dynamic applications. The higher the mechanical hysteresis the greater the dissipated mechanical energy.

The shape of the stress-strain superelastic loop is directly related to the critical stresses to induce phase transformation ($\sigma^{A_s}, \sigma^{A_f}, \sigma^{M_s}$ and σ^{M_f}), which in turn are linear dependent on temperature. So, during loading in a tensile test, if the strain rate is high enough to increase the temperature of the material due to the released latent heat, the critical stress levels will increase. Analogously, during unloading, if the strain rate is high enough to decrease the temperature of the material due to the absorbed latent heat, the critical stress levels will decrease. This variation on the critical stress levels will modify the shape of the superelastic hysteretic loop and consequently the amount of dissipated energy. In this context, several works investigated the influence of strain rate on the superelastic hysteretic loop of shape memory alloys (Zhang et al., 2010; He and Sun, 2011; Kan et al., 2016).

Zhang et al., 2010 studied the influence of the strain rate on the stress hysteresis size during tensile tests of superelastic NiTi alloys performed at room temperature in stagnant air conditions. They observed temperature variations (ΔT) on the order of $\Delta T = +29°C$ during loading and $\Delta T = -9°C$ during unloading. These temperature variations were responsible for increasing the stress level in around $\Delta\sigma = 100MPa$ at the end of loading and $\Delta\sigma = 50MPa$ at the end of unloading. The critical stress variation associated to the temperature variation promoted an important change on the superelastic loop area as observed in Fig. 1.9a. From the stress-strain curves plotted in Fig. 1.9a the authors calculated the dissipated mechanical energies as the area inside the hysteresis loop and plotted in function of strain rate, as shown in Fig.1.9b.

They observed a non-monotonic variation of the stress hysteresis with the strain rate reaching a peak at $\dot{\varepsilon} = 2.0 \times 10^{-3}s^{-1}$. The stress hysteresis peak observed at this strain rate was the result of the interaction between the heat released/absorbed during the material's phase transformation and the ambient conditions. This interaction allowed the increase of the upper stress plateau and the decrease of the lower plateau (see the blue loop in Fig.1.9a) allowing so the increase in the loop area. They also observed that for strain rates below $\dot{\varepsilon} = 1.1 \times 10^{-4}s^{-1}$ the stress hysteresis showed a constant trend

once the temperature variation observed was negligible. The same constant tendency was observed for strain rates above $\dot{\varepsilon} = 1.1 \times 10^{-1} s^{-1}$ were an adiabatic behavior was observed. Finally they concluded that the mechanical hysteresis variation was governed by the effect of the temperature induced by the released/absorbed latent heat during SIPT.

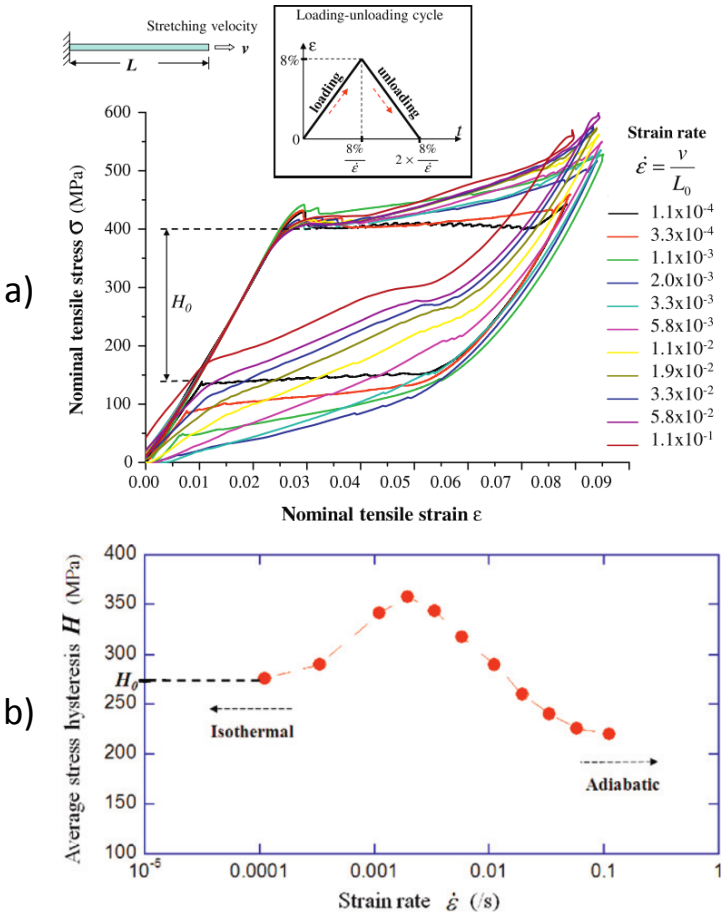

Figure 1.9: *(a) Macroscopic nominal stress-strain curves for different strain rates and (b) the variation in the average stress hysteresis with nominal strain rate (adapted from Zhang et al., 2010).*

In a similar work, He et al., 2010 investigated the effect of the ambient condition on the thermomechanical behavior of SMA. They submitted SMA specimens to tensile tests at three different ambient conditions: still air and 2 different airflow speeds, all of them at the room temperature. Figure 1.10 shows the stress hysteresis in function of the strain rate for all the ambient conditions. As well as Zhang et al., 2010, they observed a non-monotonic increase on the stress hysteresis with the strain rate for the three ambient conditions. With these results He et al., 2010 showed that independently of the ambient condition, the temperature variation due to thermomechanical coupling will always affect the stress hysteresis once the strain rate do not provide an isothermal

or adiabatic test condition. In other words, there will be always a competition between the release/absorption of heat during SIPT and its dissipation to the ambient.

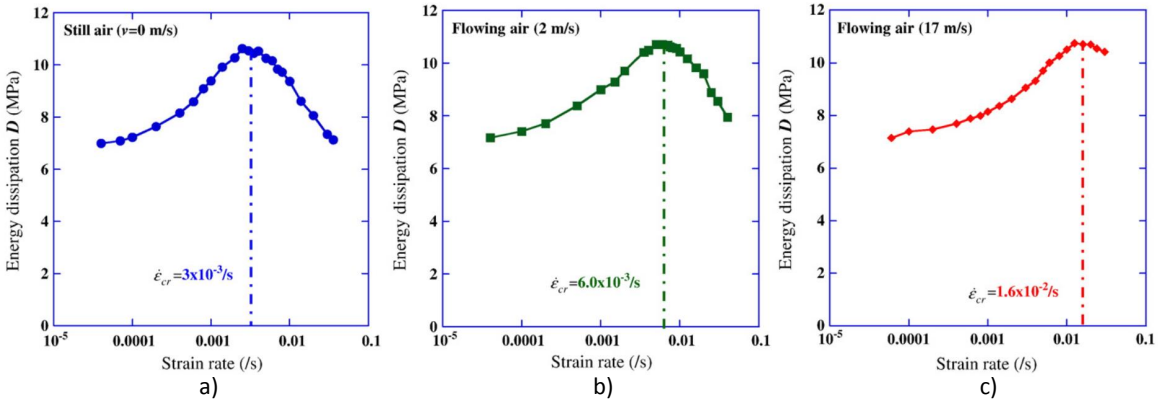

Figure 1.10: *Energy dissipation (hysteresis area) in function of strain rate at three different ambient conditions (a) still air, (b) airflow at $v = 2m/s$ and (c) airflow at $v = 17m/s$ (dapted from He et al., 2010).*

1.2.1.2 Elastocaloric Cooling Devices

As previously shown, the thermomechanical coupling present on the SIPT has been studied regarding its mechanism and its effect on the mechanical response in cyclic dynamic applications (as described in section 1.2.1.1). It was not until very recently that the thermomechanical coupling also called elastocaloric effect was recognized as a potential cooling mechanism for heat-pumping applications. Its advantage over the classic vapor compression cooling technology is the use of a solid state material instead of refrigerant gases. The commonly used gases such as hydrochloroflurocarbons (HCFCs) and hydrofluorocarbons (HFCs) are a significant source of the greenhouse effect, making this technology not environmentally friendly.

The use of the SMA in elastocaloric cooling devices is based on the heat pump principle which is to transfer the energy from a heat source to a heat sink. As described by Schmidt et al., 2015a, similar to the conventional vapor compression refrigeration cycle, the SMA based cooling cycle can be divided in four phases (see Fig.1.11):

1. Loading: The strain increases at a high strain rate leads to a near-adiabatic temperature increase of the SMA ribbon above the temperature of the heat sink.

2. Heat transfer to heat sink: At constant high strain the SMA ribbon contacts the heat sink. The heat sink absorbs heat from the SMA, the temperature of the SMA ribbon decreases and the temperature of the heat sink increases.

3. Unloading: The strain decreases at a high strain rate, leading to a temperature decrease of the SMA ribbon below the temperature of the heat source.

4. Heat transfer from heat source: At constant low strain the SMA ribbon contacts the heat source. The SMA absorbs heat from the heat source, the temperature of the SMA ribbon increases and the temperature of the heat source decreases.

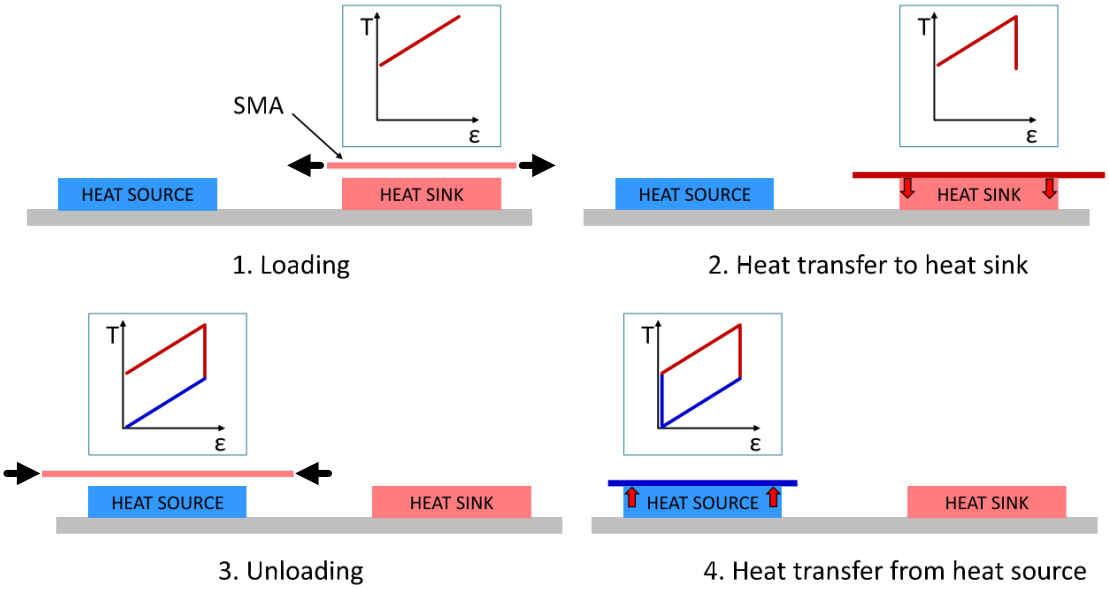

Figure 1.11: *Schematic of a SMA based cooling process described in four steps: 1.Loading, 2.Heat transfer to heat sink, 3.Unloading and 4.Heat transfer from heat source (Adapted from Schmidt et al., 2015a).*

This exemplary elastocaloric cooling cycle shows the feasibility of a heat pump system using shape memory alloys. In this way several works on the application of SMA in elastocaloric cooling devices have been proposed in the literature (Schmidt et al., 2015a; Schmidt et al., 2016; Qian et al., 2016b; Qian et al., 2016a). In these studies an important property analyzed in regard of heat pumping is the system efficiency. To measure the efficiency of a heat pump cycle a commonly metric used is the coefficient of performance (COP) (Tušek et al., 2016b). It is defined as the ratio between the cooling/heating energy and the input work required to perform a thermodynamic cycle (Eq. 1.2).

$$COP = \frac{Q}{W} \tag{1.2}$$

with Q standing for the thermal energy and W the mechanical energy.

In the work published by Cui et al., 2012 it was investigated the efficiency of elastocaloric cooling SMA as solid-state refrigerant to be used in heat pumps. They obtained

COP levels in the order of 11.8 and 3.7 for NiTi wires when submitted to tension and compression respectively. These values corresponds to 83.7% and 56.5% when compared to theoretical Carnot cycle COP values (see Eq.1.3). For comparison purpose, vapor compression commercial systems show COP values up to 60% of the theoretical Carnot cycle (Cui et al., 2012).

$$COP_{Carnot} = \frac{T_c}{T_h - T_c} \tag{1.3}$$

with T_c standing for the temperature of the cold source and T_h the temperature of the hot source.

In this way, the use of SMA shows great potential as refrigerant element to replace gas in vapor compression heat pump systems. However, to master this technology, one of the key parameter is the knowledge of the thermal energy involved on the SIPT.

1.2.2 Thermodynamic framework of thermoelastic martensitic transformation

Several thermodynamic frameworks provide a description of the thermomechanical behavior of shape memory alloys. Some aims to account the complex state behaviour and thermomechanical coupling of polycrystaline SMA (McNichols and Cory, 1987; Chrysochoos et al., 1996). Others are based on the pioneering work of Cohen and his collaborators (Patel and Cohen, 1953; Salzbrenner and Cohen, 1979). In all of these approaches, the martensite transformation is considered a first order diffusionless reversible phase transformation. Also equilibrium condition is analyzed at the austenite-martensite interface of an elementary volume of material.

In this context, a thermodynamic framework based on the studies developed by Ortín and Planes, 1989 and Wollants et al., 1993 is presented. Firstly the hypothetical absence of any irreversibility is considered. Next, the particular case of a uniaxial stress induced phase transformation is presented. Finally, the sources of irreversibility are introduced and its effects on thermomechanical behaviour are discussed.

Notation and units

The units of properties involved in the thermodynamic framework is listed on Table 1.1. The units apply to the symbols even when sub or superscripts are added. This table is for reference and throughout text these symbols are still presented. Throughout this section $\Delta\bullet$ denotes the difference of a property between martensite and the parent phases.

Table 1.1: Units of the properties used in this thermodynamic framework

Symbol	Property	Unit
G	Specific Gibbs free energy	J/kg
H	Specific enthalpy	J/kg
P	Pressure	Pa
T	Temperature	K
S	Specific entropy	J/kg.K
U	Specific internal energy	J/kg
V	Specific volume	m^3/kg
W	Specific work	J/kg
σ	Stress	Pa
ε	Strain	-
f_m	Martensite fraction	-
ρ	Mass density	kg/m^3
E_{fr}	Specific frictional work	J/kg
E_{st}	Specific stored elastic energy	J/kg

1.2.2.1 The Gibbs free energy equation

A **thermodynamic potential** is a state function that describes the behaviour of a thermodynamic system as function of its natural variables. For the thermodynamic system consisting of martensite or austenite phase, the thermodynamic potential is the specific Gibbs free energy G and the natural variables are pressure P and temperature T. According to the first and second laws of thermodynamics, Eq. (1.4) relates G to P and V for the case where only $P-V$ reversible work is involved

$$G(P,T) = U + PV - TS = H - TS \tag{1.4}$$

where U is the system's specific internal energy, V is the specific volume, S is the specific entropy and H is the specific enthalpy.

The driving force for the phase transformation is the difference between the Gibbs free energy of austenite $G^A_{P,T}$ and that of martensite $G^M_{P,T}$:

$$\Delta G_{P,T} = G^M_{P,T} - G^A_{P,T} \tag{1.5}$$

A thermodynamic equilibrium is met when the difference between the thermodynamic

potential of the phases is minimal for a set of values of the natural variables (P, T) . In the two-phase system composed by martensite (M) and austenite phases (A), this means at

$$G^M_{P,T} = G^A_{P,T} \tag{1.6}$$

and according to Eq. (1.4), at

$$\Delta G_{P,T} = \Delta H_{P,T} - T\Delta S_{P,T} = 0 \tag{1.7}$$

with $\Delta H_{P,T}$ and $\Delta S_{P,T}$ being the enthalpy and entropy variation between phases at a given P, T pair. They originate from the chemical differences of austenite and martensite phases.

1.2.2.2 Uniaxially stress-induced transformation

When a stress is externally applied in the thermodynamic system, the thermoelastic martensitic transformation is said to be stress-induced. In this case a reversible mechanical work is performed on the system. According to continuum mechanics theory, the mechanical work per unit of mass performed on a representative element volume (REV) can be written as a function of the average stress and macroscopic strain tensors. If the stress is applied uniaxially the specific mechanical work is

$$W_{mech} = \frac{1}{\rho}\sigma d\varepsilon \tag{1.8}$$

where ρ is the mass density, σ is the uniaxial stress tensor externally applied on the system and ε is the uniaxial macroscopic strain.

Ignoring elastic and plastic strain components and considering only transformation strains (ε_{tr}), as well as introducing f_m as the martensite fraction and df_m as an infinitesimal step of martensite fraction, Eq. (1.8) can be written as

$$W_{mech} = \frac{1}{\rho}\sigma d\varepsilon = \left(\frac{\partial W_{mech}}{\partial f_m}\right) df_m = W'_{mech} df_m \tag{1.9}$$

A linear relation between $d\varepsilon_{tr}$ and df_m is assumed:

$$d\varepsilon_{tr} = \Delta\varepsilon_{tr} df_m \tag{1.10}$$

where $\Delta\varepsilon_{tr}$ is defined as the transformation strain for a complete transformation, at $f_m = 1$. Equation (1.9) then becomes

$$W'_{mech} = \frac{1}{\rho}\sigma\Delta\varepsilon_{tr} \tag{1.11}$$

Finally, the difference between the Gibbs free energy of martensite and austenite in Eq. (1.7) can be rewritten as

$$\Delta G_{P,T} = \Delta H_{P,T} - T\Delta S_{P,T} - \frac{1}{\rho}\sigma\Delta\varepsilon_{tr} = 0 \tag{1.12}$$

which expresses the thermodynamic potential of a uniaxially stress-induced thermoelastic martensitic transformation happening on thermodynamic equilibrium.

This external work displaces the thermodynamic equilibrium, that now occurs at $T = T(\sigma)$. However, it does not change the fact that the transformation happens isothermally when pressure is kept constant.

1.2.2.3 Sources of thermodynamic irreversibility

In the previous section the thermodynamic potential for phase transformation was presented for the case where only reversible work is involved (either $P - V$ or external mechanical work). However, in reality, the martensitic phase transformation does not occur isothermally, but rather in a temperature range, generally accompanied by a hysteresis between forward and reverse transformations.

These deviations from equilibrium are caused by the presence of two main non-chemical irreversible contributions in the thermodynamic potential: the **frictional work**, associated with the energy dissipated by the relative movements between the austenite and martensite interfaces; and the **stored elastic energy**, associated with the shape and volume changes during transformation between austenite and martensite.

1.2.2.3.a Frictional work E_{fr}

Frictional work is present in thermally or stress induced transformations. It can be defined as the work performed to overcome interface motion, which is directly related to the amount and nature of the barriers opposing the movement of transformation fronts. This parcel of energy is ultimately dissipated from the system as heat during both forward and reverse transformations (Wollants et al., 1993).

1.2.2.3.b Stored elastic energy E_{st}

The stored elastic energy is generated from two sources: elastic strain energy and interfacial energy (Ortín and Planes, 1989; Hamilton et al., 2004). The first can be defined as

the work performed against internal forces to modify the total strain of the system and the latter comes from the creation of new interfaces and/or changes in existing interface dimensions.

1.2.2.4 Thermodynamic potential with irreversibility contributions

These non-chemical contributions must be added to the thermodynamic potential expressed in Eq. (1.7), characterizing the thermoelastic phase transformation as it happens in reality. From now on, the subscript notation "P, T" is omitted and the following subscripts are adopted: "ch" for chemical energy contributions, "fr" for non-chemical frictional work and "st" for non-chemical stored elastic energy. Thus, for a given set of natural variables one obtains

$$dG = (\Delta H_{ch} - T\Delta S_{ch})df_m + \partial E_{st} + \partial E_{fr} = 0 \tag{1.13}$$

where ΔH_{ch} and ΔS_{ch} constitute the chemical contributions of enthalpy and entropy changes, respectively; and ∂E_{st} and ∂E_{fr} constitute the non-chemical contributions of stored elastic energy and frictional work, respectively.

Equation (1.13) can be rewritten as function of the martensite mass fraction as

$$dG = (\Delta H_{ch} - T\Delta S_{ch})df_m + (\partial E_{st}/\partial f_m)df_m + (\partial E_{fr}/\partial f_m)df_m = 0 \tag{1.14}$$

or in derivative form as

$$G' = \Delta H_{ch} - T\Delta S_{ch} + E'_{st} + E'_{fr} = 0 \tag{1.15}$$

where the superscript $'$ designates the partial derivative of a property with respect to f_m. Thus, $E'_{st} = \partial E_{st}/\partial f_m$ and $E'_{fr} = \partial E_{fr}/\partial f_m$.

When the material is fully in the austenite phase, the martensitic fraction is written $f_m = 0$ and when fully in the martensite phase the martensitic fration is $f_m = 1$. During the forward transformation the infinitesimal martensite mass fraction step df_m is positive and during reverse transformation it is negative.

Including the contribution of an external mechanical work in a stress-induced phase transformation occurring under the application of uniaxial stress, Eq. (1.15) can be rewritten as

$$G' = \Delta H_{ch} - T\Delta S_{ch} + E'_{st} + E'_{fr} - \frac{1}{\rho}\sigma\Delta\varepsilon_{tr} = 0 \tag{1.16}$$

Sign convention

Considering that work performed by the system is negative and work performed on the system is positive, the sign of each non-chemical contribution in Eq. (1.15) can be defined for the forward and reverse transformations.

The stored elastic energy is work performed by the system during forward transformation and work performed on the system during reverse transformation. Therefore dE_{st} must be positive during forward and negative during reverse transformation. This makes both $E'^{A\to M}_{st}$ and $E'^{M\to A}_{st}$ positive values due to df_m signs in each sense. The frictional work dE_{fr} is always performed by the system and thus is always positive. This leads to a positive $E'^{A\to M}_{fr}$ and a negative $E'^{M\to A}_{fr}$. Furthermore, ΔH_{ch} and ΔS_{ch} are both negative.

1.2.3 Experimental studies on thermomechanical couplings

1.2.3.1 Local measurements

In one of the pioneering works about the thermomechanical coupling, Rodriguez and Brown, 1980 studied experimentally the thermal effect on the stress induced martensite transformation in single crystals of CuAlNi SMA on tensile tests.

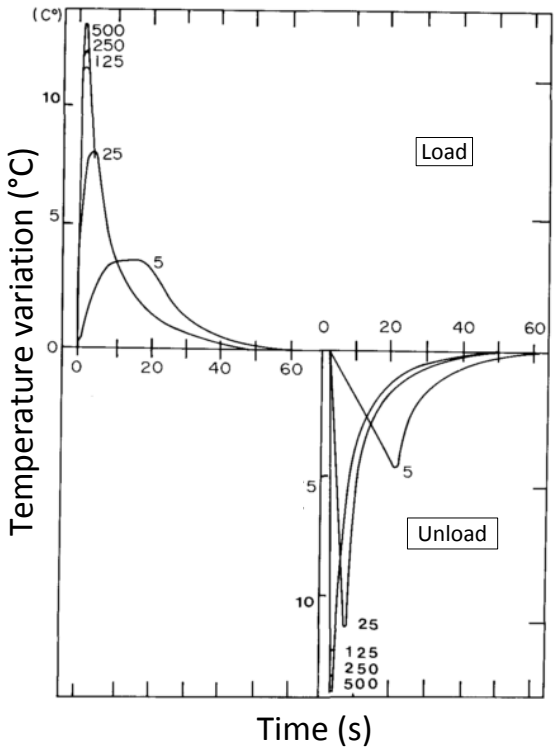

Figure 1.12: *(a)Temperature variation in function of time for different cross-head speeds (in mm/min); (b) and variation of the critical stress for martensite nucleation (σ_c) as a function of temperature (adapted from Rodriguez and Brown, 1980).*

A thermocouple welded to the center of the specimen's gauge length (l_0 =20 mm) was used to investigate the temperature variation with the increase of the strain rate on the superelastic behavior. They observed an increase in the specimen temperature of about $\sim 4°C$ for a cross-head speed of $5\,mm/min$ and up to $\sim 14°C$ when submitted to a higher cross-head speed of $500\,mm/min$.

Peyroux et al., 1998b also investigated the thermomechanical coupling during a stress induced phase transformation on superelastic CuZnAl alloys. Using infrared and calorimetric techniques, they analyzed the temperature variation and investigated the heat sources present on this phenomenon. Mechanical and thermal energies were estimated during the stress induced phase transformation for different strain rates. They observed that, independently of the strain-rate, mechanical and thermal energy remained constant despite the increasing temperature (see Fig. 1.13). They concluded that the increasing behavior of the stress level with the strain-rate was due to the thermomechanical coupling effects rather than viscous effects.

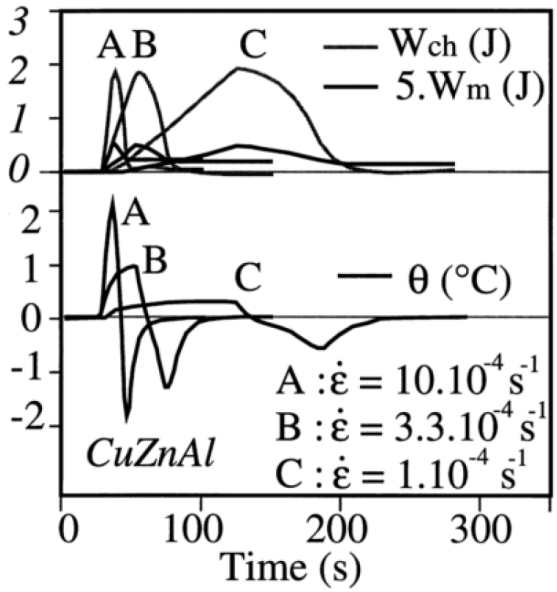

Figure 1.13: *Thermal energy (W_{ch}), mechanical energy (W_m) and temperature variations (θ) at different strain rates (adapted from Peyroux et al., 1998b).*

1.2.3.2 Full field measurements

Since the pioneer work of Miyazaki et al., 1981 using optical methods, many studies has been published with this kind of technique. With the advance of technology, thermal measurements also started to be performed via infrared cameras. The first observation of thermal fields recorded during a tensile test was published by Shaw and Kyriakides, 1997a. Then, many studies using simultaneous kinematics and thermal field measurements were applied to investigate the thermomechanical coupling in SMA's.

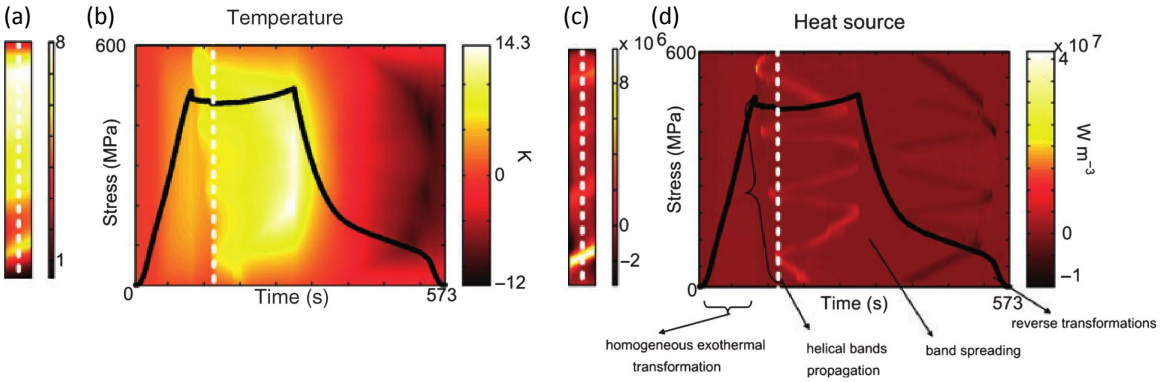

Figure 1.14: *Temperature measurement and heat sources estimation during a tensile test of a NiTi tube sample (adapted from Schlosser et al., 2007).*

For example, Schlosser et al., 2007 investigated the thermomechanical coupling during a stress induced phase transformation on a superelastic NiTi tube. Thanks to a thermal camera and a digital image correlation (DIC) system, they obtained the temperature and strain fields during a tensile test and quantified the amount of energy involved on the SIPT. The material showed a strong localized deformation behavior and due to the specimen's geometry (tube), the Luders-like deformation bands appeared in a helical or ring shape (Schlosser, 2008). Due to the localized strain presence a temperature gradient was observed in the specimen. Finally, even with a heterogeneous temperature field, they were able to perform a 2D formulation of the thermal problem in order to quantify the heat sources on the tube. Figures 1.14 a and c show an example of a temperature and heat sources with a spatiotemporal representation in Fig. 1.14d.

These results put in evidence how the advances of technology and the development of full field measurement techniques, like infrared thermography and DIC, improved the accuracy and allowed local investigations of thermomechanical couplings in SMA.

1.2.3.3 Heat sources estimation

As mentioned before, temperature variations are observed during a SIPT. The cause of these thermal response are the local heat sources. The aim of this section is to present the method chosen to estimate heat sources from temperature measurements. A first set of assumptions is stated in order to write a general heat balance equation describing the heat transfer in solid materials (Section 1.2.3.3.a). Then, the model is simplified into a 0D formulation which is the case when homogeneous thermal response is observed (Section 1.2.3.3.b).

1.2.3.3.a General heat balance equation

The heat balance equation governing heat transfer is deduced from the first law of thermodynamics applied to continuum media. The spatial local form of the first law combined with the momentum and mass energy balances leads to the energy equation. This one introduces the specific internal energy e, the mass density ρ, the internal stress power per unit of volume p_{int}, the heat flow vector q per unit area and the distributed external heat sources s_e per unit volume. The given equation reads:

$$\rho\dot{e} = -p_{int} + s_e - \mathbf{div}\,\mathrm{q} \tag{1.17}$$

The term "**div**" shown in Eq.1.17 is the divergence operator applied to the heat flow vector q, defined with respect to the spatial coordinates x_i. The term $\dot{e}$ represents the material time derivative of the specific internal energy e.

The heat conduction is assumed to be governed by the standard Fourier's law and the medium considered isotropic, with that, the heat flow q is written:

$$q = -k\,\mathbf{grad}\,T \tag{1.18}$$

where "**grad**" is the gradient operator with respect to the spatial coordinates x_i and the thermal conductivity k. In our analysis, thermal conductivity is assumed uniform along the sample and constant during the test.

Rewriting the Eqs. 1.17 and 1.18 with the specific heat capacity c, the local heat balance is defined as (Louche, 1999; Schlosser, 2008; Chrysochoos and Louche, 2000):

$$\rho c\dot{T} - k\,\mathbf{lap}\,T = s_i + s_e \tag{1.19}$$

where "**lap**" stands for the Laplacian operator with respect to the x_i and s_i stands for the heat rate generation per unit volume of all internal origins such as: intrinsic generation, thermoelastic coupling or latent heat due to solid-solid phase transformation (McCormick et al., 1993).

Analyzing the Eq.1.19, if the temperature is expressed as a function of the spatial position M of a particle P, i.e. $T(M,t)$, the material time derivative of temperature is given by:

$$\dot{T} = T_{,t} + v\,\mathbf{grad}\,T \tag{1.20}$$

with $T_{,t} = \partial T/\partial t$ as temperature time derivative and v the current velocity of the considered particle at the spatial position M. The second term of the right hand side of the Eq. 1.20 implies the necessity to know simultaneously the kinematic and thermal

fields. In our approach the terms "$v\,\mathbf{grad}\,T$" and "s_e" are assumed to be negligible. Because of that, the general heat balance equation is finally written as:

$$\rho c T_{,t} - k\,\mathbf{lap}\,T = s_i + s_e \tag{1.21}$$

1.2.3.3.b Simplified thermal model

The general heat balance equation Eq.1.21 can be written in a simpler form when the internal heat sources are uniformly distributed ($s_i(x,y,z,t) = s_i(t)$) in a specimen surrounded by ambient medium at a temperature T_0 and when the specimen's temperature (T) is not too far from thermal equilibrium (Chrysochoos et al., 1996; Chrysochoos and Louche, 2000). Hence, at any point of the specimen's surface, the Laplacian term can be linearised:

$$\frac{-k}{\rho c}\,\mathbf{lap}\,\theta(t) \approx \frac{\theta(t)}{\tau_{eq}} \tag{1.22}$$

where θ is the temperature variation ($\theta = T - T_0$) and $\theta \ll T$.

Therefore, Eq.1.21 becomes:

$$\rho c \left(\frac{d\theta(t)}{dt} + \frac{\theta(t)}{\tau_{eq}} \right) = s_i(t) \tag{1.23}$$

The parameter "τ_{eq}" represents a characteristic time reflecting the heat losses (by radiation, convection and conduction) through the specimen surfaces and towards the grip zones, respectively. This parameter is experimentally estimated and is necessary to solve the Eq. 1.23. One method to estimate the τ_{eq} is to observe the natural temperature variation (towards the equilibrium) during a hold time after a loading/unloading test. During the temperature stabilization, heat sources are assumed to be zero once no phase transformation, thermoelasticity nor plasticity are present. From that, τ_{eq} is then estimated through the following equation:

$$\frac{d\theta(t)}{dt} + \frac{\theta(t)}{\tau_{eq}} = 0 \tag{1.24}$$

1.3 Nanostructured NiTi wires

1.3.1 Specificities of the NiTi alloys

1.3.1.1 General Characteristics

NiTi alloys have been studied most extensively and used in the greatest number of commercial applications when compared to other SMA. This alloy exhibits strong shape memory and superelastic effects (up to 8% recoverable strain) (Lagoudas, 2008) which makes this material ideal for a variety of applications.

Equiatomic NiTi alloys (i.e. 50 at. % of Ni) exhibit the highest final critical temperature transformation A_f, around $120°C$. Decreasing the atomic percentage of Ni in the alloy does not change the transformation temperatures. However, increasing the Ni percentage to 51 % at. the transformation temperature decreases to $A_f = -40°C$. This transformation temperature variation can be designed to obtain the desired behaviour (SME or SE) at the application's temperature (e.g. human's body temperature at biomedical applications).

Thermomechanical properties are strongly dependent on the alloy's composition as well as thermomechanical historic processing. In Ni-rich alloys, heat treatments may promote the formation of Ti_3Ni_4 precipitates which reduces the amount of Ni on the NiTi matrix. This reduction directly affects the critical transformation temperature which may change the alloy's characteristics from SME to SE at room temperature, for example.

1.3.1.2 Crystallographic microstructure of NiTi alloys

The martensite transformation is a diffusionless phase transformation in which the atoms move cooperatively driven by a shear-like mechanism. The atomic movement inside the crystal lattice promotes an atomic rearrangement which generates a crystallographic phase change. Even though the relative atomic displacements are small (compared to inter-atomic distance) a macroscopic shape change is produced (Otsuka and Wayman, 1998).

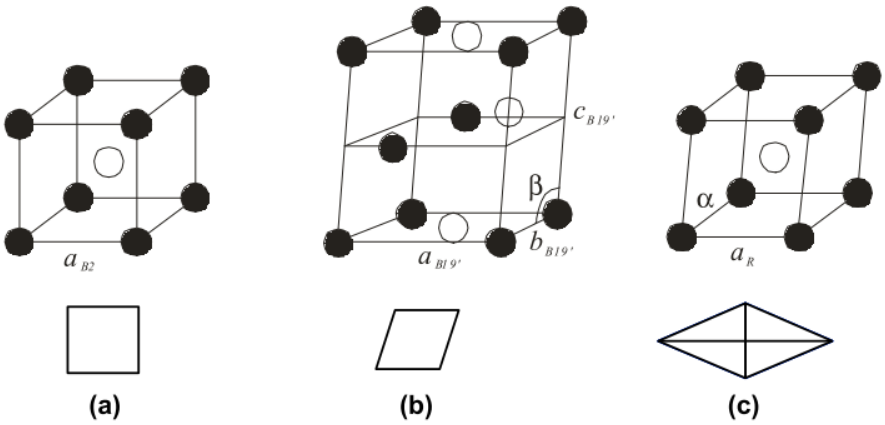

Figure 1.15: *The crystal structures of NiTi alloys. (a) Cubic austenite parent $B2$, (b) Monoclinic $B19'$ martensite and (c) R-phase. (Adapted from Schlosser, 2008)*

NiTi near-equiatomic SMAs show three different crystallographic lattices in solid state, namely: body centered cubic (BCC) also known as B2 cubic austenite; monoclinic or $B19'$ martensite and rhomboedral or R-phase. The latter appear under certain structural and thermomechanical conditions between the austenite and martensite phases. A schematic representation of the above mentioned lattices is shown in the Fig. 1.15.

1.3.1.3 Strain localization phenomenon in NiTi alloys

The strain localization consists on the appearance and propagation of macroscopic strain bands under constant stress level (plateau-type stress-strain curve). Also known as Luders-like deformation mode, this mechanism has only been observed in NiTi alloys, not in any other polycrystalline SMAs (Sittner et al., 2005). An example of strain localization observed by full field measurements (kinematic and thermal fields) is given by Fig. 1.16.

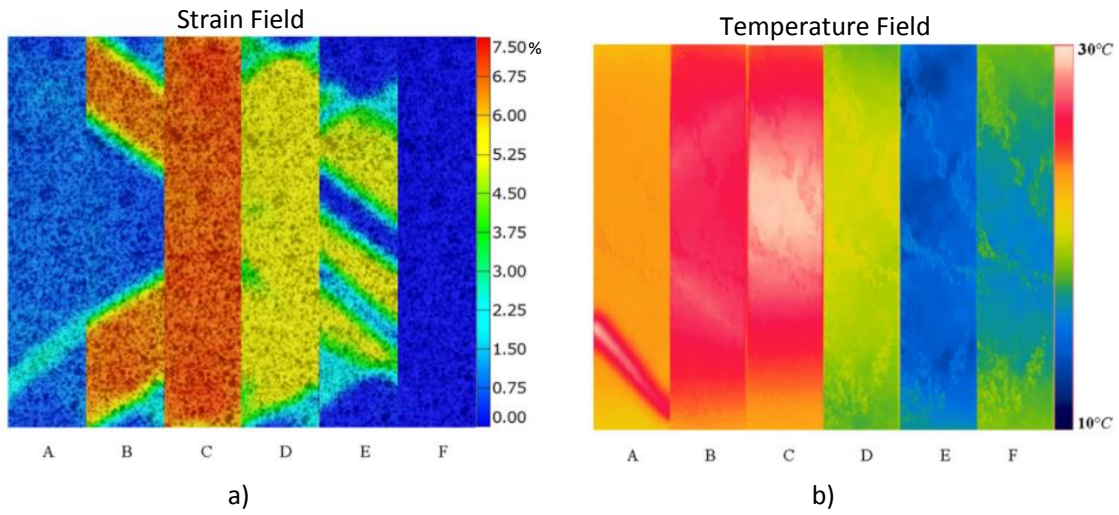

Figure 1.16: *a) Strain field obtained trough DIC and b) temperature field obtained trough IR camera of a dog-bone shaped NiTi specimen showing localization pattern. (Adapted from Xie et al., 2016)*

The main characteristics of this phenomenon are:

- It has been found to occur only during deformation in tension, not under another applied stress state, e.g. shear, compression, tension-torsion (Orgéas and Favier, 1998; Sun and Li, 2002);
- It has been found to occur during tensile deformation via any process: stress induced transformation or stress martensitic reorientation;
- Whereas it has been observed in a variety of specimen geometries (thin wires, thick bars, ribbons, plates, dog-bone shaped specimens and tubes), this effect appears to be more pronounced in specimens of large length-to-thickness aspect ratios (Shaw and Kyriakides, 1997a; Messner et al., 2000).

1.3.2 Influence of wire manufacturing process on crystallographic structure and mechanical behaviour

NiTi wires are commonly manufactured through a sequence of hot and/or cold working which may be followed by a heat treatment above its recrystallization temperature ($350°C$).

The hot/cold working is a process in which the material is deformed plastically to take the shape of the die geometry. In these thermomechanical forming processes the thickness reduction may reach values up to 60% (Koike et al., 1990; Otsuka and Ren, 2005),

strongly modifying the material microstructure and directly affecting its thermomechanical properties. In most metallic alloys, these thermomechanical forming processes are used not only to obtain a final shape for the material, but also with the purpose of modifying the cast structure and produce a desired microstructure (Ahadi et al., 2012). The main differences between hot and cold working are listed in the Table 1.2:

Table 1.2: Main characteristics of Cold and Hot working

Cold Working	**Hot working**
It is done at a temperature **below** the recrystalization temperature	It is done at a temperature **above** the recrystalization temperature
It is accomplished by **strain hardening**	**Hardening** due to plastic deformation **is eliminated**
Crystalization **does not take place**	Crystalization **takes place**
Internal and residual stress **are produced**	Internal and residual stress **are not produced**
No influence of **oxydation**	Strongly **affected by oxydation**

In NiTi alloys, hot working is mostly used to produce specific microstructure and induce a desired anisotropy usually oriented in the rolling/drawing direction. Also, since it is performed above the recrystallization temperature, hot working produces a material showing higher shape memory properties (Ahadi et al., 2012) once dynamic recrystallization takes place during the process.

In cold working process, however, recrystallization does not take place and a strong grain size reduction is observed. Such a process causes an increase of the tensile strength and hardness, eliminates the superelastic plateau, reduces the ductility and shape memory recovery (Mitwally and Farag, 2009). It has also been published in literature that cold working process suppress martensitic transformation via grain size reduction and even the amorphization of the material's structure (Koike et al., 1990). A heat treatment performed on a cold worked material can always recover and even optimize the suppressed properties, such as SE or SME (Mitwally and Farag, 2009).

1.3.3 Influence of heat treatment on microstructure and mechanical behavior

It has been shown in literature that the properties of NiTi alloys can be manipulated through cold work, heat treatment or a combination of both. As previously mentioned, cold work promotes a grain-size reduction and even a partial or total amorphization of the crystalline microstructure in NiTi alloys (Delville et al., 2010; Koike et al., 1990). In a work published by Delville et al., 2010 a study was performed on the effect of non-conventional heat treatments on cold worked NiTi wires. On their approach, they submitted NiTi wires to different pulsed electric current times in order to perform local heat treatment through joule effect. From the obtained results they compared the evo-

lution of the microstructure and the mechanical response of the tested wires, shown in Fig.1.17.

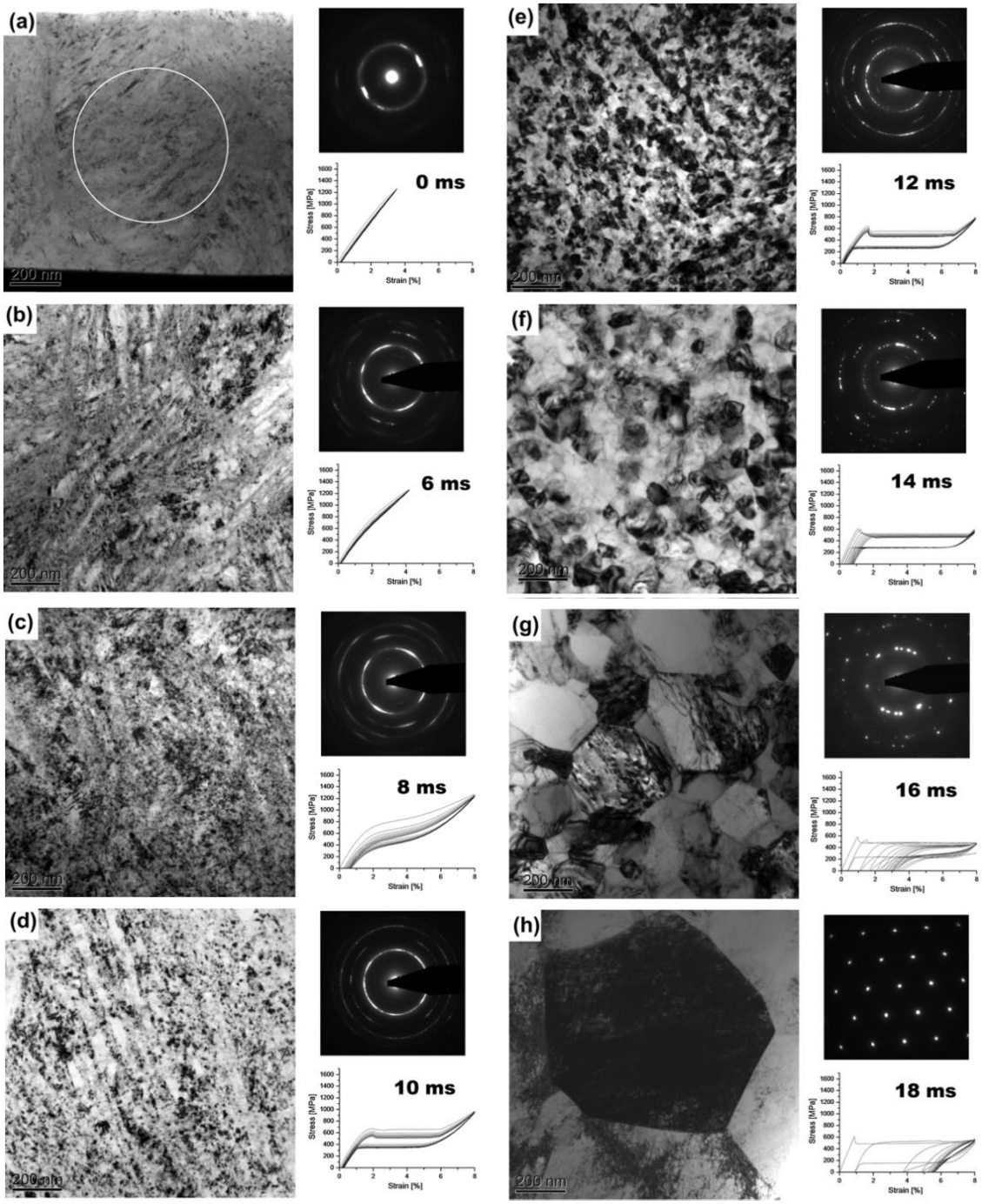

Figure 1.17: *Evolution of microstructure and corresponding superelastic functional properties in the Ni–Ti wires heat treated by electric pulses with pulse times t= 0, 6, 8, 10, 12, 14, 16 and 18 ms (a to h, respectively)(Adapted from Delville et al., 2010)*

Figure 1.17(a) presents the result obtained for the "as received" cold worked wire which was submitted to section area reduction of 45±5%. The stress - strain curve shows a pure elastic behavior characteristic of a strain hardened NiTi alloy. It is also possible to observe the partially amorphous microstructure revealed by the electron microscopy and transmission electron microscopy (TEM) diffraction pattern. Observing the stress - strain curve in Fig.1.17(b) it is already noticeable a minor changing on the elastic behavior and a smaller increase on the strain level. From the TEM diffraction pattern, the weak intensity of halo suggests that recrystallization in the amorphous areas has taken place.

From Figures 1.17(c) to (h) it is clearly observed the evolution of the hysteretic superelastic loop with the increase of the intensity of heat treatment (pulsed current from 8ms to 18ms). This evolution is followed by the change of the microstructure characterized by the increase of the grain size observed on the micrographies and ratified through the explicit dots on the diffraction patterns.

In a similar work on the investigation of the grain size influence on the thermomechanical behavior of SMA Ahadi and Sun, 2014 studied the effect of the grain size on the rate - dependent thermomechanical response of cold worked NiTi sheets. In their study, they submitted a NiTi sheet to a cold work process where a 42% thickness reduction was achieved. A further heat treatment was performed at four different temperature - time configurations, namely $SA = 520°C$ for 6 min.; $SB = 520°C$ for 3 min.; $SC = 520°C$ for 2 min. and $SD = 485°C$ for 2 min. They observed an increase of the grain size with the increase of the intensity of heat treatment (temperature vs. time). The average grain size values observed were: $SA = 90$ nm, $SB = 68$ nm, $SC = 42$ nm and $SD = 27$ nm. This variation was reflected on the superelastic response where a higher hysteretic behavior was observed for the larger grain sized material, as shown at Fig. 1.18.

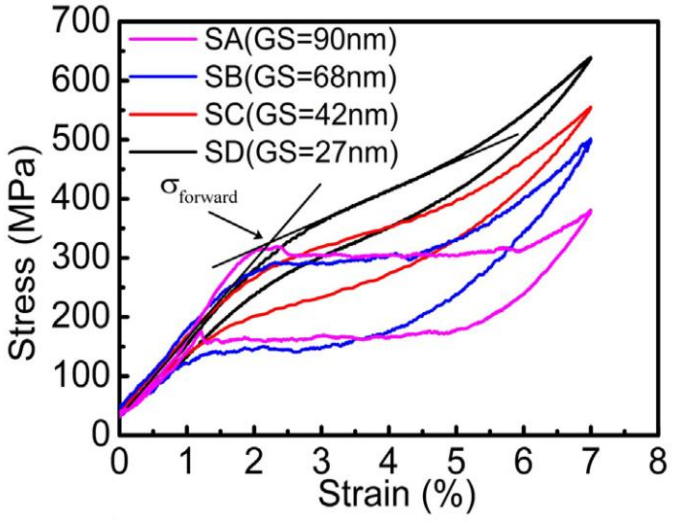

Figure 1.18: *Effects of grainsize on the isothermal superelastic response ($\sigma - \varepsilon$) (Adapted from Ahadi and Sun, 2014)*

A more explicit hysteretic loop implies that more phase transformation is happening on superelasticity. In this way, the more austenite phase being stress induced into martensite phase, the more latent heat of transformation can be released/absorbed. Following this reasoning, they submitted the cold rolled (CR) and the heat treated (SA, SB, SC and SD) sheets to three different strain rates in order to observe the temperature variation and further analyse its effect on the mechanical behavior. Figure 1.19 shows the (a) full - field thermografic images as well as the (b) volume - averaged temperatures $T(t)$ for all the tensile tested sheets at the following strain rates: $\dot{\varepsilon} = 10^{-3}s^{-1}$, $\dot{\varepsilon} = 5\times10^{-3}s^{-1}$ and $\dot{\varepsilon} = 10^{-1}s^{-1}$.

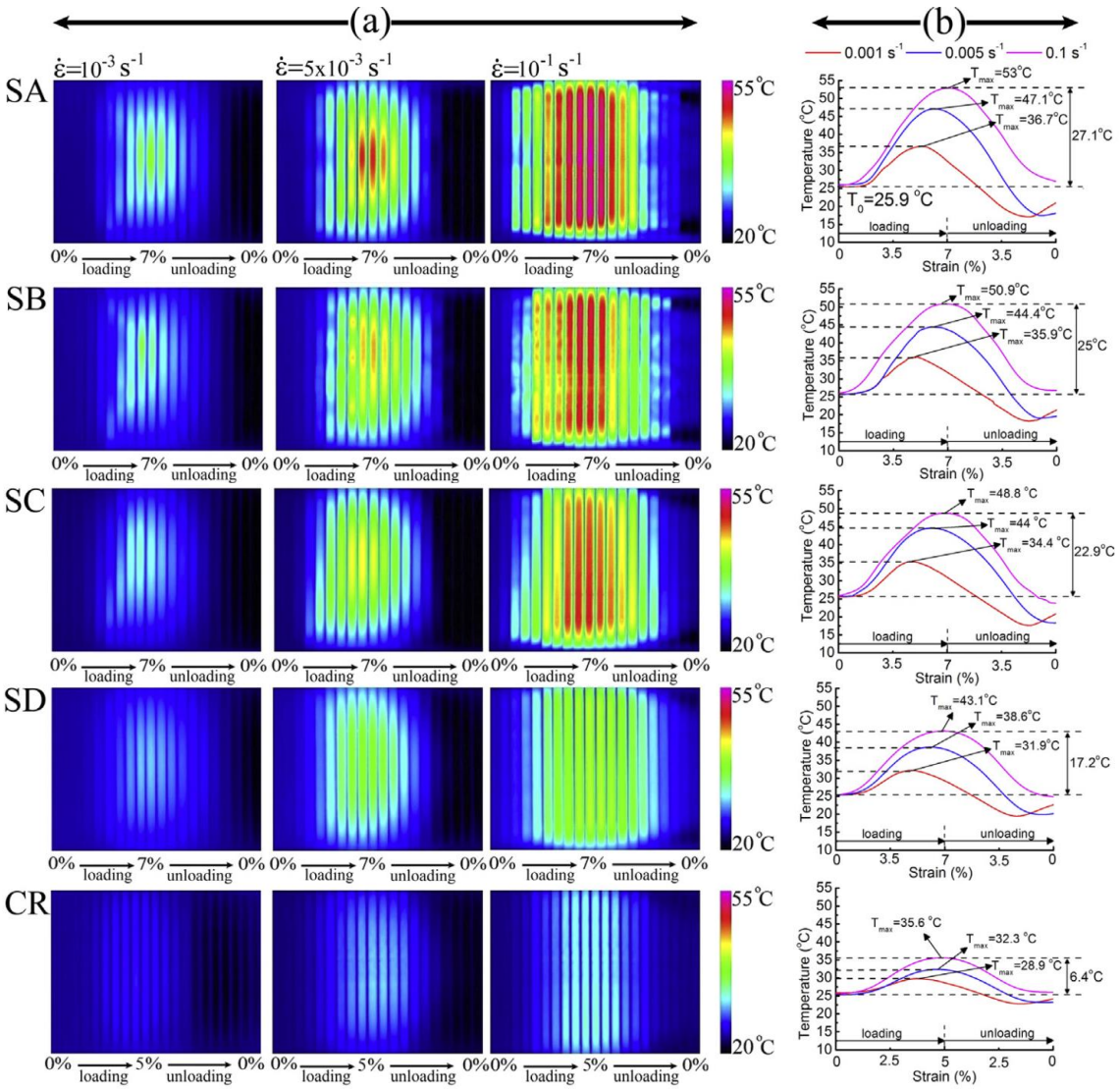

Figure 1.19: *(a) Full-field thermographic images and (b) volume - averaged temperature ($T(t)$) during loading – unloading at three strain rates of $\dot{\varepsilon} = 10^{-3}s^{-1}$, $\dot{\varepsilon} = 5\times10^{-3}s^{-1}$ and $\dot{\varepsilon} = 10^{-1}s^{-1}$ (Adapted from Ahadi and Sun, 2014)*

Analyzing Fig. 1.19 combined with Fig. 1.18, it is easily shown that the more developed is the superelastic loop, more phase transformation is present and so, more latent

heat is released. Due to this latent heat releasing, the temperature variations observed on tests increased from 17.2°C for the SD sheet (lower heat treatment magnitude) to 27.1°C for the SA sheet (higher heat treatment magnitude).

1.4 Chapter review

This chapter has presented, in the Section 1.1, some information about the characteristics of the shape memory alloys (SMA's). It was explained the mechanisms of phase transformation as well as the two main properties of these alloys, the shape memory effect (SME) and the superelasticity (SE).

The Section 1.2 presented the thermomechanical coupling during the superelasticity. In a first moment it was shown some engineering applications using this phenomenon. Further, a thermodynamic framework used to study the thermomechanical coupling was presented. Finally, some experimental studies on the thermomechanical coupling found in literature was shown.

In the last Section 1.3, the specificities of the NiTi SMA was presented. The influence of the manufacturing process and heat treatments in the microstructure of the material, as well as their impact on the thermomechanical coupling, was also presented.

CHAPTER

TWO

EXPERIMENTAL ASPECTS

Contents

2.1 Introduction

The objective of this chapter is to present in detail all the experimental aspects of the work. Section 2.2 introduces the material and heat treatments performed to obtain different mechanical properties. Section 2.3 presents the details of the uniaxial tensile test and DSC performed on the material. Section 2.4 shows the applied tools and methods to measure the kinematic and thermal full field responses of the analyzed material. Experimental details and difficulties are also discussed. Finally, section 2.5 presents a study on the repeatability of thermomechanical measurements.

2.2 Material

2.2.1 NiTi wire sample

The wire used in all performed experiments was a commercial cold worked (noted CW) $Ti - 50.9\,at.\%\,Ni$ alloy with a nominal diameter of d=0.5mm provided by Fort Wayne Metals. Figure 2.1 shows a) an example of such a NiTi wire sample and b) its mechanical behavior.

Due to its fabrication history a hardened mechanical response is observed. To overcome that and to allow the intended study, heat treatments were performed on the wire.

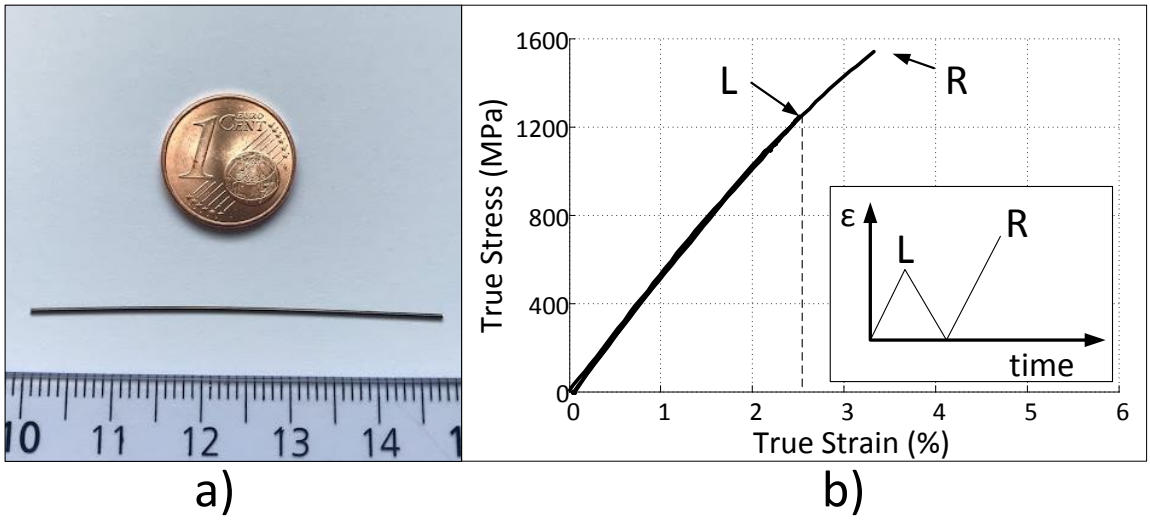

Figure 2.1: *a) Cold worked NiTi wire with a diameter of d=0.5mm. b) Tensile test of the CW NiTi wire showing in detail the loading path and their respective loading maximum (L) and rupture (R) points.*

2.2.2 Wire Microstructure

The microstructure of the cold worked wire was analyzed using a transmission electron microscopy (TEM) technique. Figure 2.2a shows a bright field (BF) picture from a high-resolution electron microscopy in which one can observe the nanosized polycrystalline microstructure of the material. Nanograins ranging from nearly 10nm to 100nm are observed.

Figure 2.2b shows the TEM diffraction pattern (DP) of the tested wire. In this picture one can observe the presence of a polycrystalline austenite phase (B2) with crystal lattice preferentially oriented in the direction (110). This result will be further discussed in Chapter 3.

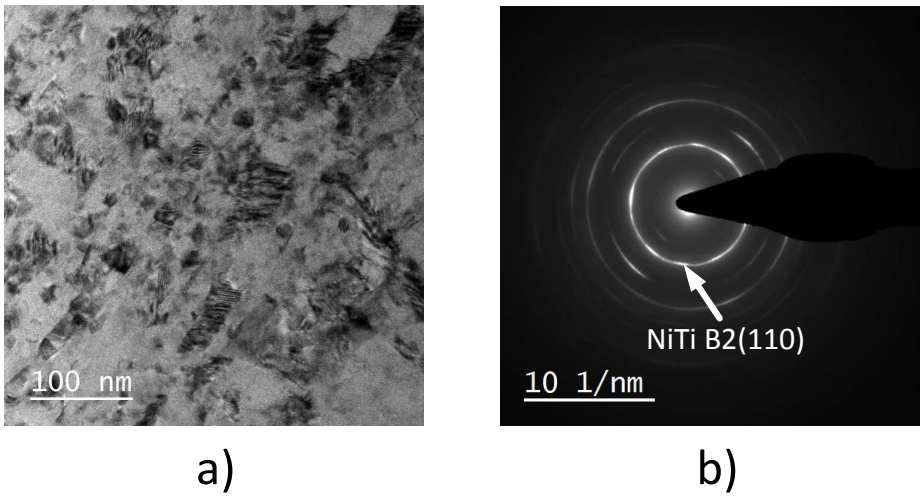

Figure 2.2: *Transmission electron microscopy showing a) a bright field picture b) and a diffraction pattern of the NiTi cold worked wire.*

The TEM tests were performed by Professor Yinong Liu from the School of Mechanical Engineering of the University of Western Australia.

2.2.3 Heat treatments

Four heat treatments were performed at $523K$, $548K$, $573K$ and $598K$ for 30min. The objective of the heat treatments was to trigger the superelastic effect on the initially cold worked material. In the following, these tests will be reported as HT523, HT548, HT573 and HT598. Figure 2.3 shows the mechanical behavior of the initial cold worked (CW) wire and the different heat treatments.

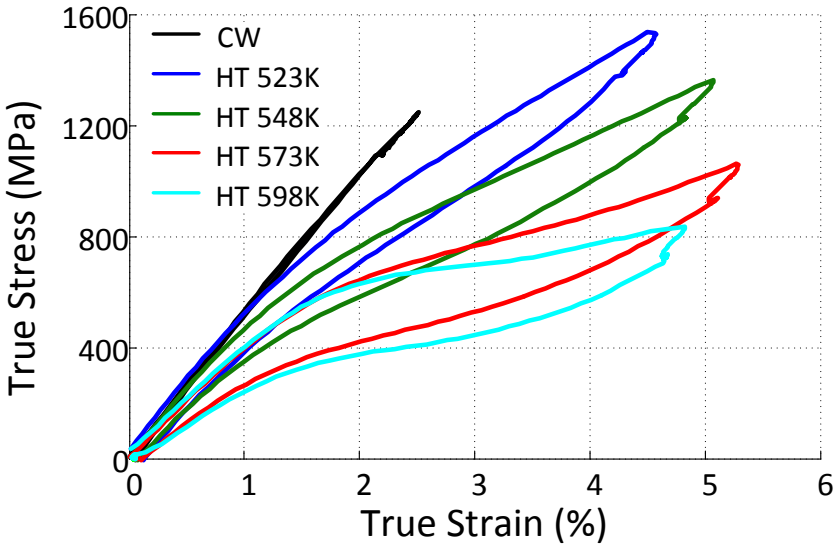

Figure 2.3: *Superelastic tensile behavior of the $Ti-50.9\,at\%\,Ni$ wire CW and submitted to different heat treatments.*

2.3 Performed tests

2.3.1 DSC test

After heat treatments, every sample was submitted to a DSC (Differential Scanning Calorimetry) analysis to investigate their thermomechanical properties. The purpose of this thermal investigation was to obtain the characteristic phase transformation temperatures (A_s, A_f, M_s and M_f) and the specific latent heat of phase transformation (ΔH).

The specific latent of phase transformation is determined by the area between the base line and the peak of heat flow vs. temperature curve. The characteristic transformation temperatures are determined from the inflection points of the curve. Figure 2.4a shows schematically the graphical method used to obtain these properties.

Figure 2.4b shows the results of DSC tests for the heat treated wires. The absence of peaks makes impossible to determine the specific latent heat using the before mentioned method.

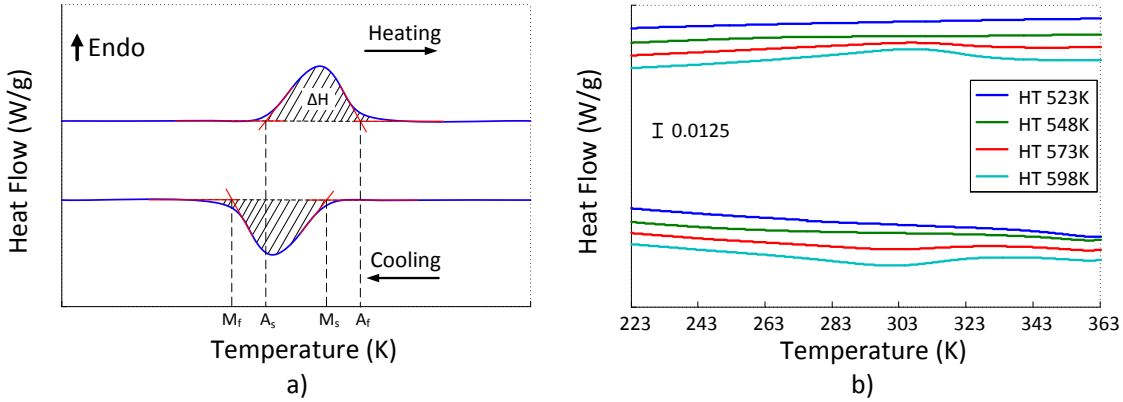

Figure 2.4: *a) Graphical representation of a classic DSC curve and methodology to determine the specific latent heat and the critical temperatures. b) Actual DSC results of heat treated NiTi wires.*

2.3.2 Uniaxial tensile tests

2.3.2.1 Test details

All tests were performed in a tensile testing machine Eplexor Gabo (see Fig. 2.5a) and carried out in controlled room temperature. During tests, two external data acquisition systems were used: an infrared (IR) camera and a visible light camera. The first one was responsible for the temperature field measurement while the second one for the strain field measurement. Despite the bigger area filmed by the visible light camera (compared to the IR camera), the analyzed area was limited by the IR camera spacial resolution (length of $l_0 = 8.2mm$).

The cameras were positioned in opposition. Each filmed "side" was coated differently. A black paint on the IR "side" and a black and white speckle painting on the visible light camera "side". The schematic representation of the tensile test with both external systems is shown in Fig. 2.5b.

The tensile test consisted in deforming the wire at a constant deformation rate up to a maximum deformation and returning to its initial (zero) deformation. Also, in order to obtain the necessary data to allow the thermal analysis, a hold time was performed after each loading and unloading. In this way, the tensile test was divided in four steps: I-loading, II-hold time, III-unloading and IV-hold time (loading: up to 6%, loading rate: $\dot{\varepsilon} = 10^{-2}s^{-1}$ and hold time: $50s$ each). The schematic representation of the loading path is presented in Fig. 2.5c.

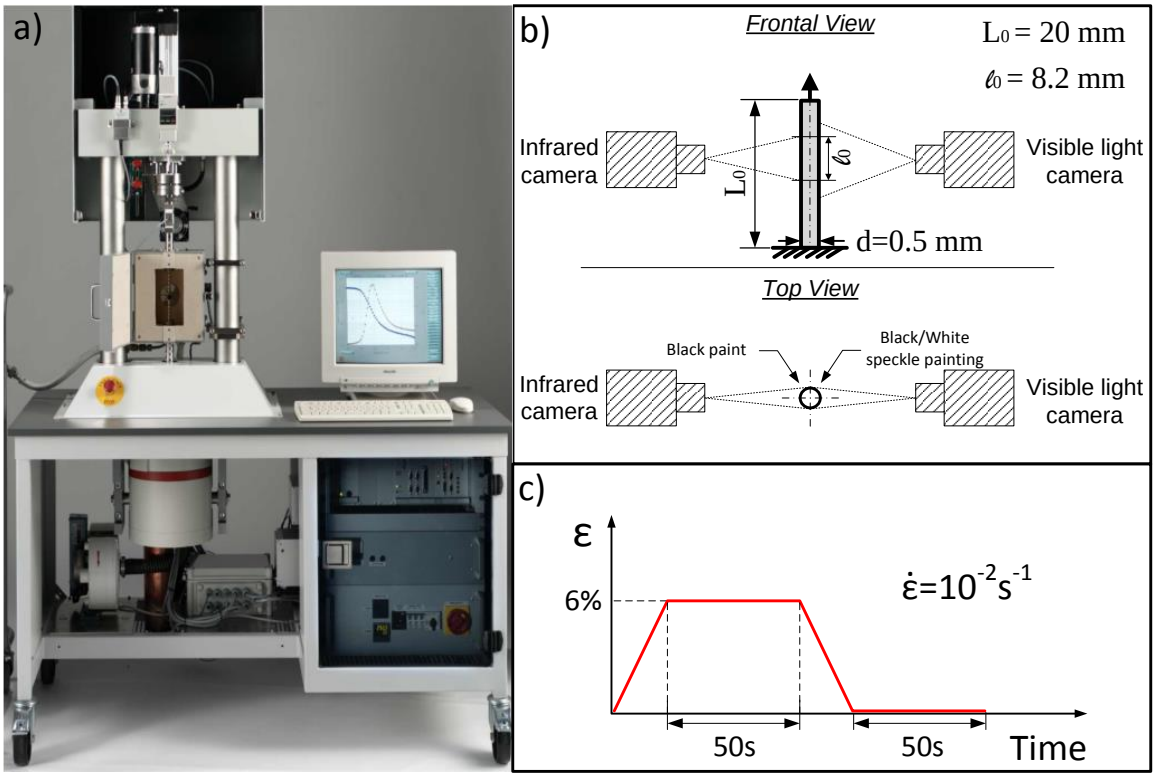

Figure 2.5: *a) Eplexor Gabo tensile testing machine. b) Schematic representation of tensile test with both infrared and visible light camera. c) Schematic representation of the loading path imposed at each test.*

2.3.2.2 Gripping system

A so called "V-clamp" was used to minimize the sliding effect on the sample/clamp interface. Figure 2.6a shows two clamp models, a "V-clamp" and a "Flat clamp". On the detail of Fig. 2.6a, one can observe that the "V-clamp" promotes 3 contact points on the sample, while the "Flat clamp" holds the sample over 2 contact points only. Because of that, the "V-clamp" promotes a higher gripping when compared to the "Flat clamp". Fig. 2.6b shows a sample mounted on the "V-clamp" used on tests.

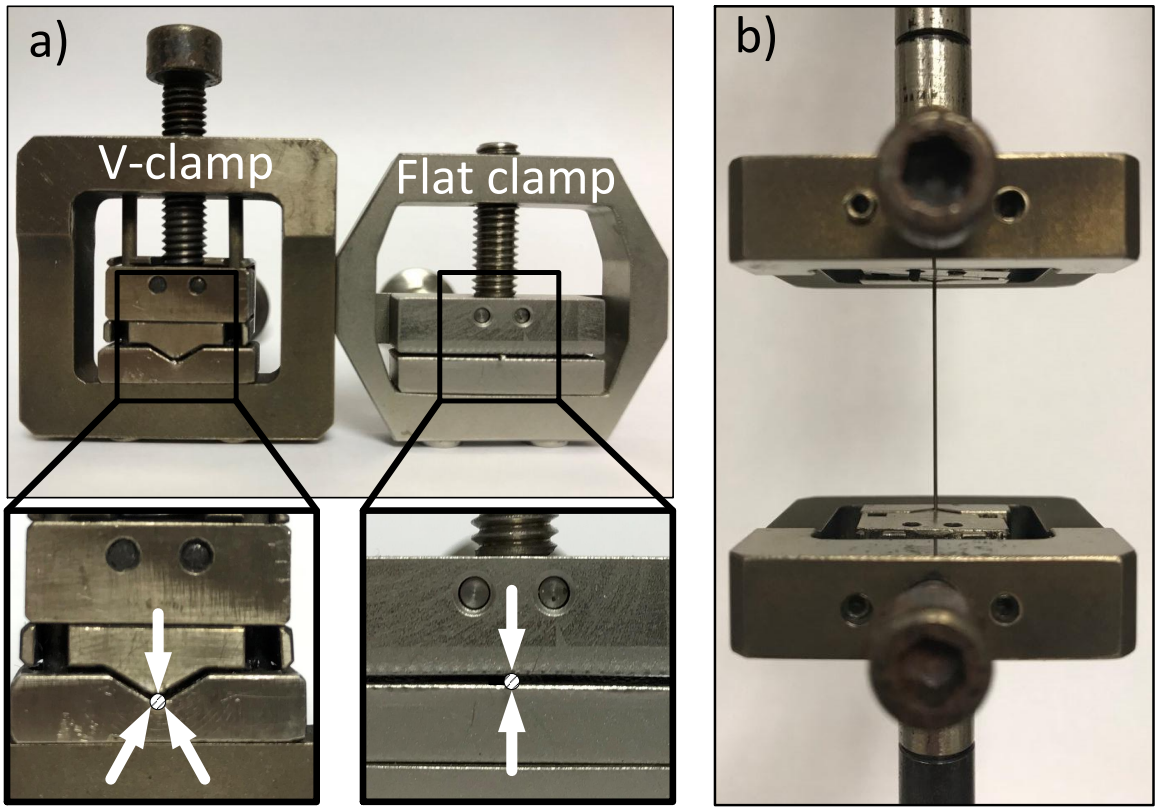

Figure 2.6: *a) "V-clamp" and "Flat clamp" models showing in detail the different contact points over the hold sample. b) sample mounted on the used clamps.*

2.4 Full field measurements

Kinematic and thermal full field measurements are commonly used nowadays to study the thermomechanical coupling in materials and structures. With this kind of approach it is possible to study localized phenomena such as necking (Chrysochoos and Louche, 2000), Luder's like bands (Chrysochoos and Louche, 2000; Louche and Chrysochoos, 2001),Portevin-Le Chatelier effect (Louche et al., 2005), phase transformation (Schlosser et al., 2007; Chrysochoos et al., 2010) and fracture.

Despite the easy implementation of these techniques at first glance, quantitative measurements are not so easily obtained. The smaller detail on the experimental implementation can affect the image quality and may hugely affect the post processing data.

The objective of this section is to present the thermal and kinematic full field techniques used in this work and the experimental issues involved. The kinematic measurement technique (from Digital Image Correlation - DIC), as well as the experimental aspects and difficulties of the developed tests are exposed in the following subsection

2.4.1. Analogously, the thermal measurement technique with its respective experimental aspects and difficulties are discussed in subsection 2.4.2.

2.4.1 Kinematic measurements

2.4.1.1 DIC method

Differently from using a strain gage, which gives a single local deformation, with this kind of tool it is possible to obtain a strain field throughout a whole surface.

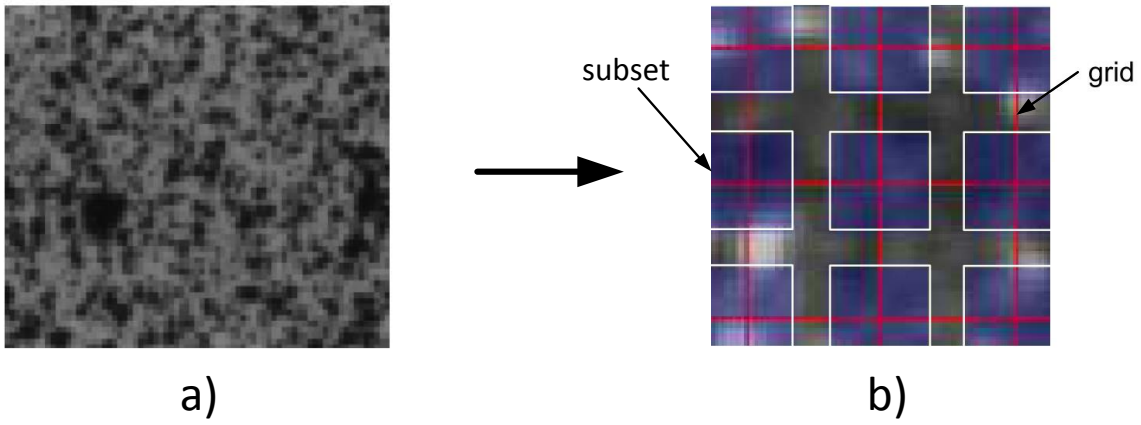

Figure 2.7: *Example of a) a speckled image; b) an applied subset and grid.*

This method consists in measuring the displacement field of an object's surface by comparing its morphology (through the analysis of its grey level) between two images prior and after deformation. The texture of the surface can be either natural or created by a painted speckle that gives a high contrast random pattern to the surface (Fig. 2.7a).

The process of displacement field determination begins by placing a virtual grid over the image, generating smaller interest zones called "subset" (Fig. 2.7b). The grid and subset sizes are typically 10 to 50 pixels, but they are strongly related to the observed texture size (speckle size). The relation between the speckled texture size and the subset size may strongly influence the measurement quality. Once the grid and subset are defined, the displacement field is calculated by the software (VIC 2D from Correlated Solutions was used in this work) through the tracking of the new position of each defined subset on the deformed image. This tracking is performed through the minimization of a correlation factor calculated from the gray level at each subset prior and after deformation. Figure 2.8 shows an example of a correlated image with its respective grid before (initial grid Fig.2.8a) and after (deformed grid Fig.2.8b) deformation. With this, displacement and strain fields can be calculated.

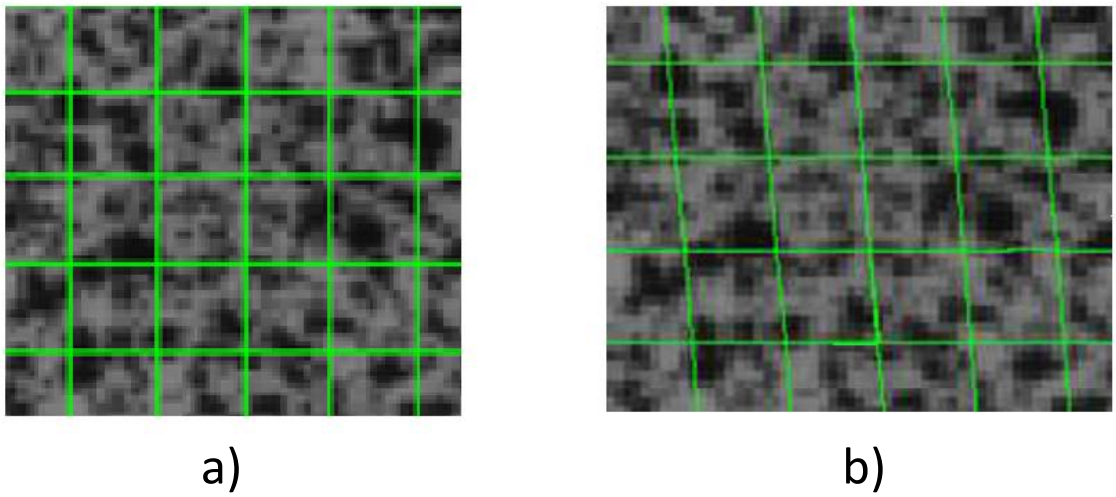

Figure 2.8: *Example of an image correlation grid a) prior and b) after shear deformation.*

2.4.1.2 Sample preparation

Sample preparation is fundamental to obtain a good result since surface texture directly affects the correlation accuracy. The texture may be from different origins: scratches on the surface, surface morphology or artificial speckle painting. Several examples of surface textures can be seen in Fig. 2.9.

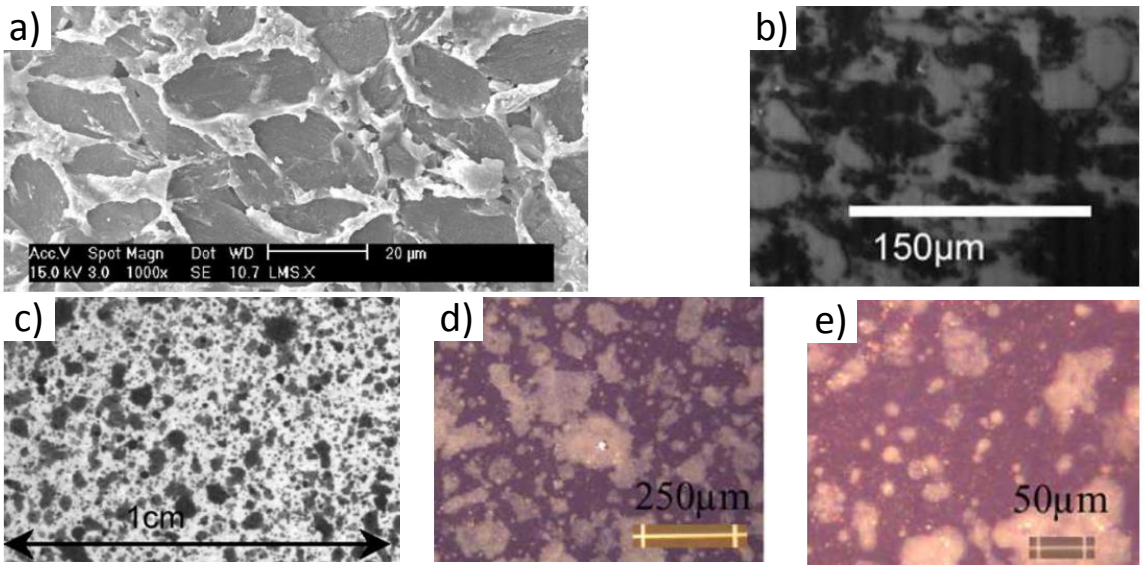

Figure 2.9: *Example of natural and artificial textures. a) Biphasic polymer. b) Rock. c-e) Speckle paintings. (Adapted from Schlosser, 2008)*

When using an artificial texture (speckle painting), it is important that the texture adheres to the surface during all test. This may be an obvious statement but it is common that paints loose its elasticity after a long dry. In this case, the texture may break and get loose from sample's surface, making measurement impossible. Because of that, it is crucial to perform tests soon after the sample preparation.

The size of random pattern also plays an important role since the deformation resolution is directly affected by its size and consequently by the subset size. This can be an issue specially in the preparation of surfaces with small dimensions, which is the case in this study. For example, preparing a 100mm x 100mm sample is much easier than a wire of d=0.5mm. In the latter case each drop of paint may have the size of the wire's diameter, reducing drastically the resolution of the measured deformation.

2.4.1.3 Experimental set-up and difficulties

To obtain a good quality artificial texture some special attention is required. As the correlation requires a good contrast, using a speckled black paint over a white surface is often more suitable than the inverse. Also, on the experiment set-up, the lightening has to be adjusted to avoid reflections or shadows on the sample to maximize the field of view, especially in the case of circular section samples (e.g. tubes and wires). Finally, a cold light source is recommended when a simultaneous thermal acquisition is performed. This prevents the heat of lightening from being absorbed by the material and interfering with the measurement.

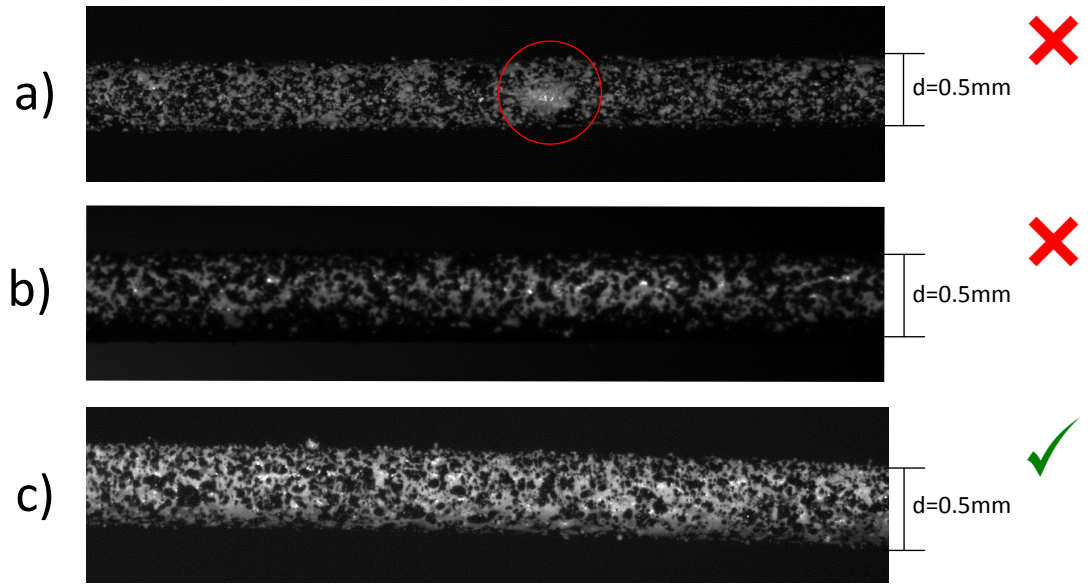

Figure 2.10: *a) Big painting spot on the speckle pattern. b) Low contrast pattern. c) Ideal speckle painting with uniform pattern and good contrast.*

Figure 2.10 shows three different speckle paint patterns of the tested 0.5mm diameter

NiTi wire. In Fig.2.10a one can observe the big drop of white paint disturbing the random speckle paint pattern. The Fig.2.10b shows a low contrast speckle paint image, which commonly produces a high noise correlation result. Finally in Fig.2.10c, one can observe an ideal speckled painting which produces a good correlation result due to its uniform pattern and good contrast. In this study, a black paint speckle over a white paint layer was used on the wire's side of the visible light camera acquisition (as observed in Fig.2.10c).

2.4.2 Thermal measurements

2.4.2.1 Infrared thermography

Infrared (IR) cameras are based on the detection of infrared light, first discovered in the early 19^{th} century. The first IR camera was created in 1964 and firstly used for military purposes in the beginning of the 1980 decade. The use of this device for measurement purposes is now largely applied in mechanics of material studies to observe localized phenomena such as phase transformation (Shaw and Kyriakides, 1997b; Schlosser, 2008; Delobelle et al., 2013), plasticity in metallic alloys (Louche and Chrysochoos, 2001; Louche et al., 2005), fatigue behavior (Berthel et al., 2008) and thermophysical properties (Delobelle et al., 2015; Delpueyo et al., 2012).

In the electromagnetic radiation spectrum, the IR wavelengths are present approximately between $0.7\mu m$ and $1mm$. The first part of this range is classically subdivided into four categories: Near Infrared (NIR) between $0.7\mu m \sim 1\mu m$, Short Wave Infrared (SWIR) between $0.9\mu m \sim 1.7\mu m$, Medium Wave Infrared (MWIR) between $2\mu m \sim 5\mu m$ and Long Wave Infrared (LWIR) between $7.5\mu m \sim 14\mu m$ *or more*. The choice of the IR bandwidth depends on the application.

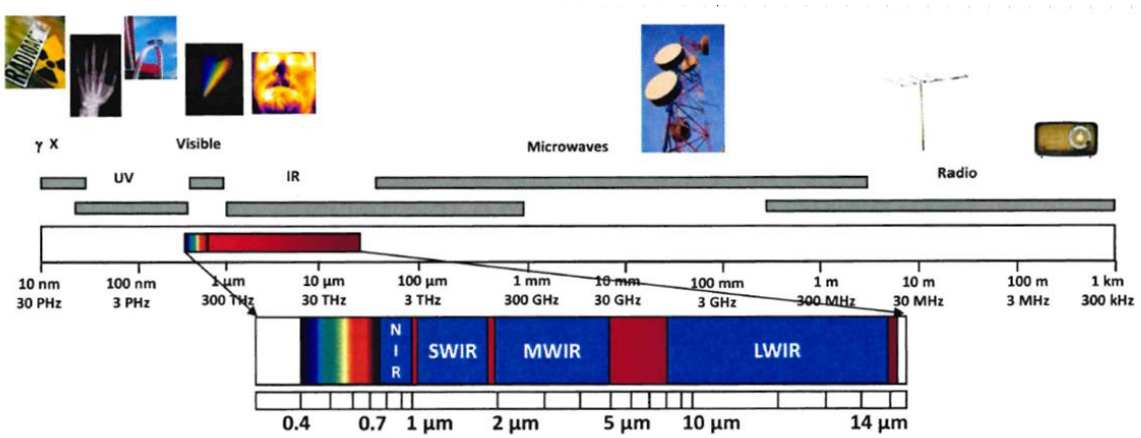

Figure 2.11: *Electromagnetic radiation spectrum.*

An infrared camera does not measure the temperature of a filmed object but the

radiation that emanates from it. However, this radiation may be coming from the object itself (heat generated) or from the environment around it through reflection or transmission phenomena. It means that when a radiation is incident on an object it can be either absorbed, transmitted or reflected as schematically shown in Fig. 2.12.

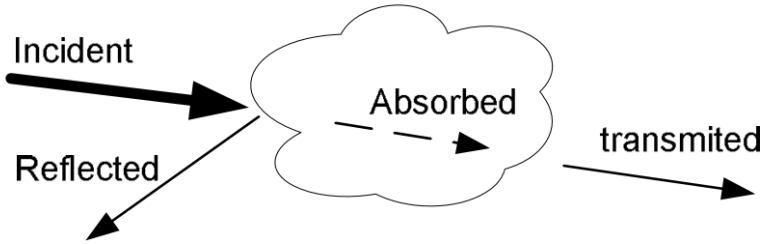

Figure 2.12: *Schematic view of the different forms of radiations. (Source: Schlosser, 2008)*

The emissivity factor ϵ represents the capacity of a body to absorb the incident IR radiation. An ideal object that absorbs all the incident radiation is called black body and its emissivity factor is $\epsilon = 1$. Any real object would have an emissivity factor $\epsilon < 1$. The emissivity of a body depends on many parameters, such as: chemical composition, wavelength, observation angle of the camera towards the surface, material temperature and surface aspect (roughness, polishing, etc). A commonly used hypothesis is that the emissivity and absorptivity of a body do not depend on the wavelength and on the temperature, and thus the emissivity is a constant. Fig. 2.13 shows the emissivity factors of typical materials.

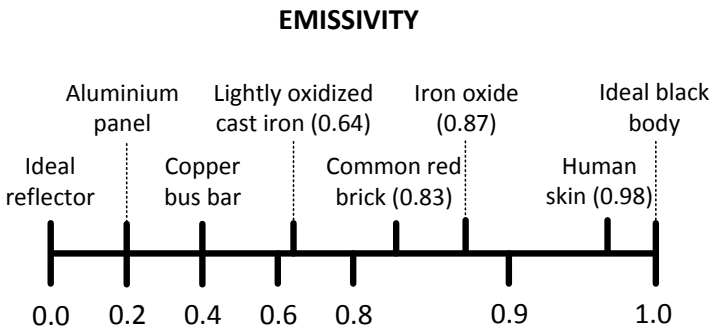

Figure 2.13: *Common emissivity values; Expanded scale between 0.8 and 1. (Adapted from: Schlosser, 2008)*

2.4.2.2 The Infrared Camera

In the present work a FLIR IR camera (model A6500sc) was chosen. It was equipped with a MWIR detector with a resolution of 640x512 pixels and a maximum frame rate of 120Hz (the acquisition rate used during tests was 30Hz).

A zoom objective lens was selected in order to observe the very small specimen. The standard objective lens provided a pixel resolution of $122\mu m$ while the zoom objective lens has a pixel resolution of $16\mu m$. This lens provided an optic increase on the field of view (FOV) of about 7.6 times compared to the standard objective lens.

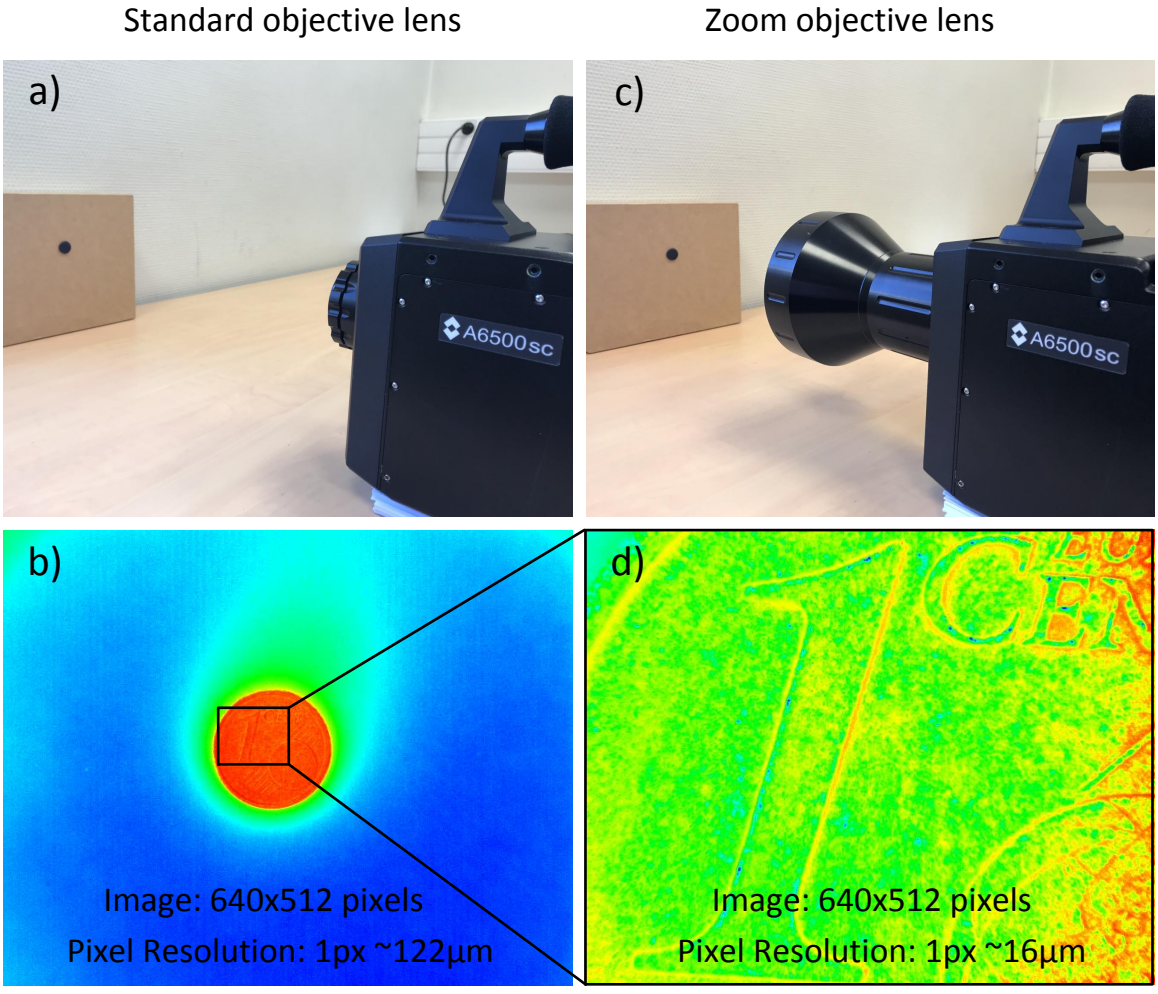

Figure 2.14: *a) Used IR camera filming a scene with a standard objective lens. b) Thermal image obtained with the standard objective lens. c) Used IR camera filming a scene with the zoom objective lens. d) Thermal image obtained by the zoom objective lens.*

Figure 2.14 shows the difference between a scene observed with a standard objective

lens and the zoom objective lens. Figs. 2.14a and 2.14b show the scene (1 cent euro coin) and its respective IR image obtained by the standard objective lens. Figs 2.14c and 2.14d show the same scene filmed by the zoom objective lens and its respective IR image with detail enhancements.

2.4.2.3 Sample preparation and experimental cautions

In this study the sample used (NiTi wire) presented a polished surface and so a low emissivity factor. The samples were covered with a thin layer of a high emissivity black paint on the IR measurement side of the sample. This technique, commonly applied in thermography, allowed to obtain a gray body condition with an emissivity coefficient higher than $\epsilon > 0.95$.

Due to the emissivity smaller than 1, the measured body may reflect the surroundings heat. Because of that, the sample's surrounding was insulated during tests. When performing the simultaneous DIC, LED lights were used to illuminate the scene (LED light promotes a colder light source when compared to incandescent light bulbs). Finally, the test operator was not positioned behind the filmed scene to avoid heat interference.

2.4.2.4 Camera calibration

The infrared camera has a matrix of detectors which translate the IR radiation into temperature. However, to reach this, some calibration procedures must be taken.

2.4.2.4.a Reading IR signal

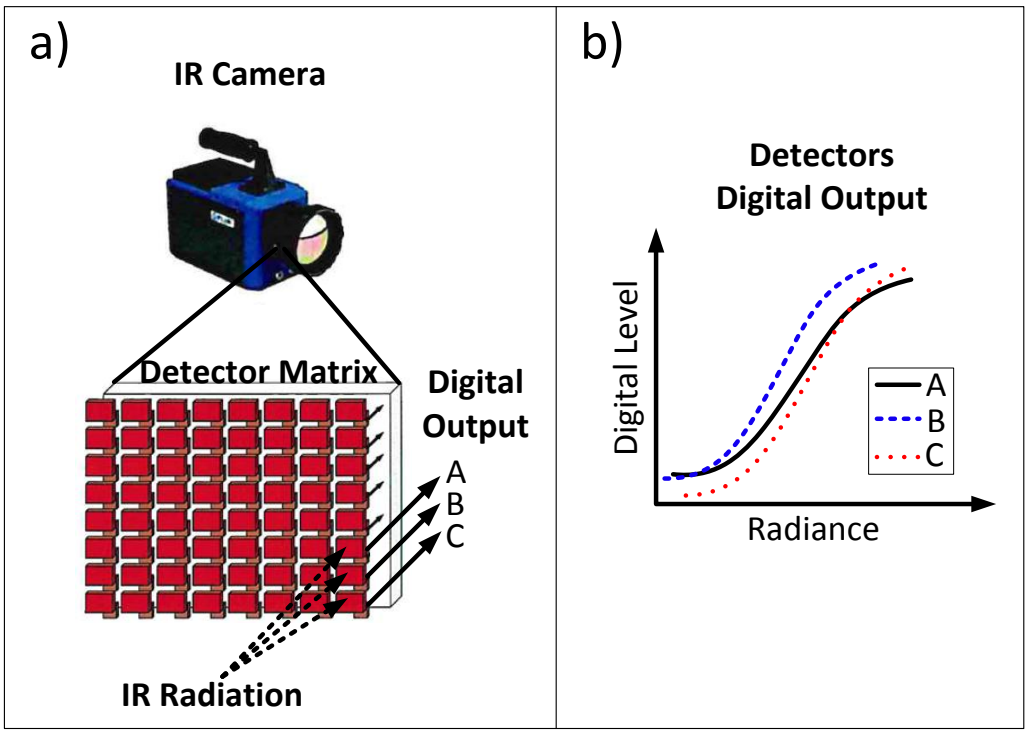

Figure 2.15: *a)Schematic representation of an IR camera detector matrix b) and its respective digital signal output.*

Figure 2.15a shows a schematic representation of an IR camera operation. The incident IR radiation on each detector is transformed in a digital output signal read by the circuit's camera. Each detector acts as a temperature probe and responds to the absorbed IR radiation independently. Fig. 2.15b shows for three detectors (A, B and C) a schematic representation of the digital level in function of the radiance (IR radiation). One can observe the random behavior shown by each detector. Because of that, a so called Non-Uniformity Correction (NUC) has to be performed in order to align each detector output signal.

2.4.2.4.b Signal correction

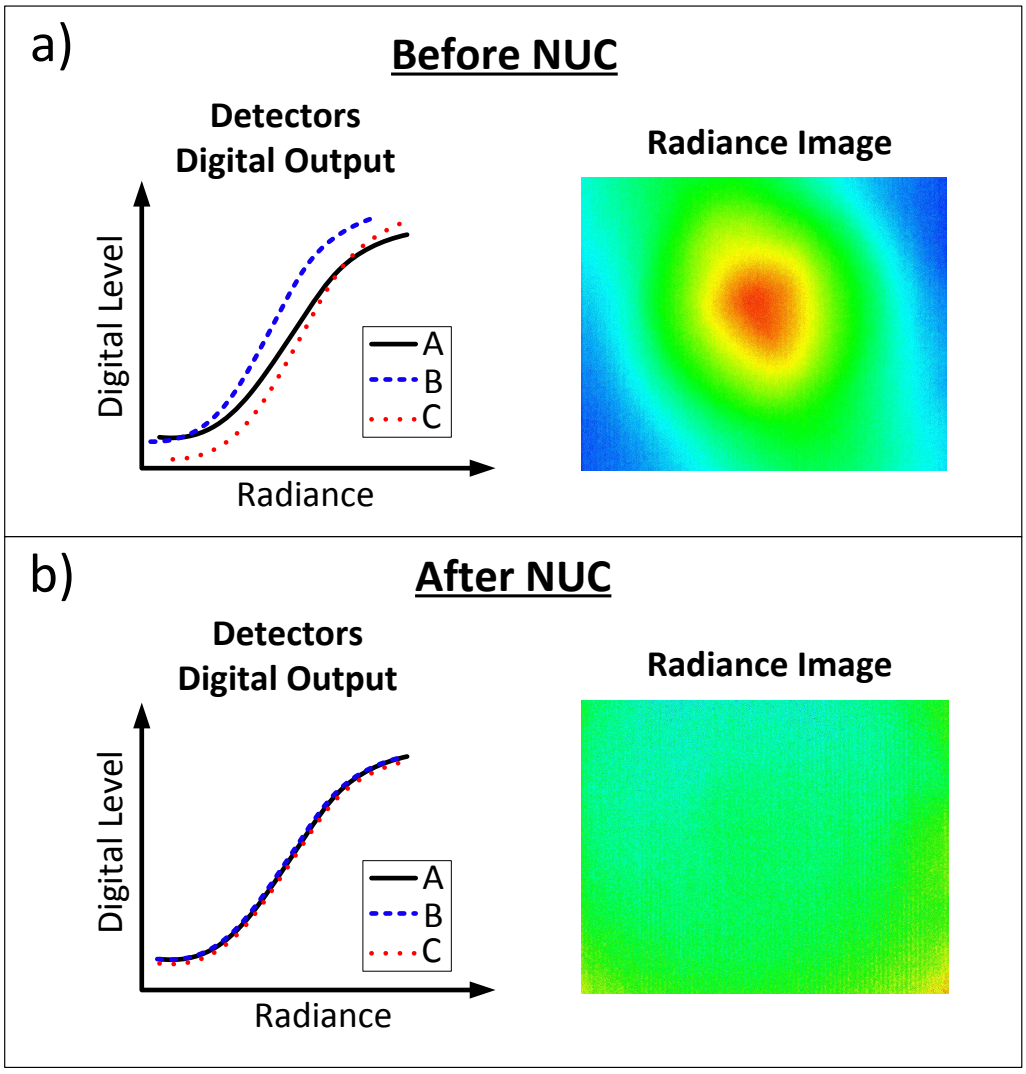

Figure 2.16: *a) Schematic representation of the digital output and an example of a radiance image before NUC b) and after NUC.*

The NUC procedure consists in submitting all the captors to two IR radiation levels, i.e. to film a uniform black body at two constant temperatures. Basically, the camera's software uses the two temperature levels to correct the gain (curve slope) and the offset (distance between the curves) of the measured signals.

Figure 2.16a shows the schematic representation of the random digital output of the detectors and an example of radiance image generated before the NUC procedure. Despite filming a black body surface with uniform temperature, the radiance image shows a non-uniform response.

After performing the NUC procedure, the detectors output signal are aligned and

show the same digital level between them. Fig. 2.16b shows the schematic representation of the aligned digital output responses and an example of radiance image after the NUC procedure. In this case, it is possible to observe the uniformity on the radiance image.

2.4.2.4.c From radiance to temperature

After the NUC procedure a temperature calibration must be performed. It consists in filming a black body in several temperature in a given range. Automatically, the camera's software draws a curve of digital level vs. temperature and find its equation. In this study, the camera was calibrated in a temperature range between $268K$ and $318K$.

2.4.2.5 Data processing

The raw data obtained by the IR camera was processed in the MATLAB environment. A code was developed to identify the wire on every image and further obtain the value of temperature along its surface.

In the following, preliminary thermal images will be presented as temperature variation fields $\theta(x, y, t) = T(x, y, t) - T_0(x, y, t)$ where T and T_0 are the temperature fields at the current time t and the initial time t_0, respectively. The spatial positions in pixel are noted x for the circumferential direction and y for the longitudinal direction.

2.4.2.5.a Identifying the wire on thermal image

Figure 2.17a presents an example of the processed infrared image showing the tested wire in the center. As one can notice, the wire is distinguished on the image because of the difference between its temperature and the background. When tracing the circumferential temperature profile, one can observe (see Fig. 2.17b) that the image's background is around $300K$ (at this specific instant) while the wire is at $307K$. So, by calculating the spatial derivative of the temperature profile along x direction 2 peaks are obtained as it can be seen in Fig. 2.17c. From that, the peaks named $p2$ and $p3$ represent the initial and final positions of the wire when sweeping the thermal image from left to right.

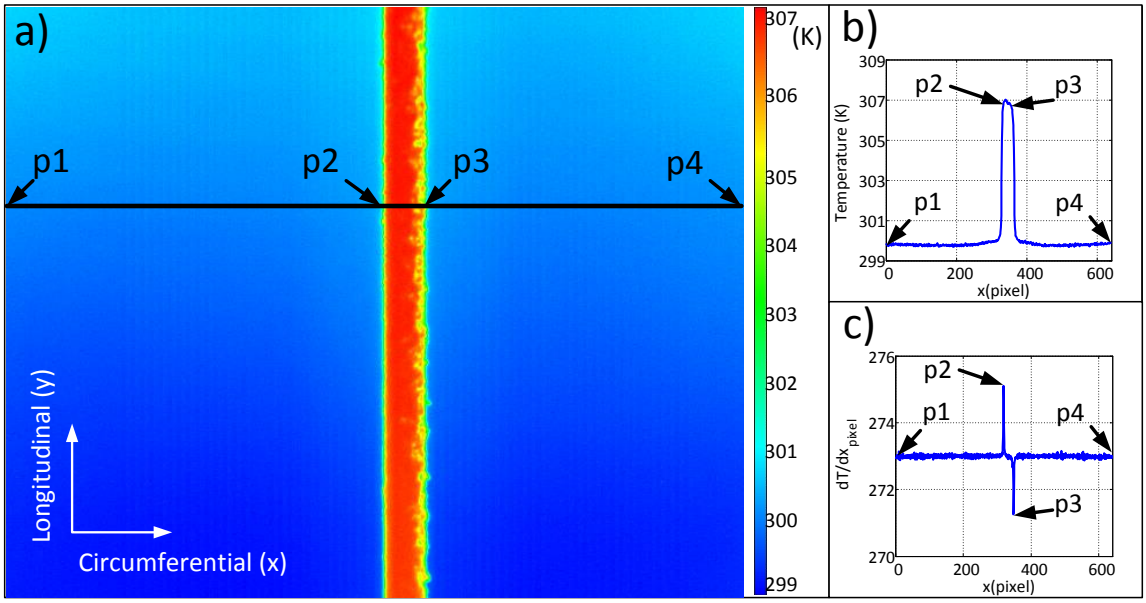

Figure 2.17: *a) Example of thermal image of a tested wire. b) Temperature profile of the blue line shown in a). c) Spatial (x direction) temperature derivate curve used to determine the wire's position on thermal image.*

2.4.2.5.b Mean temperature estimation

On the detail of Fig. 2.18b, it is possible to observe the wire occupying 30 pixels on the image width. However, temperature is not uniform along the whole profile as shown by Fig. 2.18c. A lower temperature is observed at the extremity of curve (approximately after pixel 20). This decrease is due to the emissivity variation along the wire's surface, due to the experimental procedure of painting one "side" of the wire with black paint (for IR acquisition purpose) and the other "side" with the white (which has lower emissivity) and black speckle painting (to perform DIC analysis). To overcome this problem, it was simply decided to use data from the wire's zone with a uniform temperature, avoiding the non-uniform emissivity zone.

After analyzing the circumferential temperature profiles, longitudinal temperature profiles were plotted. For each image, the longitudinal profile was obtained by averaging the circumferential profiles. In other words, each point of the longitudinal profile (at y direction) was obtained by the mean value of the circumferential profile at the y pixel position.

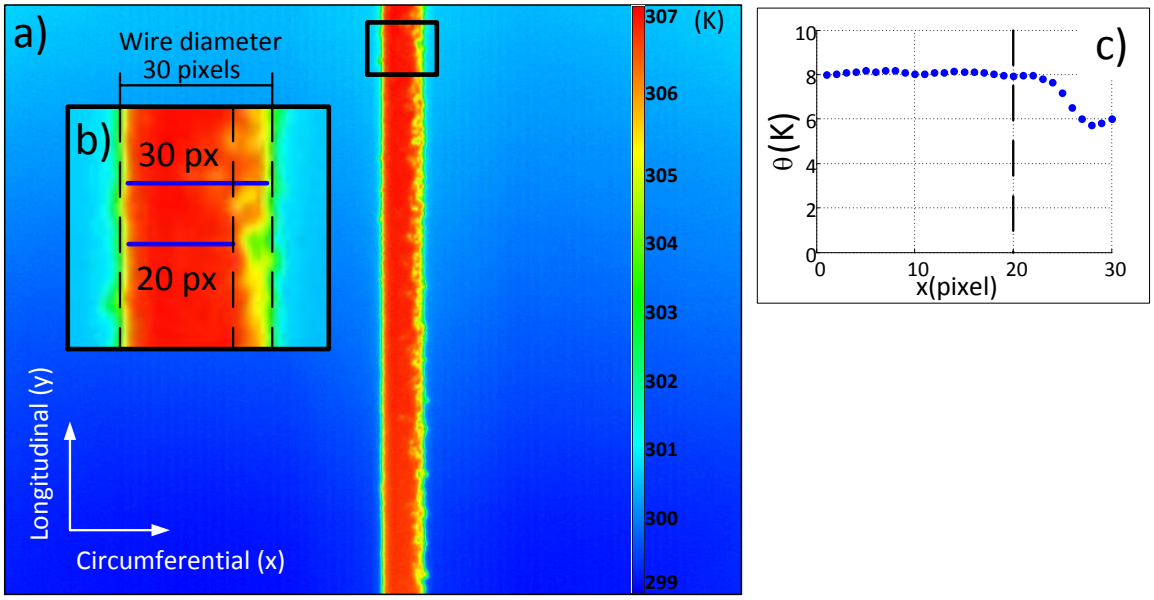

Figure 2.18: *a) Example of thermal image of a tested wire. b) Detail showing the* 30 *pixels in the wire's diameter and the* 20 *pixels used to avoid the image's non uniform emissivity zone. c) Temperature profile of the* 30 *pixels line shown in b).*

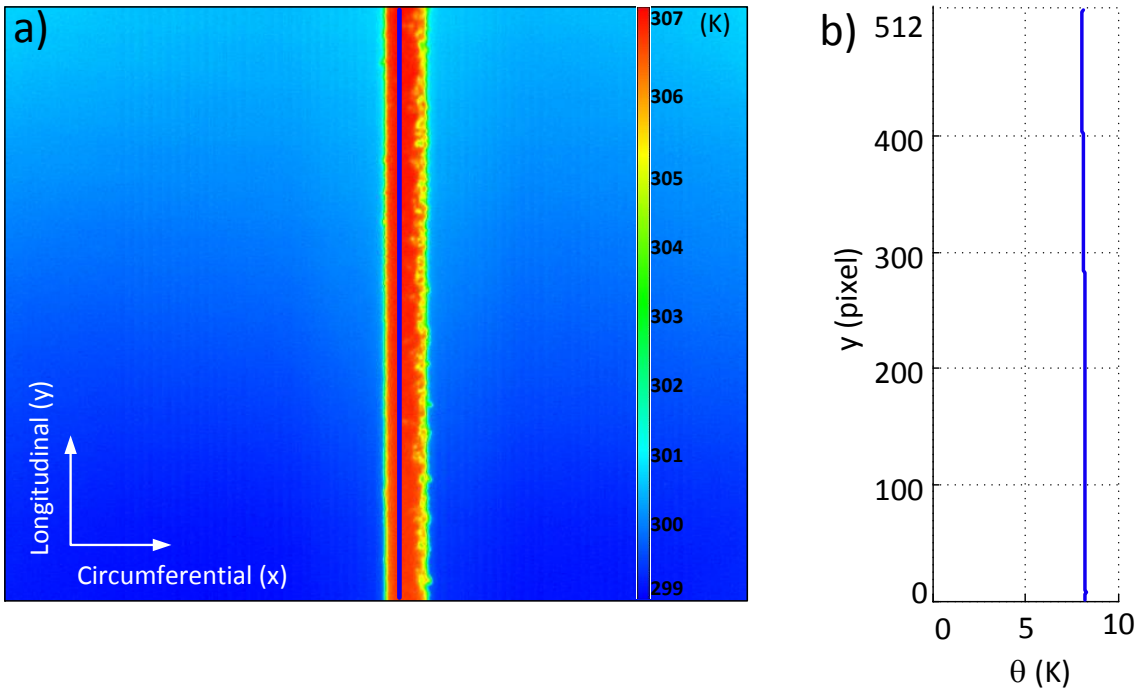

Figure 2.19: *a) Example of thermal image of the tested wire showing a longitudinal profile (blue line), b) and its respective longitudinal temperature profile.*

Figure 2.19a presents a line traced along the longitudinal direction of the wire and its respective temperature variation in Fig. 2.19b. As it can be observed, the obtained temperature was uniform along the y direction. Because of that, the temperature was treated as independent of the y position and it was averaged along the wire longitudinal y direction.

Finally, the wire temperature variation during the test was calculated by the mean temperature variation ($\theta(t)$) of the longitudinal profile at each image. Fig. 2.20 shows the temporal mean temperature evolution of a tested wire.

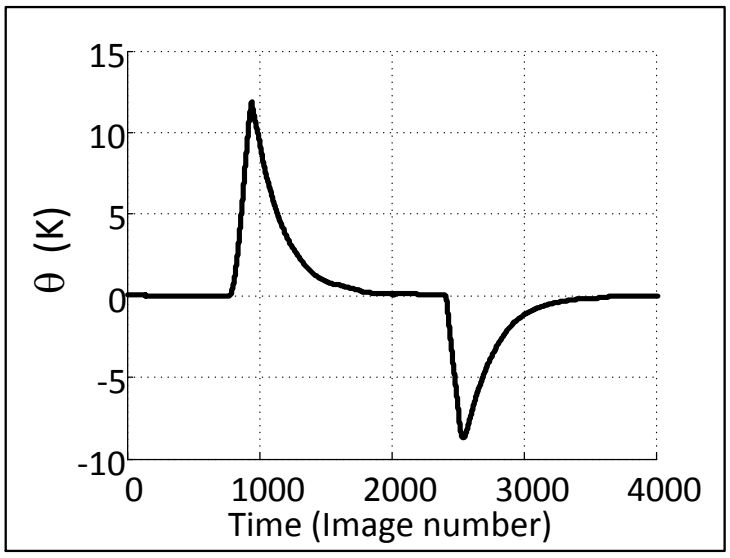

Figure 2.20: *Wire's average temperature variation at each image.*

2.4.2.5.c Lost images during data acquisition

Infrared images acquisitions are made through a software provided by the camera manufacturer. As the camera is capable of a high acquisition rate, the software has two acquisition modes. The first one consists in writing every image directly on the computer's hard disk. The advantage of this mode is unlimited data acquisition (limited by the hard disk capacity). However, as the hard disk shows a low writing speed, for high rate acquisition, several images may be lost on the process. Because of that, a second acquisition mode is suggested for high rate acquisition. It consists in writing every image on the computer RAM memory, which presents a much faster writing speed. However, this mode is restricted to a limited number of data acquisition per test (10000 images). Even though, at high acquisition rates, some images may be lost also in this acquisition mode. The second acquisition mode was used in this work to minimize the number of lost images.

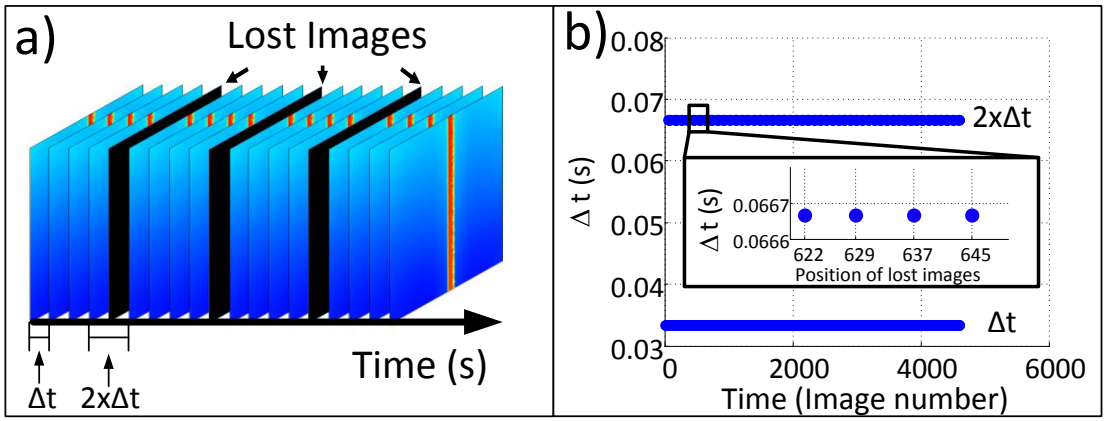

Figure 2.21: *a) Schematic representation of lost images during thermal data acquisition. b) Example of data showing time difference between images.*

Figure 2.21a shows a schematic representation of images lost during a test. This phenomenon is random and is present along the whole test duration. For example, in a test performed for this work, in a total of 4300 acquired images, 230 have been lost. To overcome this problem, a MATLAB code was developed to replace the lost data by linear interpolation of the data before and after the lost images.

The developed method consisted on identifying the gap position (on time) and adding the interpolated data in it. As the data were acquired in a constant frequency of $30Hz$, the normal time between images was $\Delta t = 1/30s$ which is approximately $\Delta t = 0.0333s$. Analyzing the values of Δt along the data acquisition, it was observed that some values were two times bigger $\Delta t = 0.0667s$. In these cases, it was confirmed that some images have been lost. Figure 2.21b shows an example of the time difference between images during a test. The bottom line shows the values of $\Delta t = 0.0333s$, meaning that time between images were as expected, however, the top line shows a value of $\Delta t = 0.0667s$, which means that the time between these images were the twice expected. From that, as one can observe on the detail of Fig. 2.21b, it was possible to determine in which position, these images were lost, in this case, at the positions: 622, 629, 637 and 645.

After identifying the position of the lost data, the mean temperature was interpolated and placed in the vacant position. Figure 2.22 shows the difference between the raw data (black curve) and the corrected data (red curve). The cumulative nature of the problem can be noticed by the increase of the gap between the first and second temperature peak. The correction of this problem was fundamental for the perfect temporal synchronization, further discussed in section 2.4.3.2.

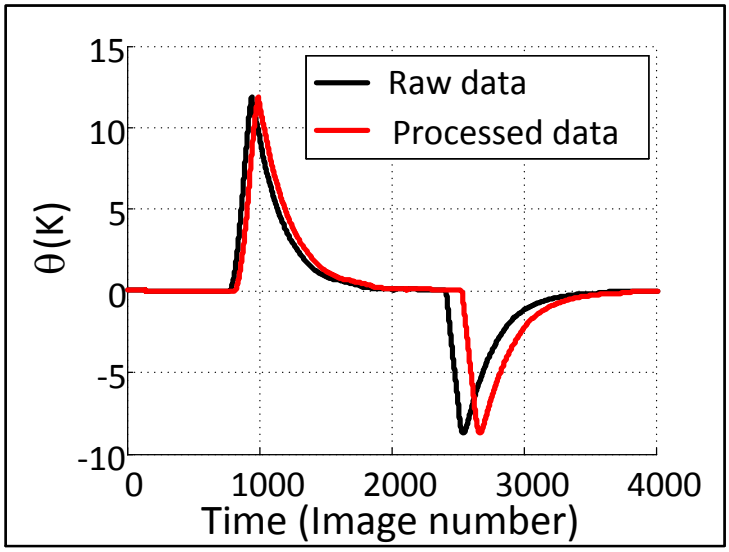

Figure 2.22: *Example of the experimental data before (black curve) and after (red curve) fixing lost image problem.*

2.4.3 Simultaneous kinematic and thermal measurements

2.4.3.1 Set-up and issues

During the tests, several data were recorded, using different temporal and spatial resolutions, through two acquisition systems (Fig. 2.23).

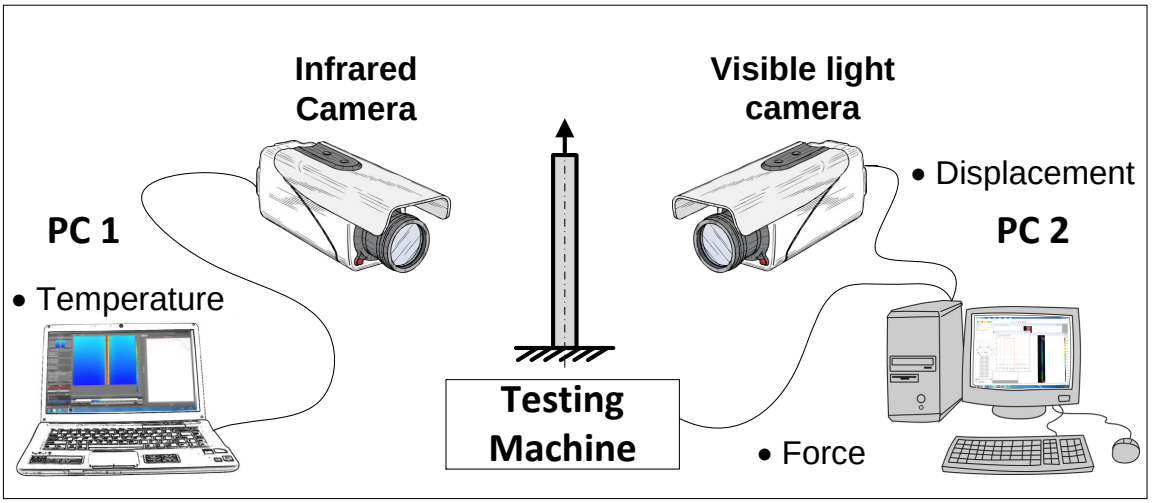

Figure 2.23: *Schematic representation of the two acquisition systems.*

- **PC 1:** Thermal images were acquired by the infrared camera at a frequency of $f_{IR} = 30\text{Hz}$ for all tests. Image acquisition started at a time $t_{0(IR)}$.

- **PC 2:** Visible light images were acquired at a frequency of $f_{Vis} = 10\text{Hz}$ in all tests. Those images were then used by a DIC software to obtain the displacement and strain fields. Force was also acquired and automatically synchronized with strain fields by the same software. Image and force acquisition started at a time $t_{0(kin)}$, where "kin" stands for "kinematic" field.

In order to analyze the thermomechanical coupling, a synchronization of both data was necessary. As the acquisition was made separately and with different frequency rates, the temporal synchronization was made manually as presented in the following section 2.4.3.2. Due to the uniform nature of the acquired thermal field, spatial synchronization was not necessary (Schlosser, 2008).

2.4.3.2 Temporal synchronization

As the acquisitions were made independently, without a hardware synchronization, the initial time (t_0) was different for thermal and kinematic data. The synchronization was made manually and consisted in finding a characteristic event to determine the test beginning. For that, the beginning of test was set for the kinematic field, as the first point of the increasing deformation curve and for the thermal field as the first point of temperature variation.

Due to the constant acquisition rate of both systems (after fixing the issue of lost images during thermal acquisition, discussed in section 2.4.2.5.c) time synchronization was easily obtained after determining the test beginning.

Figure 2.24 shows an example of the experimental data before (see Fig. 2.24a) and after (see Fig. 2.24b) synchronization. One can observe on the detail of Fig. 2.24a that the time gap between the two signals is $7.5s$. Then, after determination of the test start, both signals presented the same initial time $t_{0(kin)} = t_{0(IR)}$ (see detail in Fig.2.24b).

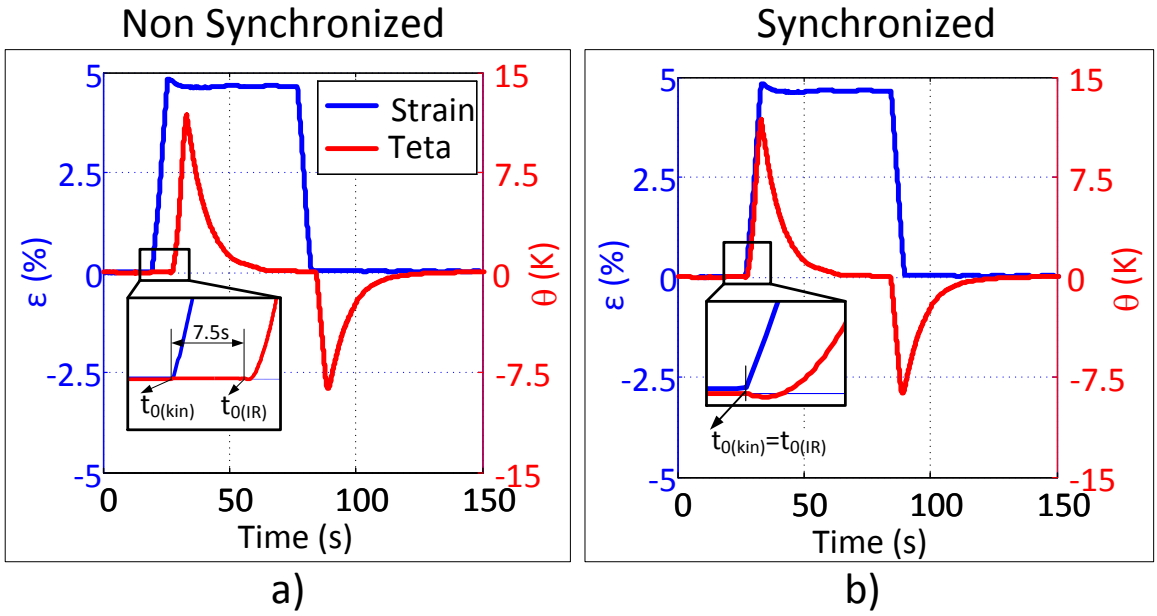

Figure 2.24: *a) Example of experimental data with both axial strain (ε) and temperature variation (θ) before synchronization. b) and after synchronization.*

2.5 Repeatability of thermomechanical measurements

To investigate the repeatability of the experimental results, three tensile tests were performed under the same conditions (with the four steps described in section 2.3.2.1). These tests were performed in wires submitted to the heat treatment of $598K$ for 30 min.

The mechanical responses of the three samples (named $HT523-1$, $HT523-2$ and $HT523-3$) are presented in Fig. 2.25. One can notice qualitatively the same behavior for the three tested samples. Despite the lightly difference, a weak scattering with a standard deviation reaching 3% of the stress value is observed.

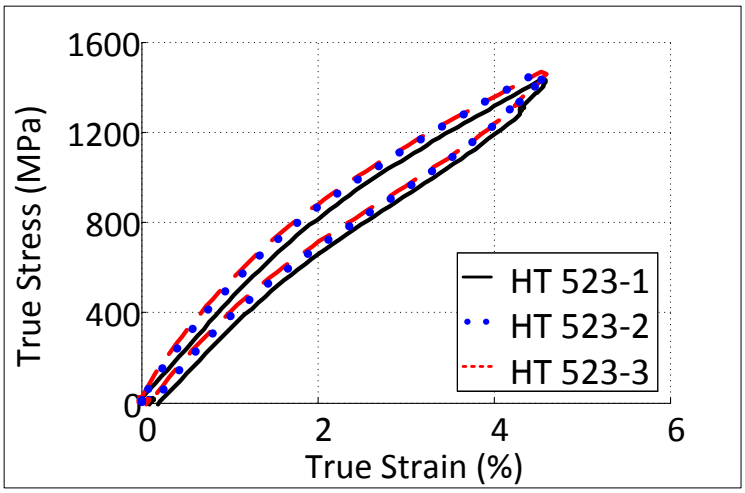

Figure 2.25: *a) Tensile test performed under same conditions on three wire samples.*

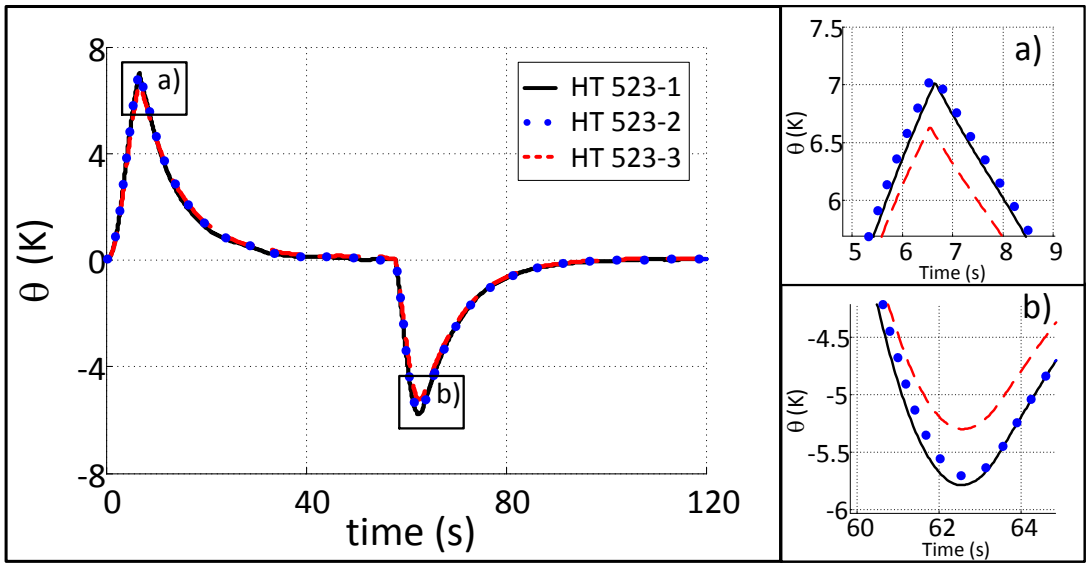

Figure 2.26: *Temperature variation over time of the three tested wires with detail over the a)upper peak and b) lower peak.*

Analogously, the temperature variations reported in Fig. 2.26 show qualitatively the same behavior between the samples. Even if the absolute temperature reached at the peak is lower for the $HT523-3$.

2.6 Chapter review

This chapter presented all the aspects of the experimental procedures used in this work. The used material, the performed heat treatments as well as the thermal and mechanical tests.

It was shown the superelastic response of a initially cold worked wire and the constant evolution of its behavior with different heat treatments. The details of the uniaxial tensile tests were also presented.

Full field measurement techniques such as digital image correlation (DIC) and infrared thermography have been described. Details of the experimental set-up and difficulties were presented for both techniques.

Concerning the DIC method, the issue of measuring the strain field on a tiny surface, such as $0.5mm$ diameter wire, was take into account by the difficulties of creating a speckle painting on its surface.

For the infrared measurement technique, several aspects have been detailed such as: the infrared camera operation, its calibration, the sample preparation and the experimental precautions. It was also described the post processing of the data in order to obtain the temperature variation of the measured sample as well as problematics of the signal synchronization.

The results of a brief study on the repeatability of the thermomechanical measurements have also been shown.

The experimental results of the simultaneous temperature and strain fields measurements will be presented and analyzed in the further chapters. Chapter 3 will show in more detail the procedure used to estimate the heat sources of phase transformation and the martensitic fraction in the wire submitted to the heat treatment of 598K for 30min. Chapter 4 performs the same analysis for the other heat treatments.

CHAPTER

THREE

SPECIFIC LATENT HEAT AND MARTENSITE FRACTION DURING UNIFORM CYCLIC SUPERELASTIC TENSILE DEFORMATION OF NANOSTRUCTURED NITI WIRES

This Chapter is written as a paper to be published soon.

ABSTRACT

Superelastic NiTi wires are manufactured by a sequence of hot and cold drawing which induces on the material a mixture of amorphous phase and highly strained nanocrystals. The present work analyses the thermomechanical tensile behavior of a cold rolled $Ti - 50.9\,at.\%\,Ni$ wire submitted to a heat treatment at 598 K for 30 min, which is below the recrystallization temperature (623 K). Such low temperature heat treatment promotes a fully superelastic loop without stress plateau and no Luders-like deformation. The specific latent heat in such nanostructured materials cannot be measured using Differential Scanning Calorimetry method due to the absence of peaks in the heat flow vs. temperature curve. In this work, a method using Digital Image Correlation (DIC) and Thermal Field Measurement (TFM) was developed and used to determine during superelastic tensile tests thermal power and thermal energy through a heat balance. From these results and using a thermodynamic approach, forward and reverse specific latent heats and martensite fraction in function of strain and stress were estimated.

Keywords: *Kinematic and thermal full field approach, heat balance, enthalpy of transformation, superelastic NiTi, non-localized strain, nanostructured NiTi wires.*

NOTATION

L_0 (mm)	Sample gauge length	$\Delta\varepsilon_{tr}$ (–)	Transformation strain
l_0 (mm)	Observed length	f_m (–)	Martensite fraction
E (GPa)	Elastic Modulus	$\dot{f_m}$ (s^{-1})	Martensite fraction rate
ρ (kg/m^3)	Mass density	τ_{eq} (s)	Characteristic time
T_0 (K)	Initial/room temperature	$\frac{\partial\langle\theta\rangle}{\partial t}$ (K/s)	Mean temperature derivative on time
T (K)	Measured temperature	$\dot{q}$ (W/g)	Heat source / total thermal power
θ (K)	Temperature Variation $(T - T_0)$	$\dot{q}_{thel}$ (W/g)	Thermoelastic power
$\langle\theta\rangle$ (K)	Mean temperature from temperature profiles	$\dot{q}_{tr}$ (W/g)	Transformation thermal power
σ (MPa)	Nominal stress	E_{th} (J/g)	Thermal energy
σ_F (MPa)	Stress at middle of plateau for the forward transformation	P_{mech} (W/g)	Mechanical power
σ_R (MPa)	Stress at middle of plateau for the reverse transformation	E_{mech} (J/g)	Mechanical Energy
$\dot{\sigma}$ (MPa/s)	Stress rate	E_{st} (J/g)	Elastic energy released or stored
ε (–)	True/Logarithmic strain	W'_{mech} (J/g)	Mechanical work
$\langle\varepsilon\rangle$ (–)	Mean strain from strain profiles	ΔH_{tr} (J/g)	Specific latent heat
$\dot{\varepsilon}$ (s^{-1})	Strain rate $\dot{\varepsilon} = d\langle\varepsilon\rangle/dt$	ΔH_{tr}^{A-M} (J/g)	Specific latent heat from austenite to martensite
$\dot{\varepsilon}_{el}$ (s^{-1})	Elastic strain rate $\dot{\varepsilon}_{el} = \dot{\sigma}/E$	ΔH_{tr}^{M-A} (J/g)	Specific latent heat from martensite to austenite
$\dot{\varepsilon}_{in}$ (s^{-1})	Inelastic strain rate	ΔH_{F-R} (J/g)	$\Delta H_{tr}^{A-M} - \Delta H_{tr}^{M-A}$
$\dot{\varepsilon}_{tr}$ (s^{-1})	Transformation strain rate $\dot{\varepsilon}_{tr} = \dot{f_m}\Delta\varepsilon_{tr}$	ΔH_{F-R}^{m} (J/g)	$\frac{1}{\rho}\sigma_F\Delta\varepsilon_{tr} - \frac{1}{\rho}\sigma_R\Delta\varepsilon_{tr}$

Contents

3.1 Introduction

NiTi shape memory wires are manufactured through a process of hot (Ahadi et al., 2012) and cold working (Delville et al., 2010; Mitwally and Farag, 2009). Usual industrial wires are submitted to a further high temperature heat treatment (annealing), above 623K. Such a heat treatment promotes a fully recrystallized microstructure (Peterlechner et al., 2010; Shi et al., 2014; Sergueeva et al., 2003; Yu et al., 2016). During heating and cooling of these annealed NiTi wires, an austenite to martensite phase transformation occurs and a large amount of latent heat is released or absorbed. These forward and reverse latent heats are commonly quantified through a Differential Scanning Calorimetry (DSC) test. These annealed wires stretched in tension are capable of achieving large amounts of pseudoelastic deformation associated to a stress-induced phase transformation (SIPT). The pseudoelasticity, also called superelasticity, is the ability of the material to undergo a phase transformation when an external stress is applied. Superelastic tensile deformation of annealed NiTi wire is accompanied by a forward stress plateau during loading and a reverse stress plateau during unloading. The deformation along the wire during these two plateaux is non uniform and exhibits a large mechanical hysteresis.

Cold worked wires can be heat treated at lower temperatures (473K to 598K). When submitted to DSC tests to quantify the transformation latent heat, these aged materials show inconclusive results since a weak or no thermal peak is observed (Ahadi and Sun, 2014; Li et al., 2008; Chang et al., 2006; Tsuchiya et al., 2006; Miller and Lagoudas, 2001). Many authors showed that such wires exhibit the superelastic effect, however, without stress plateau and with a smaller mechanical hysteresis when compared to annealed materials (Kan et al., 2016; Tsuchiya et al., 2006; Ahadi and Sun, 2014). Moreover, no deformation localisation phenomenon is observed for these low temperature aged wires.

The knowledge of the amount of latent heat of phase transformation is mandatory in many applications, such as those which use the elastocaloric effect of NiTi alloys in cooling devices (Tušek et al., 2016b; Schmidt et al., 2016). These devices make use of the latent heat of stress induced phase transformation (SIPT) to perform a temperature change in a designed system. Working as heat pumps, a cyclic behaviour of phase transformation is needed to maintain the cooling effect, which in turn, implies in a huge fatigue life. Aged materials present a suitable mechanical behaviour to obtain a longer fatigue life since less strain deformation is obtained in the presence of phase transformation (Qian et al., 2016b). However inconclusive DSC tests are a barrier to determine the transformation latent heat and its further use on the design of elastocaloric applications.

To overcome this problematic, the analysis of the temperature variation during a SIPT can be performed through a thermal approach to obtain the involved heat sources. A method to estimate heat sources from temperature fields obtained with an infrared thermal camera has been presented by Chrysochoos and Louche, 2000. The same method was used to investigate the heat source of phase transformation (Schlosser et al., 2007) and the deformation mechanism (Favier et al., 2007) of NiTi tubes.

In this context, this paper aims to quantify the heat sources generated during a SIPT of a cold worked wire aged at 598K for 30 min. For this purpose, temperature field was acquired using an infrared thermal camera. Strain field was also acquired using a visible camera and analyzed via digital image correlation (DIC). Using a thermodynamic framework based on the Gibbs free energy, the specific latent heat on loading and unloading were determined in function of strain and stress. Also, the martensite fraction was estimated and presented in function of strain and stress. Finally the obtained specific latent heat values were compared with the ones founded in literature for fully annealed NiTi alloys when tested using purely thermal methods (i.e. DSC).

3.2 Material and experimental procedure

3.2.1 Material

The material used in the experimental campaign was a commercial cold worked NiTi wire of d=0.5 mm diameter with a composition of $Ti - 50.9\,at.\%\,Ni$ provided by Fort Wayne Metals. The wire was heat treated (HT) at 598K for 30 min. Figure 3.1a shows the uniaxial tensile test at room temperature ($T_0 = 297\,K$) performed to observe the superelastic behavior until rupture.

Fig. 3.1b shows the result of a Differential Scanning Calorimetry (DSC) performed on the heat treated wire. A Q200 DSC testing machine from TA Instruments was used and the tests were carried out with a temperature rate of 10K/min between 223K and 363K.

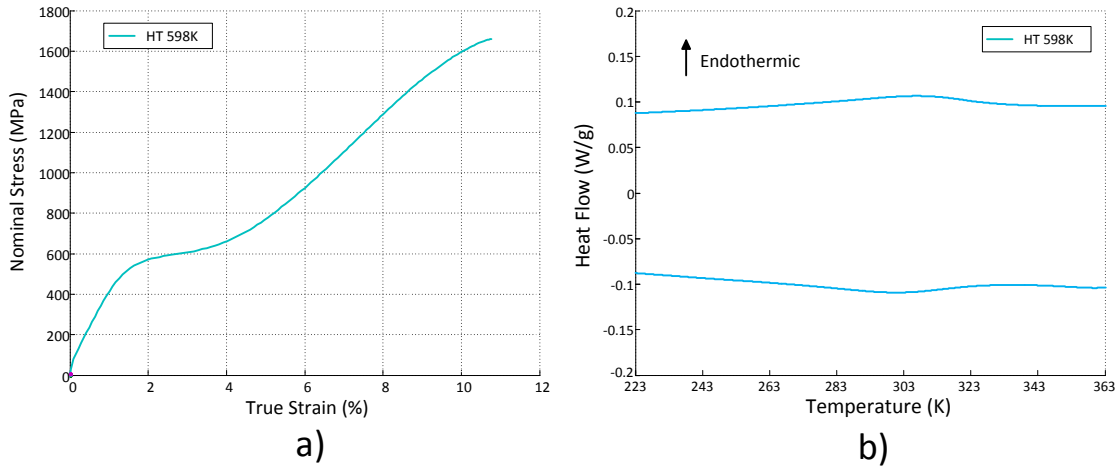

Figure 3.1: *a) Tensile response up to rupture (with global deformation) at room temperature (297 K). b) DSC of the wire heat treated at 598 K (with temperature rate of 10K/min).*

3.2.2 Superelastic tensile tests

The NiTi wire sample was mounted on a standard gripping system on a tensile testing machine (Gabo Qualimeter) equipped with a $500N$ load cell. The gauge length of the sample was $L_0 = 20\,mm$. Before being clamped, the wire was heated in boiling water and then cooled down to room temperature. This procedure was conducted to transform as much as possible the material to the austenite phase, allowing tests to start in the superelastic state.

The tensile test was performed by loading the NiTi wire at a pre-set global strain of 6% at a strain rate of $10^{-2}s^{-1}$. During the complete load-unload cycle, two hold-time were performed, one at the end of loading and the other at the end of unloading, during $50s$ each. Subsequently, the wire was submitted to a tensile test until rupture using the same strain rate.

3.2.3 Thermal and kinematics full field measurements during tensile tests

Temperature field was measured with a fast multi detector infrared camera (FLIR SC6000 series) with a resolution of 640x512 pixels equipped with a medium wavelength infrared (MWIR) macro $1:3.0$ objective lens. Spatial resolution (pixel size) was $16\,\mu m \times 16\,\mu m$. The surface of the wire observed by the IR camera was coated with a highly emissive black paint in order to obtain black body properties compatible with the infrared camera calibration. The thermal field was measured in section of length $l_0 = 8.2mm$, shorter than L_0 (see Fig. 3.2). The number of pixels, in the radial direction of the wire, was 31 in the IR images. The size of the IR zone of interest (ZOI) was then 512x31 pixels.

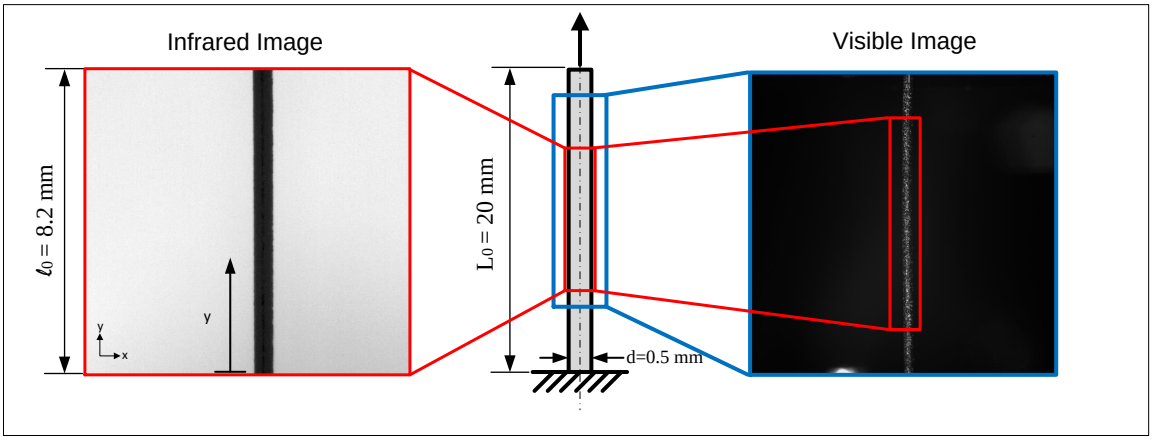

Figure 3.2: *Experimental set-up showing the NiTi wire in the center with extracted thermal and visible images.*

The displacement field was obtained using a visible-light digital camera (ALLIED,

2048x2048 pixels) and Digital Image Correlation "VIC 2D" processing software. The visible camera recorded the opposite side of the IR zone. The wire surface was covered with a random pattern of white paint speckles over a black paint coat to allow displacement and strain field measurements through image correlation. The resolution of the visible light camera ZOI was 2048x72 pixels. However, the ZOI used to perform the DIC analysis was 1181x72 pixels, which corresponded to the same length $l_0 = 8.2mm$ filmed by the thermal camera. At this ZOI a subset of 25 pixels with a step of 17 pixels led to a spatial resolution of $\sim 0.17\,mm$ in the axial direction and $\sim 0.12\,mm$ at the circumferential direction. From that, the strain profiles obtained were calculated taking into account only the axial component ε_{yy} of the true strain (logarithmic) tensor.

In the following, the true strain tensor ε_{yy} will be named ε. The uniform temperature variation computed as the difference between the averaged absolute temperature in the IR ZOI $\langle T \rangle$ and the room temperature T_0 will be named $\langle \theta \rangle$, i.e. $\langle \theta \rangle = \langle T \rangle - T_0$.

From the full field measurements it was possible to obtain the Fig.3.3. The stress vs. strain behavior, on loading, of the superelastic NiTi wire is plotted in Fig. 3.3a. Each square marker represents a strain level in which the strain profiles were plotted in Fig. 3.3b and the temperature variation profiles were plotted in Fig. 3.3c. The curves shown in Fig. 3.3b indicates an uniform strain behavior of the NiTi wire with no Luders-like localization mechanism (Ahadi and Sun, 2014; Leo et al., 1993). This behavior is ratified by the Fig. 3.3c where the temperature variation profiles also present a uniform response over the wire's length. As temperature variation θ and strain ε were considered uniform over the wire's length, their values were averaged in this zone in order to construct their average quantities $\langle \theta \rangle$ and $\langle \varepsilon \rangle$ along the axial length l_0.

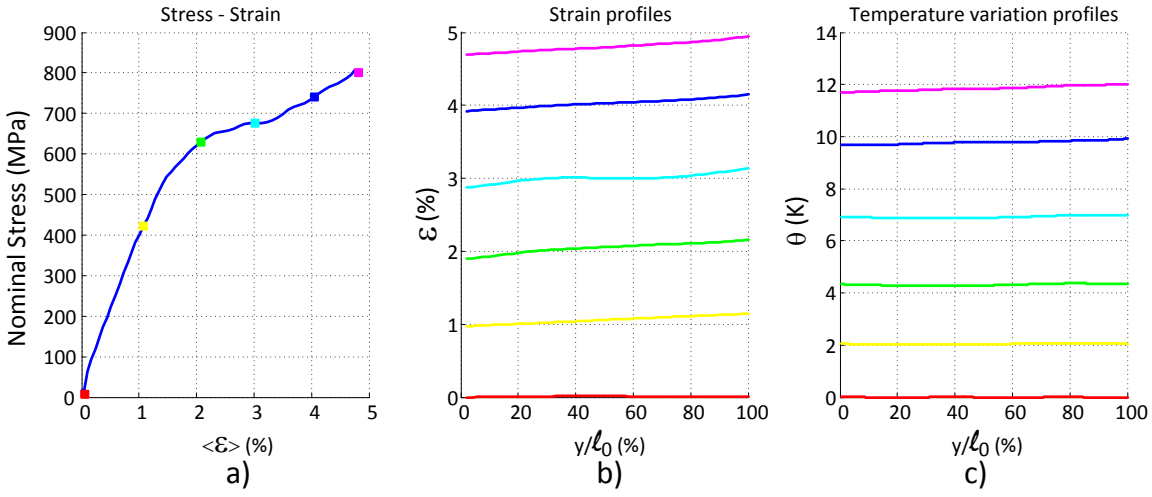

Figure 3.3: *a) Single tensile Stress-Strain curve during loading and unloading of the NiTi wire, where $\langle \varepsilon \rangle$ is the averaged logarithmic strain over the length l_0. b) DIC average logarithmic strain profiles over the wire's gauge length at different strain levels, as indicated by the colored marks in (a). c) Temperature variation profiles at different strain levels.*

3.2.4 Heat sources and thermal energy estimation

In the present work, due to the uniform temperature variation along the tested wire, a time dependent thermal approach was chosen. The thermal framework used to estimate heat sources during a superelastic tensile test is presented hereafter.

For a simple geometry (wire) and uniformly distributed heat sources (uniform temperature distribution), if the specimen is not too far from thermal equilibrium with the ambient medium T_0, the thermal model reads (Chrysochoos et al., 1996; Chrysochoos and Louche, 2000; Schlosser, 2008):

$$c\left(\frac{\partial\langle\theta\rangle}{\partial t}+\frac{\langle\theta\rangle}{\tau_{eq}}\right)=\langle\dot{q}\rangle \tag{3.1}$$

where $\langle\dot{q}\rangle$ represents the uniform heat sources or thermal power per unit of mass.

As shown by Chrysochoos et al., 1996; Chrysochoos and Louche, 2000, the heat source in the right member of Eq.3.1 can be calculated from experimental data. It is obtained from estimations of the two terms of the left member after some filtering and numerical derivative operations.

In the following and in order to simplify the notation, the uniform heat sources will be noted $\dot{q}$. The specific heat c is assumed to be uniform and constant. The parameter τ_{eq} represents a characteristic time of the heat losses by both convection and radiation through the specimen surface and by conduction towards the grip's zone.

Thermal energy E_{th} can also be estimated. It is calculated through time integration of the heat sources per unit of mass $\dot{q}$; as shown in Eq. 3.2.

$$E_{th}(t)=\int_0^t \dot{q}dt \tag{3.2}$$

3.2.5 Determination of mechanical power and energy

Mechanical power P_{mech} as well as the mechanical energy E_{mech} were calculated. Both values are determined per unit of mass. The first one is defined as:

$$P_{mech}=\frac{\sigma\dot{\varepsilon}}{\rho} \tag{3.3}$$

where σ is the uniaxial tensile true stress, $\dot{\varepsilon}$ the uniaxial strain rate and ρ the mass density. True stress σ is calculated from the formula $\sigma=\sigma_0(1+\varepsilon_n)$ where σ_0 is the engineering stress and ε_n is the nominal strain (Quan et al., 2012).

The mechanical energy per unit of mass E_{mech} was calculated by time integrating the mechanical power, as described in the following:

$$E_{mech}(t) = \int_0^t P_{mech} dt \tag{3.4}$$

3.3 Results

3.3.1 Strain and temperature field evolution

Figure 3.4 shows nominal stress vs. true strain $\sigma_0 - \langle\varepsilon\rangle$ curve of the uniaxial tensile test (Fig. 3.4a) and the temporal evolution of the uniform temperature variation $\langle\theta\rangle$ and strain $\langle\varepsilon\rangle$ (Fig. 3.4b). The uniform strain rate temporal evolution $\langle\dot{\varepsilon}\rangle$ is also plotted in Fig. 3.4b. It was calculated by numerical derivation of the strain temporal evolution.

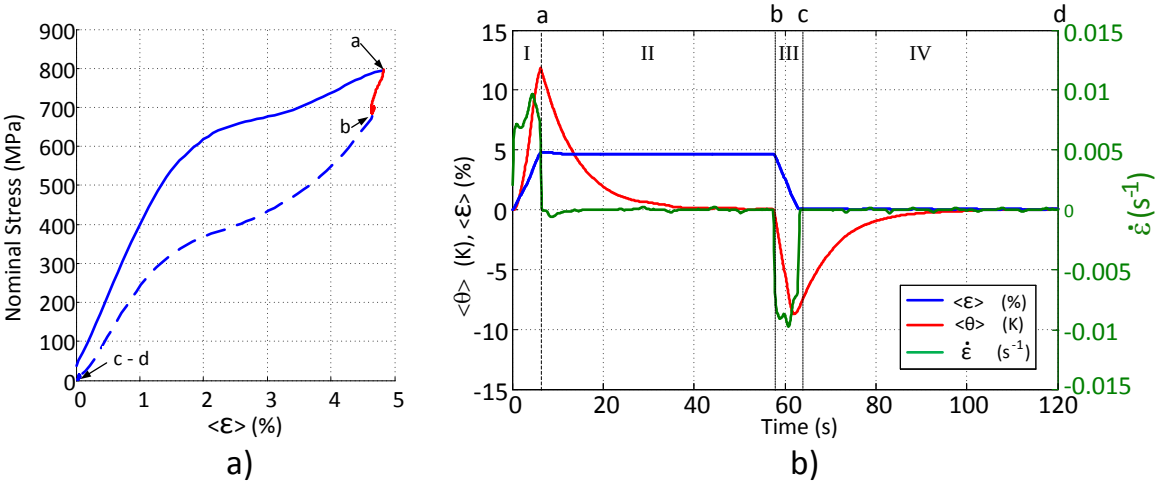

Figure 3.4: *a) Stress-strain curve for a single cycle tensile test at* $\langle\dot{\varepsilon}\rangle = 10^{-2}s^{-1}$. *b) Average temperature variation* $\langle\theta\rangle$ *, average strain and average strain rate in function of time.*

Four distinct stages, noted I$(0-a)$, II$(a-b)$, III$(b-c)$ and IV$(c-d)$, are outlined:

- Stage I: Temperature raises as the strain goes up to 4.8%. Due to the fast release of the latent heat of phase transformation the temperature increase was $\theta = 11.8K$.
- Stage II: The hold time allows the temperature to decrease to T_0 while $\langle\dot{\varepsilon}\rangle = 0$ and $\langle\varepsilon\rangle$ remained almost constant.

- Stage III: The recovering of strain promoted the absorption of latent heat due to reverse transformation, leading to a negative temperature variation of $\langle\theta\rangle = -8.7K$. It can be noticed that at the end of the stage III (end of unloading) the temperature started to rise again just before the strain reaches zero.

- Stage IV: Second hold time allowing once again the temperature to increase to T_0 while $\langle\dot{\varepsilon}\rangle = 0$ and $\langle\varepsilon\rangle$ remained constant.

3.3.2 Estimation of thermal power

The averaged thermal power $\dot{q}$ was calculated using the averaged temperature $\langle\theta\rangle$ shown in Fig. 3.4b and a processing of Eq. 3.1. The material properties used were $\rho = 6500\,Kgm^{-3}$ and $c = 500\,JKg^{-1}K^{-1}$.

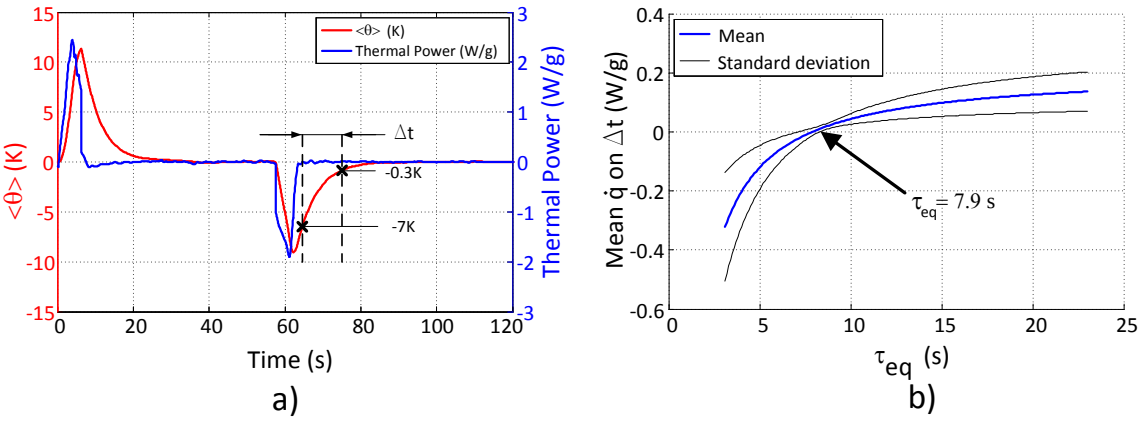

Figure 3.5: *a) Uniform temperature variation $\langle\theta\rangle$ and Thermal power $\dot{q}$, presented on left and right axis, respectively, in function of time. b) Mean and standard deviation of $\dot{q}$, calculated in the time interval Δt shown in a), obtained for different values of τ_{eq}.*

Figure 3.5a shows the temperature variation $\langle\theta\rangle$ and an example of the temporal evolution of the thermal power ($\dot{q}$) computed with a value of $\tau_{eq} = 5s$.

The best value of τ_{eq} was calculated on the hold-time of stage IV. During this stage no heat source was present. From Eq. 3.1 and for each imposed τ_{eq} value, the $\dot{q}$ quantity was computed on the period Δt, with its statistical characteristic (mean and standard deviation). In Figure 3.5b the blue thick line represents the mean value of Thermal Power in function of τ_{eq}, while the black lines show the standard deviation. With this procedure, it was possible to determine a value of $\tau_{eq} = 7.9\,s$, considered as the optimal value leading to a thermal power close to zero.

3.3.3 Thermal and mechanical power and energy in function of time

Figure 3.6 shows the Thermal power and the Mechanical power per unit of mass (W/g) as function of time.

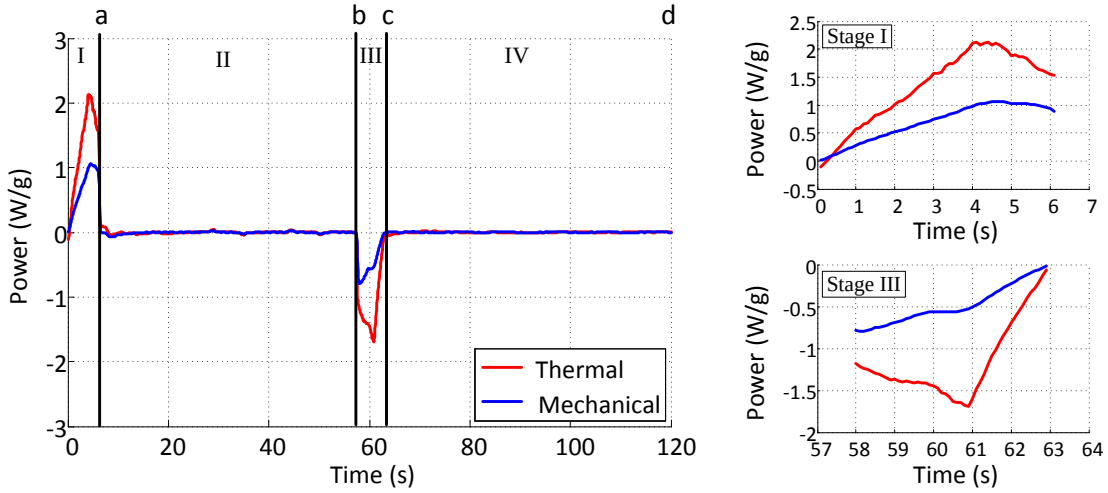

Figure 3.6: *Thermal and mechanical powers per unit of mass in function of time for a single loop tensile test at* $\dot{\varepsilon} = 10^{-2}s^{-1}$. *At right, close-up for stages* I *and* III.

Similarly to Fig. 3.4b, it is possible to divide Fig. 3.6 in four distinct stages. In stage I, one can observe the sudden increase of thermal power and its continuous growth until it reaches a peak at approximately $\dot{q} = 2.1\,W/g$. The same qualitative behavior is shown by the mechanical power, which reaches at the same time a maximum at $P_{mech} = 1.0\,W/g$. After the thermal peak in the stage I, the decrease on thermal power highlights the decrease of the phase transformation "activity" before reaching the end of loading. Stage II, as well as the stage IV, which corresponds to the hold-times of Fig. 3.4b, are characterized by zero thermal power. Finally, in stage III (unloading) one can see the reversible thermomechanical behavior of the martensite transformation. The thermal power shows the same qualitative response compared to the stage I (loading) but with a peak at $\dot{q} = -1.7\,W/g$ which, despite its lower amplitude, is around twice as large as the mechanical power, which reaches $P_{mech} = -0.8\,W/g$.

Figure 3.7 shows the thermal E_{th} and mechanical E_{mech} energies per unit of mass (J/g) as a function of time. These results were calculated through Eqs. 3.2 and 3.4 using data shown in Fig. 3.6. On loading (stage I), one can observe that the monotonic increase of thermal and mechanical energies reaching a maximum of $E_{th} = 8.3\,J/g$ and $E_{mech} = 4.3\,J/g$ respectively. During the first hold-time (stage II) a little drop on energy level can be observed at the beginning for both thermal and mechanical energies. This behavior is associated with a stress decrease due to the specimen cooling and can be explained by the Clausius-Clapeyron relation. This relation states that the transformation stress variation is directly proportional to the temperature variation. After that, the energies show a constant trend once no power is generated in this stage.

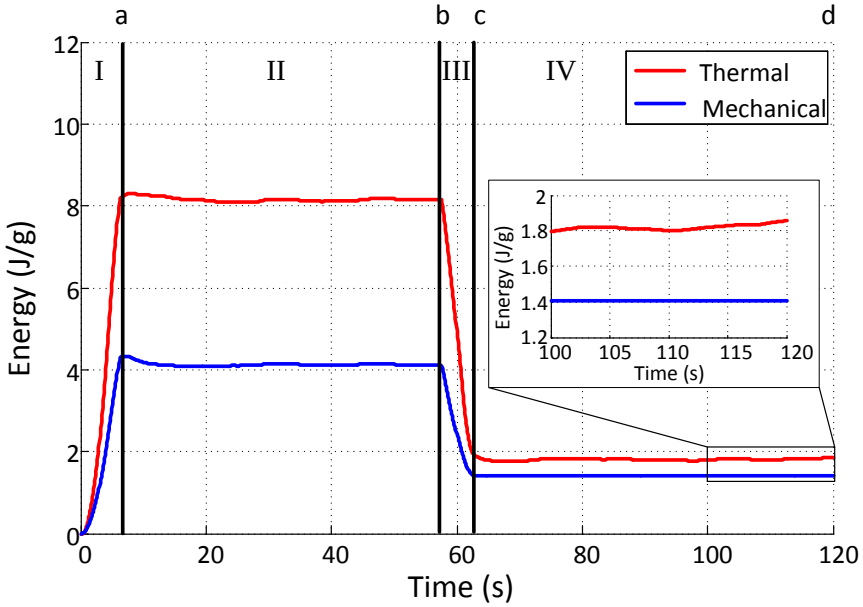

Figure 3.7: *Thermal and mechanical energies in function of time for a single loop tensile test.*

During unloading, a decrease of thermal and mechanical energies can be observed. This response is due to the endothermic reverse transformation and to the total strain recovery. Regarding the mechanical energy, a value of $E_{mech} = 1.4J/g$ is observed at the end of stage III. This residual value represents the hysteresis loop area on the stress-strain curve. In the same way, the thermal energy shows a close value ($E_{th} = 1.8J/g$) at the end of the cycle. This behavior leads to the conclusion that one has the condition of a thermodynamic cycle where $\oint P_{mech} = \oint \dot{q}$.

3.3.4 Thermal and mechanical power and energy as function of strain and stress

3.3.4.1 Cyclic test

Powers

Figure 3.8 shows, as a function of true strain ($\langle\varepsilon\rangle$), the thermal ($\dot{q}$) and mechanical ($P_{mech}$) power per unit of mass (on the left ordinate axis) and strain rate ($\dot{\varepsilon}$) (on the right ordinate axis). The dots represent the loading and the empty circles represent the unloading.

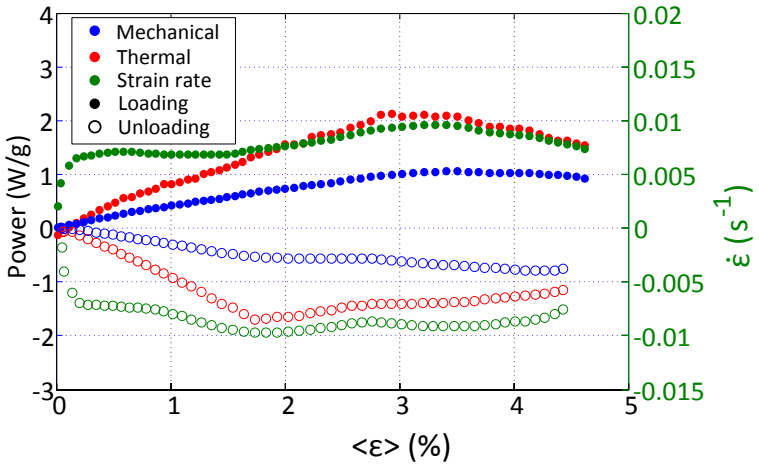

Figure 3.8: *Evolution with the strain of the thermal and mechanical power per unit of mass (left ordinate axis) and strain rate (right ordinate axis), on loading (dots) and unloading (empty circles).*

Since the beginning of loading, one can notice the increasing behavior of thermal power. Also, a non-zero value of thermal power at such low strain level confirms the presence of an early beginning of phase transformation. The increasing behavior stopped at approximately 3% strain, where it reached its maximum value. Beyond this point, a slight decreasing on thermal power is observed until the end of unloading. This response suggests a decrease of the thermal activity, possibly due to the decrease of phase transformation rate. The same trend of evolution is observed on the mechanical power. In the same way, since the beginning of unloading, thermal power started to decrease. It reached its minimum value at about 1.7% strain. Mechanical power, however, showed a monotonically decreasing response from its minimum, starting at 4.5%, until reach zero. The recoverable nature of this phenomenon is qualitative revealed as an almost symmetric load-unload path shown by the dots and empty circles.

Due to the non-constant strain rate during the test, the thermal and mechanical power were normalized by the strain rate. With that, the misleading interpretations due to the strain rate effect can be excluded.

The normalized powers were plotted in Figs. 3.9a and 3.9b in function of strain and stress, respectively. Observing the normalized thermal power in Fig. 3.9a, one can notice the same qualitative response presented in Fig. 3.8. From that, one can still claim the strong presence of phase transformation from 0 to 3% strain and its decrease from 3% strain until the end of loading.

Analogously, in Fig. 3.9b the thermal power peak takes place around 700 MPa on loading, which is approximately the end of superelastic plateau observed in Fig. 3.4a. During unloading, the thermal peak appears at approximately 350 MPa, which is the end of the unloading plateau at the stress-strain curve shown in Fig. 3.4a. Such response highlights the thermal coupling present on SIPT.

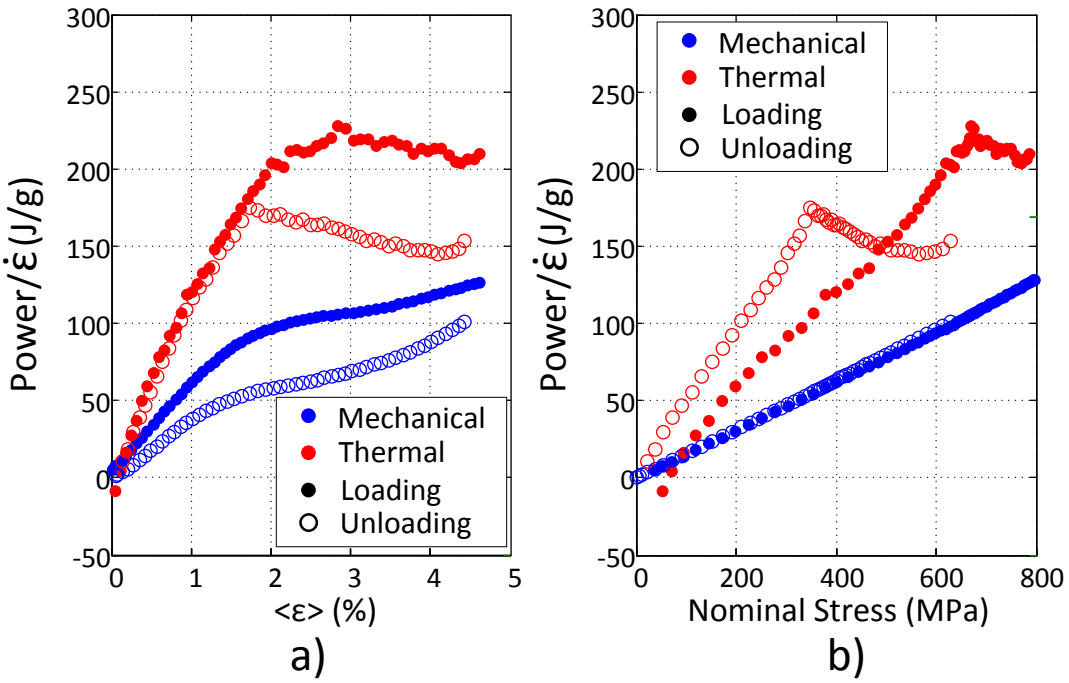

Figure 3.9: *a) Thermal and Mechanical Power normalized by strain rate in function of true strain. b) Same values in function of nominal stress.*

Energies

Figure 3.10 shows thermal and mechanical energies per unit of mass (J/g) as a function of (a) strain (%) and (b) stress (MPa). In Fig. 3.10a, mechanical energy increased monotonically until 4.3 J/g at the end of loading and decreased continuously to 1.4 J/g at the end of unloading. Thermal energy also showed the same qualitative response, although it reached 8.3 J/g at the end of loading, about twice the magnitude of the mechanical energy. During unloading, thermal energy decreased, reaching a minimum of 1.8 J/g, around the same mechanical energy level.

In Fig. 3.10b at loading, thermal energy increased to 2 J/g in the range of 0 to 600 MPa. With further loading, from 600 MPa to 800 MPa, it increased from 2 J/g to 8.3 J/g. The same qualitative behavior was observed for the mechanical energy where the most part of energy was released during the transformation plateau.

3.3.4.2 Rupture test

Figure 3.11 shows the normalized powers (a) and energies (b) in function of true strain for the tensile test until rupture. In Fig. 3.11a one can observe the same qualitative response shown by the cyclic tensile test at Fig. 3.9a. The increasing monotonic thermal response reaching a maximum at approximately 3% strain is observed. Also, after 3% strain,

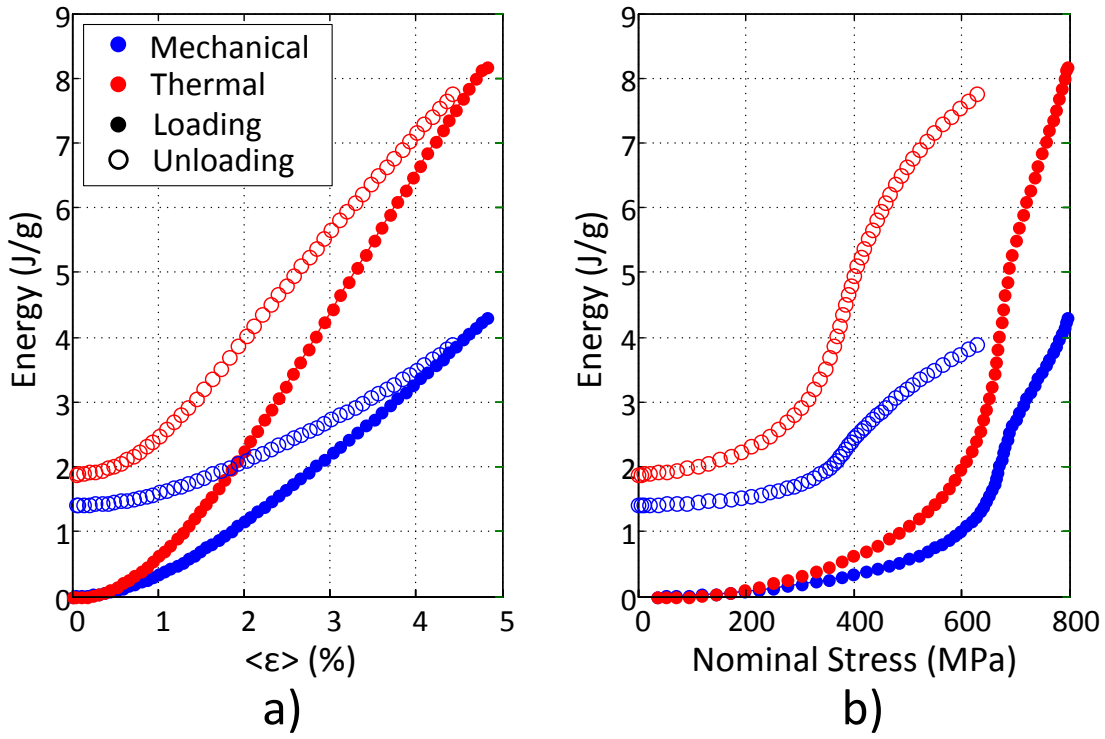

Figure 3.10: *a) Thermal and Mechanical Energies in function of true strain. b) Same values in function of nominal stress.*

the decreasing response of the normalized thermal power followed the same behavior presented at Fig. 3.9a. In Fig. 3.11a, the decreasing behavior can be observed until approximately 10% strain. After that, a slight increase on the normalized thermal power is observed before the rupture. This behavior may be explained by a decrease of the thermal power generated by phase transformation and its increase due to the presence of plastic deformation. In this case, one may conclude that the mechanism of plastic deformation takes place around 10% strain.

Figure 3.11b also shows the same qualitative behavior of the thermal and mechanical energies shown at Fig. 3.10a. A maximum of 19.3 J/g is reached by thermal energy while the mechanical one showed 15.3 J/g at the end of test. However, due to the presence of plastic transformation the amount of energies obtained cannot be associated only with the phase transformation.

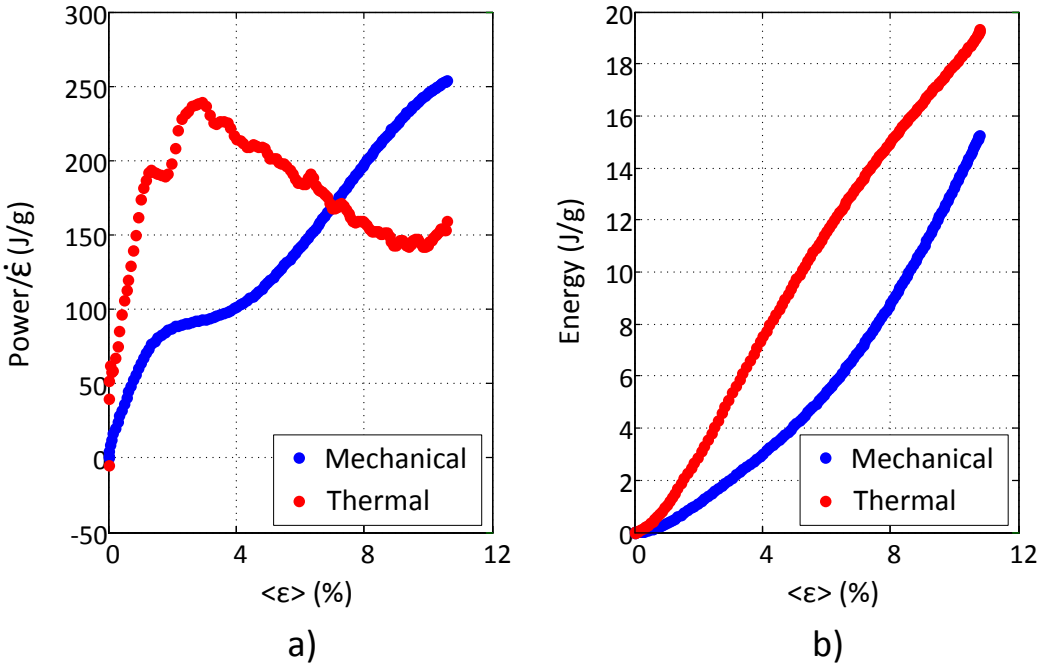

Figure 3.11: *a) Thermal and Mechanical Power normalized by strain rate in function of true strain. b) Thermal and Mechanical Energy in function of true strain.*

3.4 Discussion

3.4.1 Deformation mechanisms in SMA

It is well known that deformation mechanisms for NiTi include elastic strain of the atomic lattice associated with martensitic transformation (Šittner et al., 2006). Also, plastic deformation may be involved but is effective only for large strains (Brinson et al., 2004). In this way, the classical additive decomposition of the total strain rate ($\dot{\varepsilon}$) is assumed as:

$$\dot{\varepsilon} = \dot{\varepsilon}_{el} + \dot{\varepsilon}_{in} = \dot{\varepsilon}_{el} + \dot{\varepsilon}_{tr} + \dot{\varepsilon}_{pl} \tag{3.5}$$

where the $\dot{\varepsilon}_{el} = \dot{\sigma}/E$ and $\dot{\varepsilon}_{in}$ are the elastic and inelastic strain rates, respectively, and E is the Young modulus. The inelastic strain rate ($\dot{\varepsilon}_{in}$) includes the strain rate due to phase transformation ($\dot{\varepsilon}_{tr}$) and the one due to plasticity ($\dot{\varepsilon}_{pl}$).

In this work, the value of the elastic modulus E=70 GPa is used. This value accounts for the austenite phase and it was determined through three different experimental methods (tensile tests, in situ synchrotron x-ray diffraction, and dynamic mechanical analysis) and estimated via theoretical calculation from elastic constants by Šittner et al., 2014.

Analogously, the thermal power is also decomposed as shown in Eq. 3.6:

$$\dot{q} = \dot{q}_{thel} + \dot{q}_{in} = \dot{q}_{thel} + \dot{q}_{tr} + \dot{q}_{pl} \tag{3.6}$$

where the thermoelastic heat source $\dot{q}_{thel} = -(\alpha T/\rho)\dot{\sigma}$ is calculated with α as the coefficient of thermal expansion ($\alpha = 1.1 \times 10^{-5} K^{-1}$), T the test temperature, ρ the mass density and the true stress rate $\dot{\sigma} = d\sigma/dt$; $\dot{q}_{tr}$ is the heat source associated with the phase transformation and $\dot{q}_{pl}$ is the part of the intrinsic dissipated power due to plasticity.

The mechanical power per unit of mass can also be decomposed as shown in Eq. 3.7:

$$P_{mech} = P_{mech-el} + P_{mech-in} \tag{3.7}$$

Where the elastic and inelastic mechanical power per unit of mass are: $P_{mech-el} = \frac{1}{\rho}\sigma\dot{\varepsilon}_{el}$ and $P_{mech-in} = \frac{1}{\rho}\sigma\dot{\varepsilon}_{in}$, respectively.

Furthermore, thermal and mechanical energies are also decomposed in elastic and inelastic portions, as described before. They are calculated through time integration of each portion of correspondent powers.

3.4.2 Impact of thermoelasticity on thermal Power and Energy

Figure 3.12a shows, in function of strain, on the left ordinate axis, thermal power normalized by the strain rate ($\dot{q}/\dot{\varepsilon}$) and the inelastic thermal power ($\dot{q}_{in}/\dot{\varepsilon}$) also normalized by strain rate. The evolution of the ratio between inelastic thermal power and mechanical power ($\dot{q}_{in}/P_{mech-in}$) in function of strain is also plotted in Fig. 3.12a. The same values are plotted in Fig. 3.12b in function of stress.

One can observe that the normalized inelastic thermal power ($\dot{q}_{in}/\dot{\varepsilon}$) is slightly higher than the thermal one ($\dot{q}/\dot{\varepsilon}$). This difference is more evident at the beginning of loading between $0 - 2\%$, at Fig. 3.12a, and 0-600 MPa, at Fig. 3.12b. These ranges represent the elastic portion on the superelastic loop. In this range, it is possible to observe that thermal power attains negative values at the beginning of loading. Such a response puts in evidence the endothermic nature of thermoelasticity during loading. Thereafter, once the phase transformation shows a stronger effect, between $2 - 4.8\%$ (Fig. 3.12a) and 600-800MPa (Fig. 3.12b) the thermoelasticity effect is less pronounced.

Also, observing the Fig. 3.12, the ratio between inelastic thermal and mechanical powers ($\dot{q}_{in}/P_{mech-in}$) immediately increases to a value close to 6 but shows a decreasing trend until reach a value around 2. During unloading, this ratio increased monotonically from a value around 2 and reaches a ratio of 7 at the end of unloading. Such a high ratio value implies a significant thermal effect in relation to the mechanical power. This ratio commonly reported on literature as the Taylor and Quinney coefficient, is usually less than 1 for plastic deformation of metals or polymers (Zaera et al., 2013; Zaera et al., 2012;

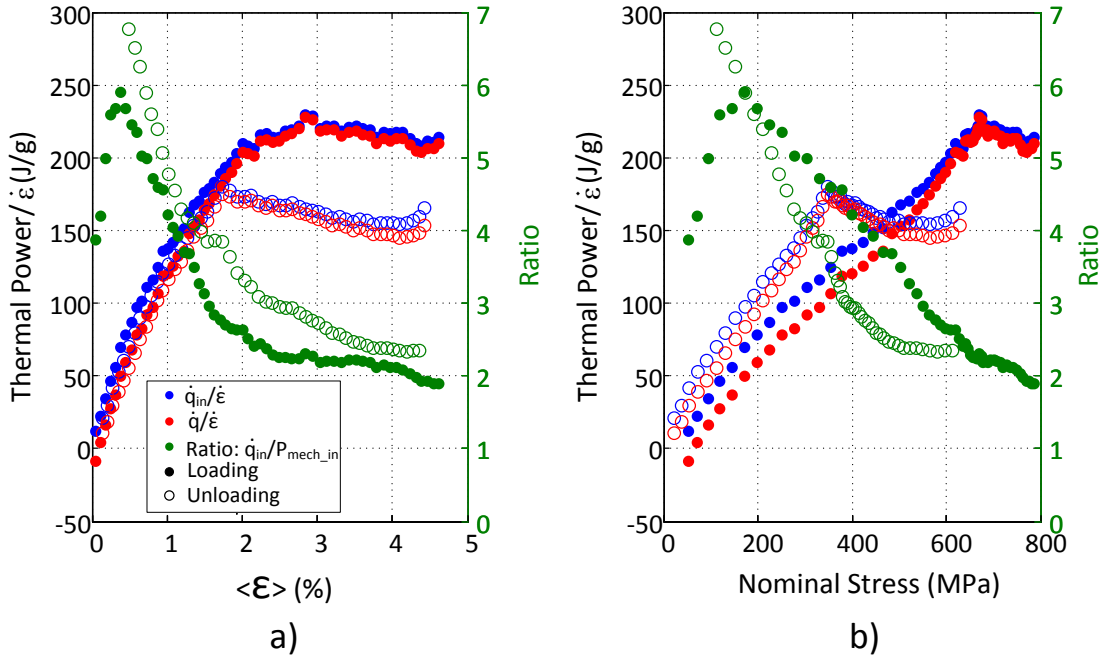

Figure 3.12: *a) Normalized inelastic thermal power ($\dot{q}_{in}/\dot{\varepsilon}$) and normalized thermal power ($\dot{q}/\dot{\varepsilon}$) on the left ordinate axis. Ratio between inelastic thermal power ($\dot{q}_{in}$) and inelastic mechanical power on right ordinate axis ($\dot{q}_{in}/P_{mech-in}$) in function of true strain. b) Same values in function of nominal stress.*

Rittel, 1999). A thermal and mechanical power ratio greater than 1 can be explained by a deformation mechanism different than plasticity, here due to phase transformation.

Figure 3.13a shows, on the left ordinate axis, the thermal energy (E_{th}) and the inelastic thermal energy (E_{in}). The thermal energy was calculated using Eq. 3.2 and data shown in Fig. 3.6. The evolution of the ratio between inelastic thermal energy and mechanical energy ($E_{in}/E_{mech-in}$) as function of strain is also plotted in Fig. 3.13a. The same values are plotted in Fig. 3.13b as function of stress.

In Fig. 3.13 it is possible to observe a slight difference between thermal energy (E_{th}) and the inelastic thermal energy (E_{in}). It is more evident at the end of loading. This difference is explained by the thermoelasticity occurring on the beginning of the loading. However, no difference is observed at the end of unloading. Such behavior highlights the reversibility of the thermoelastic effect on the tensile test.

It is also possible to observe the ratio between inelastic thermal energy and inelastic mechanical energy in Fig. 3.13. During loading, a sudden rise from 0 to a value around 6 is observed; after that, a decreasing tendency to a ratio of 2.5 is observed. Similarly, Peyroux et al., 1998b and Balandraud et al., 2005, studying the ratio between thermal and mechanical energy, reported a value of 10 but for a CuZnAl SMA.

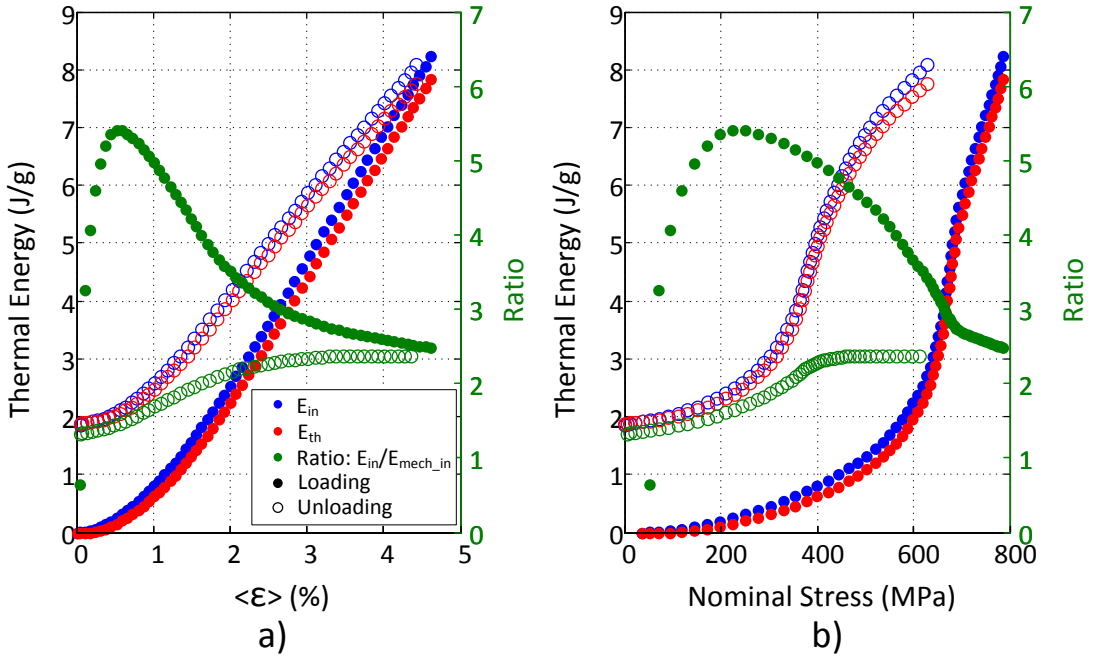

Figure 3.13: *a) Thermal energy (E_{th}) and the inelastic thermal energy (E_{in}) on left ordinate axis and Energy ratio ($E_{in}/E_{mech-in}$) on the right ordinate axis in function of true strain. b) Same values in function of nominal stress.*

3.4.3 Thermodynamics of martensitic transformation

3.4.3.1 Thermodynamic framework

Several thermodynamic framework have been proposed to describe the thermomechanical behavior of shape memory alloys. Among them, the one used in this work is based on the work developed by Ortin and Planes and Wollants et al. (Ortín and Planes, 1988; Ortín and Planes, 1989; Ortín and Planes, 1991; Wollants et al., 1993). It expresses the martensitic transformation as a diffusionless first order reversible transformation at the scale of an elementary volume. Following this approach, the occurrence of a thermoelastic martensitic transformation is determined by the Gibbs free energy (G) balance at equilibrium for the transformation, which is given by the condition $dG = 0$. For a thermoelastic martensitic transformation in a polycrystalline matrix, the free energy per unit mass changes over an infinitesimal step of martensite fraction df_m of transformation and is expressed as shown in (Ortín and Planes, 1989; Wollants et al., 1993):

$$dG = (\Delta H_c - T\Delta S_c)df_m + \partial E_{st} + \partial E_{fr} - W^{tr}_{mech} = 0 \tag{3.8}$$

where:

- $dG = (\partial G/\partial f_m)df_m = G'df_m$;
- ΔH_c is the difference between the specific enthalpies of the martensite and austenite phase;
- ΔS_c is the difference between the specific entropies of the martensite and austenite phase;
- f_m is the mass fraction of martensite defined in the elementary volume; depending only of time. Its time derivate $\frac{\mathrm{d}f_m}{\mathrm{d}t}$ is noted $\dot{f}_m$.
- T is the temperature;
- $\partial E_{st} = (\partial E_{st}/\partial f_m)df_m = E'_{st}(f_m)df_m$ is the stored energy in the elementary volume transformed by an infinitesimal step df_m;
- $\partial E_{fr} = (\partial E_{fr}/\partial f_m)df_m = E'_{fr}(f_m)df_m$ is the friction energy dissipated by the infinitesimal step df_m;
- $\partial W^{tr}_{mech} = (\partial W_{mech}/\partial f_m)df_m = W'_{mech}(f_m)df_m$ is the external mechanical work per unit mass of the elementary volume during the infinitesimal step df_m.

All terms in Eq. 3.8 are algebraic values and they are expressed as energy per unit of mass in Jg^{-1}, where, at full austenite phase $f_m = 0$ and at full martensite phase $f_m = 1$. The infinitesimal martensite mass fraction step (df_m) is positive during the forward transformation and negative during the reverse transformation. The term ∂E_{fr} is the sum of all irreversible energies dissipated, such as the energy consumed in moving dislocations and interfaces. The term ∂E_{fr} is always dissipated, thus is always positive. Rewriting then Eq. 3.8, one has:

$$\Delta H_c - T\Delta S_c + E'_{st} + E'_{fr} - W'_{mech} = 0 \tag{3.9}$$

3.4.3.2 Transformation heat source

The transformation heat source $\dot{q}_{tr}$ is defined as:

$$\dot{q}_{tr} = \dot{q}_{tr-chem} + \dot{q}_{tr-diss} = \Delta H_{tr}(f_m)\dot{f}_m \tag{3.10}$$

where ΔH_{tr} is the specific latent heat and $\dot{q}_{tr}$ is the specific transformation heat sources including both chemical $\dot{q}_{tr-chem}$ and dissipative $\dot{q}_{tr-diss}$ components.

From Eqs. 3.8 and 3.10, ΔH_{tr} can be written as:

$$\Delta H_{tr} = -T\Delta S_c + E'_{fr} \tag{3.11}$$

or

$$\Delta H_{tr} = -\Delta H_c - E'_{st} + W'_{mech} \tag{3.12}$$

3.4.3.3 Forward and reverse specific latent heat

Observing the Eqs. 3.11 and 3.12 in a cyclic loading analysis one has:

- On loading $(A - M)$, with the change of $f_m = 0$ to $f_m \leq 1$:

$$\Delta H_{tr}^{A-M} = -T^{A-M}\Delta S_c + E'^{A-M}_{fr} \tag{3.13}$$

  and

$$\Delta H_{tr}^{A-M} = -\Delta H_c - E'^{A-M}_{st} + W'^{A-M}_{mech} \tag{3.14}$$

- On unloading $(M - A)$, with the change of $f_m \leq 1$ to $f_m = 0$:

$$\Delta H_{tr}^{M-A} = -T^{M-A}\Delta S_c + E'^{M-A}_{fr} \tag{3.15}$$

  and

$$\Delta H_{tr}^{M-A} = -\Delta H_c - E'^{M-A}_{st} + W'^{M-A}_{mech} \tag{3.16}$$

with

- $\Delta S_c < 0$;
- $\Delta H_c < 0$;
- $E'^{A-M}_{fr} > 0$ and $E'^{M-A}_{fr} < 0$;
- $E'^{A-M}_{st} > 0$ and $E'^{M-A}_{st} > 0$;
- $W'^{A-M}_{mech} > 0$ and $W'^{M-A}_{mech} > 0$.

Combining then, the Eqs. 3.13 and 3.15, one has:

$$\Delta H_{tr}^{A-M} - \Delta H_{tr}^{M-A} = -(T^{A-M} - T^{M-A})\Delta S_c + (E'^{A-M}_{fr} - E'^{M-A}_{fr}) \tag{3.17}$$

With the terms $E'^{A-M}_{fr} > 0$ and $E'^{M-A}_{fr} < 0$, the second term on the right hand side of the Eq. 3.17 will be always positive. Also, as the component ΔS_c is a negative constant the first term of the right hand side will also be positive. However, its magnitude is strongly dependent on the temperature variation.

In the other hand, combining the Eqs. 3.14 and 3.16, one has:

$$\Delta H^{A-M}_{tr} - \Delta H^{M-A}_{tr} = -(E'^{A-M}_{st} - E'^{M-A}_{st}) + (W'^{A-M}_{mech} - W'^{M-A}_{mech}) \tag{3.18}$$

The difference of the stored energy between loading and unloading ($E'^{A-M}_{st} - E'^{M-A}_{st}$) is very often assumed as zero since the stored energy is considered reversible. From that, the difference of specific latent heat between loading (ΔH^{A-M}_{tr}) and unloading (ΔH^{M-A}_{tr}) can be written as a difference of the mechanical work. Then, Eq. 3.18 is written as:

$$\Delta H^{A-M}_{tr} - \Delta H^{M-A}_{tr} = W'^{A-M}_{mech} - W'^{M-A}_{mech} \tag{3.19}$$

3.5 Characterisation of the martensitic transformation

3.5.1 Determination of transformation strain ($\Delta\varepsilon_{tr}$)

To determine the transformation strain $\Delta\varepsilon_{tr}$ several superelastic tensile tests were carried out at different strain levels between 7% and 11% of superelastic deformation. The tests were performed on a *Gabo Qualimeter* testing machine with displacement control and crosshead speed of $10^{-5}s^{-1}$. The tests consisted in loading the wire (at room temperature) until a preset deformation level ε_a and unloading until zero stress, then heating the wire at 373K.

Figure 3.14a shows an example of the experimental superelastic loop in which it is possible to observe the decomposition of the strain. At the end of loading, the total strain ε_a can be described as being composed by an elastic strain ε^{el}_a, a plastic strain ε^{pl}_a and a transformation strain ε^{tr}_a. After unloading, a final strain ε_b is achieved. Heating above the critical phase transformation temperature allows the material to recover a part of this deformation and reach the final strain level ε_c.

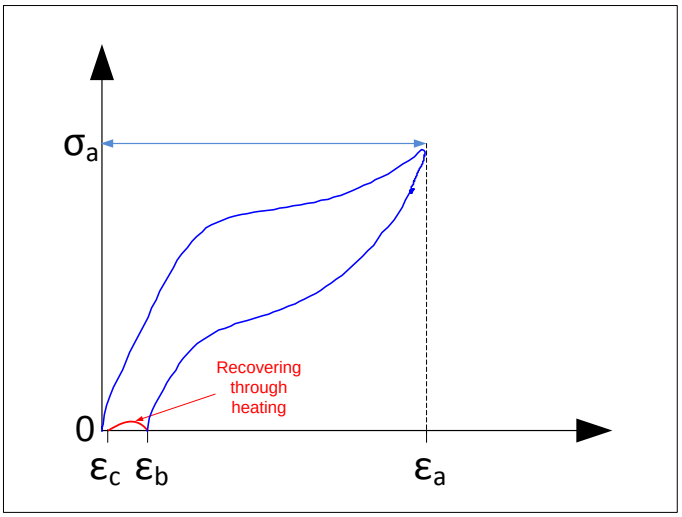

Figure 3.14: *a) Classic superelastic loop of a SMA with the decomposition of the strain components.*

The strain ε_a is written as:

$$\varepsilon_a = \varepsilon_a^{el} + \varepsilon_a^{pl} + \varepsilon_a^{tr} \tag{3.20}$$

with $\varepsilon_a^{el} = \sigma_a / E$.

Assuming $\varepsilon_a^{pl} = \varepsilon_c$, one can rewrite Eq.3.20 as:

$$\varepsilon_a^{tr} = \varepsilon_a - \varepsilon_c - \frac{\sigma_a}{E} \tag{3.21}$$

All the values in the right hand side of the Eq. 3.21 can be measured experimentally.

Technically, the transformation strain ε_a^{tr} increases with increasing ε_a until a maximum noted $\Delta\varepsilon_{tr}$, when the phase transformation is completed, i.e. the martensite fraction is $f_m = 1$. The evolution of ε_a^{tr} with ε_{in} is assumed to follow a curve similar to Fig. 3.15a.

Figure 3.15b shows the experimental results of the tests carried out using the before mentioned method. In the present study, the tested wires reached rupture before the theoretical asymptotic point. Therefore, the maximum value shown by the data presented in Fig. 3.15b was assumed as being lower than the true transformation strain $\Delta\varepsilon_{tr}$. With this, the value of transformation strain was assumed as being $\Delta\varepsilon_{tr} > 8\%$.

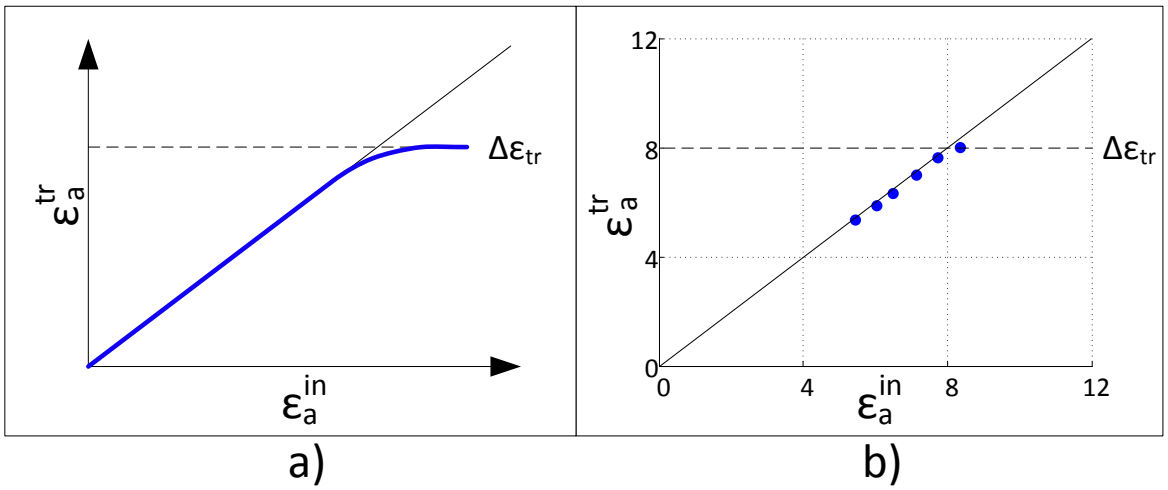

Figure 3.15: *a) Theoretical evolution of ε_a^{tr} with the total inelastic strain ε_{in}. b) Experimental data used to determine the value of transformation strain $\Delta\varepsilon_{tr}$.*

Figure 3.16 shows an inverse pole figure describing the orientation dependence of the transformation strain $\Delta\varepsilon_{tr}$ in a NiTi single crystal (Miyazaki et al., 1984). One can observe that in the direction (011), same preferential direction of the used cold worked wire (see Chapter 2), the $\Delta\varepsilon_{tr}$ is between 8% and 9%. Also, in a work published by Orgéas and Favier, 1998, they observed that the $\Delta\varepsilon_{tr}$ of a $A - M$ transformation was around $\varepsilon_{tr} = 8\%$. Finally, based on the experimental determination and the literature support, the value $\Delta\varepsilon_{tr} = 8\%$ is used in the following of this study.

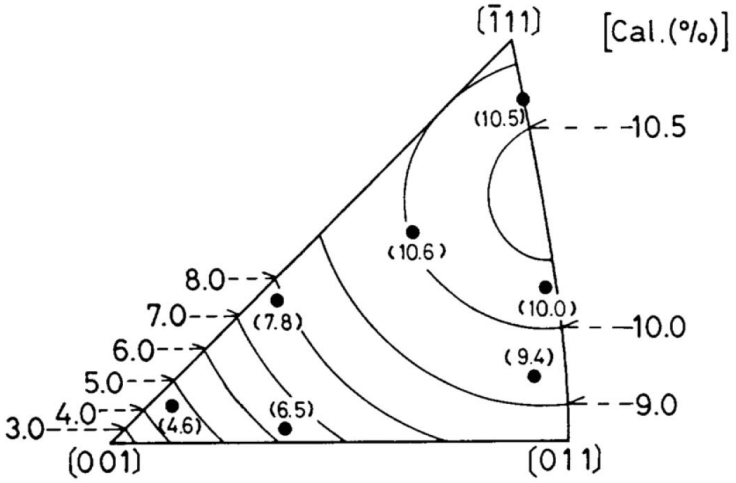

Figure 3.16: *Inverse pole figure showing the orientation dependence of the transformation strain $\Delta\varepsilon_{tr}$ of solution-treated NiTi single crystals (parenthesis) and calculated values (contour lines)(Adapted from Miyazaki et al., 1984).*

3.5.2 Experimental determination of forward and reverse specific latent heat

3.5.2.1 Cyclic test

The equations developed in Sections 3.4.1 and 3.4.3 are used to further analyze thermal behavior and properties.

Strain Rate analysis

In the following, it is assumed that the deformation mechanism is composed only by elasticity and phase transformation. The effects of plasticity are neglected. In this way, the Eq. 3.5 is rewritten as follows:

$$\dot{\varepsilon} = \dot{\varepsilon}_{el} + \dot{\varepsilon}_{in} = \dot{\varepsilon}_{el} + \dot{\varepsilon}_{tr} \tag{3.22}$$

The transformation strain rate $\dot{\varepsilon}_{tr}$ will be assumed proportional to the martensitic transformation fraction. This is assumed for any phase transformation under tensile loading (McCormick et al., 1993):

$$\dot{\varepsilon}_{tr} = \dot{f}_m \Delta\varepsilon_{tr} \tag{3.23}$$

where $\Delta\varepsilon_{tr}$ stands for the transformation strain for a complete transformation ($f_m = 1$).

Thermal power assumptions

The total thermal power is assumed to be composed only by the presence of thermoelasticity and phase transformation. The dissipation power induced by plasticity ($\dot{q}_{pl}$) is neglected. With that, Eq. 3.6 is rewritten as follows:

$$\dot{q} = \dot{q}_{thel} + \dot{q}_{in} = \dot{q}_{thel} + \dot{q}_{tr} \tag{3.24}$$

with $\dot{q}_{tr} = \dot{f}\Delta H_{tr}$.

Determination of ratio $\frac{\Delta H_{tr}(f_m)}{\Delta\varepsilon_{tr}}$

Using Eqs. 3.10 and 3.23, one obtain the following expression:

$$\frac{\dot{q}_{tr}}{\dot{\varepsilon}_{tr}} = \frac{\dot{q}_{in}}{\dot{\varepsilon}_{in}} = \frac{\dot{q} + \dfrac{\alpha T_0 \dot{\sigma}}{\rho}}{\dot{\varepsilon} - \dfrac{\dot{\sigma}}{E}} = \frac{\Delta H_{tr}(f_m)}{\Delta\varepsilon_{tr}} \tag{3.25}$$

All terms of the right hand side of the Eq. 3.25 were obtained experimentally. The ratio $\dot{q}_{in}/\dot{\varepsilon}_{in}$ is plotted in function of strain and nominal stress as shown in Figs. 3.17a and 3.17b, respectively.

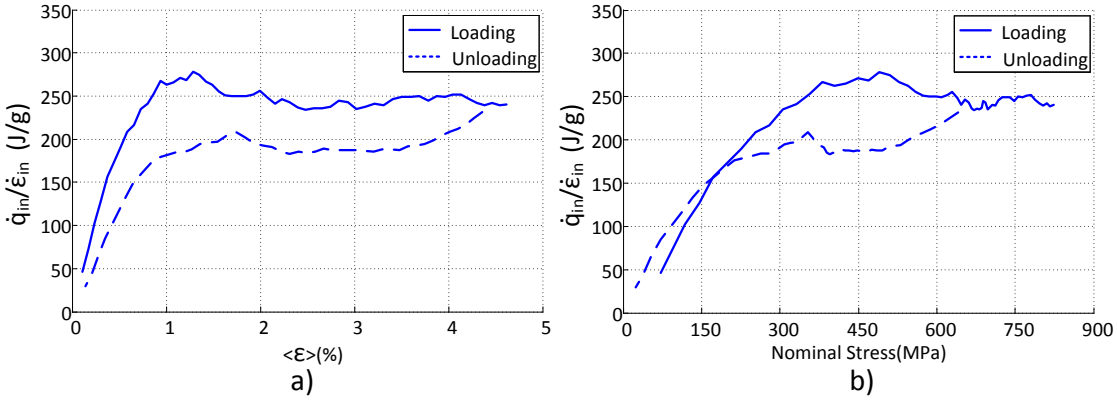

Figure 3.17: *Ratio $\dot{q}_{in}/\dot{\varepsilon}_{in}$, computed using experimental data and Eq. 3.25, as a function of a) strain and b) nominal stress for the cyclic test.*

Observing Fig. 3.17a, it is possible to consider the ratio $\dot{q}_{in}/\dot{\varepsilon}_{in}$ constant for strains between $\varepsilon = 1\%$ and $\varepsilon = 5\%$. Then, assuming the specific latent heat ($\Delta H_{tr}(f_m)$) as a constant in this strain interval it can be rewritten as:

$$\Delta H_{tr} = (\dot{q}_{tr}/\dot{\varepsilon}_{tr})\Delta\varepsilon_{tr} \tag{3.26}$$

Determination of ΔH_{tr}

From Eq. 3.26, it is possible to experimentally obtain the value of the specific latent heat (ΔH_{tr}). Calculating on the strain range between $\varepsilon = 1\%$ and $\varepsilon = 4.5\%$, one obtains: $\Delta H_{tr}^{A-M} = 19.6 \pm 0.4$ J/g for the forward phase transformation and $\Delta H_{tr}^{M-A} = 14.9 \pm 0.2$ J/g for the reverse transformation. The standard deviation is also calculated to take into account the variation in this range.

These values can be compared to the ones obtained by Frenzel et al., 2015 from DSC measurements. They showed that for fully annealed binary NiTi alloys, the values of specific latent heat decrease from about 30 J/g to 10 J/g with the increasing of $at.\%Ni$. For alloys with a composition of $Ti-50.9\,at.\%\,Ni$ the values obtained were around $17 J/g$ (Khalil-Allafi and Amin-Ahmadi, 2009; Frenzel et al., 2015).

Analyzing the relation $\Delta H_{tr}^{A-M} - \Delta H_{tr}^{M-A} = W_{mech}'^{A-M} - W_{mech}'^{M-A}$

As presented in Eq. 3.12, ΔH_{tr} is composed by a chemical enthalpy change ΔH_c, an elastic energy E_{st} stored or released during the process of transformation and a mechanical work $W'_{mech} = \frac{1}{\rho}\sigma\Delta\varepsilon_{tr}$. As shown in Eq. 3.19 the difference between forward and reverse transformation enthalpies (where $\Delta H_{tr}^{A-M} > \Delta H_{tr}^{M-A}$) is further associated only with the mechanical energy (W'_{mech}). Rewriting the Eq. 3.19, one have:

$$\Delta H_{tr}^{A-M} - \Delta H_{tr}^{M-A} = \frac{1}{\rho}\sigma^{A-M}\Delta\varepsilon_{tr} - \frac{1}{\rho}\sigma^{M-A}\Delta\varepsilon_{tr} \tag{3.27}$$

From the thermal analysis, the difference between the specific latent heat on loading and unloading is $\Delta H_{tr}^{A-M} - \Delta H_{tr}^{M-A} = 4.7 \pm 0.6$ J/g. From the mechanical point of view, assuming σ^{A-M} as the mean stress of the forward transformation plateau and σ^{M-A} as the mean stress for the reverse transformation plateau, one obtains the difference of the mechanical energy between loading and unloading $W_{mech}^{\prime A-M} - W_{mech}^{\prime M-A} = 3.5 \pm 0.7$ J/g. The mean stress values as well as the standard deviation were calculated between 1% and 1.5% of transformation strain ε_{tr}. Comparing then the values of $\Delta H_{tr}^{A-M} - \Delta H_{tr}^{M-A} = 4.7 \pm 0.6$ J/g and $W_{mech}^{\prime A-M} - W_{mech}^{\prime M-A} = 3.5 \pm 0.7$ J/g, a difference of 1.2 ± 1.3 J/g is observed. Because of the important standard deviation obtained from both mechanical and thermal approach, it can be assumed that the statement presented in Eq. 3.19 is true.

Analyzing the terms $T\Delta S_c$ ***and*** E'_{fr}

According to Eq. 3.11, the specific latent heat (ΔH_{tr}) is composed by the entropy variation ($T\Delta S_c$) and by the energy dissipated as friction (E'_{fr}). With that, it is possible to calculate the term E'_{fr} for loading and unloading. Taking into account the test temperature variation during loading (θ^{A-M}) and unloading (θ^{M-A}), Eq. 3.11 can be rewritten as follows:

- During loading, A-M:

$$\Delta H_{tr}^{A-M} = -(T + \theta^{A-M})\Delta S_c + E_{fr}^{\prime A-M} \tag{3.28}$$

and,

- During unloading, M-A:

$$\Delta H_{tr}^{M-A} = -(T + \theta^{M-A})\Delta S_c + E_{fr}^{\prime M-A} \tag{3.29}$$

where T stands for the temperature test.

Figure 3.18 shows the average temperature variation $\langle\theta\rangle$ during the test in function of transformation strain $\langle\varepsilon_{tr}\rangle$. The test temperature variation during loading (θ^{A-M}) and unloading (θ^{M-A}) are highlighted by the dashed red and blue lines, respectively. From that, their respective difference ($\theta^{A-M} - \theta^{M-A}$) was calculated and is represented by the black thick line.

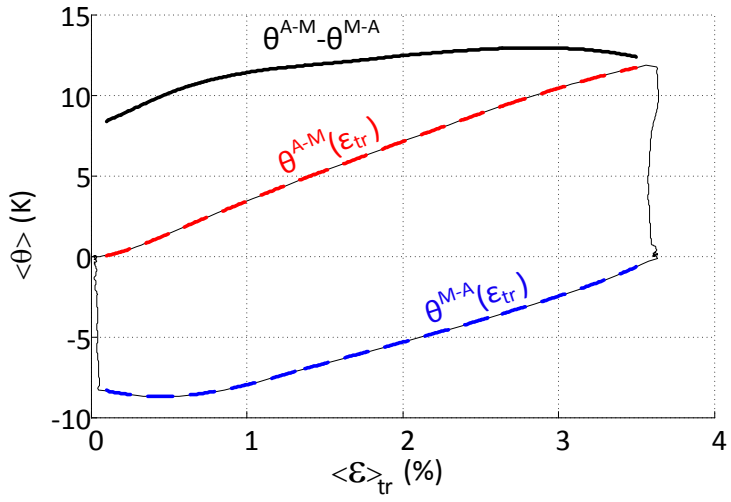

Figure 3.18: *Average temperature variation $\langle\theta\rangle$ in function of the average transformation strain $\langle\varepsilon_{tr}\rangle$. The dashed red line stands for the temperature variation during loading ($\theta^{A-M}(\varepsilon_{tr})$) and the blue dashed line during unloading ($\theta^{M-A}(\varepsilon_{tr})$). The black curve stands for the difference between temperature variation during loading and unloading ($\theta^{A-M} - \theta^{M-A}$).*

Then, using the average value of the $\theta^{A-M} - \theta^{M-A} = 11.8 \pm 1.2$ K and considering an entropy variation $\Delta S_c = -63 \pm 1$ mJ/gK (Khalil-Allafi and Amin-Ahmadi, 2009), the terms of energy due to the entropy variation ($T\Delta S_c$) and dissipated as friction (E'_{fr}) were calculated using Eqs. 3.28 and 3.29.

Then, for a loading-unloading cycle, the energy value due to temperature and entropy variation is:

$$-(\theta^{A-M} - \theta^{M-A})\Delta S_c = 0.7 \pm 0.09 \text{ J/g}.$$

And the value due to the friction energy is:

$$E'^{A-M}_{fr} + \left|E'^{M-A}_{fr}\right| = 4.0 \pm 0.7 \text{ J/g}.$$

The comparison of these values shows that for a SIPT cycle the energy dissipation is predominantly due to the friction energy. However, due to the non isothermal aspect of the test, the thermomechanical coupling term $(T + \theta)\Delta S_c$ is non-negligible.

3.5.2.2 Rupture test

Figure 3.19 presents the ratio $\dot{q}_{in}/\dot{\varepsilon}_{in}$ in function of true strain (Fig. 3.19a) and in function of nominal stress (Fig. 3.19b) for the rupture tensile test. Similarly to the curve observed in Fig. 3.17a, the ratio $\dot{q}_{in}/\dot{\varepsilon}_{in}$ in function of strain increases linearly until 1% and presents a rather constant value from $\sim$ 2% to $\sim$ 7.5% strain. Then, after 7.5%, the ratio shows a nearly linear decrease until the rupture point, around 11% strain. In Fig. 3.19b, the correspondent region is observed between $\sim$ 600 MPa and $\sim$ 1200 MPa. One can notice that after 7.5% (Fig. 3.19a) and $\sim$ 1200 MPa (Fig. 3.19b), the ratio is not constant anymore. In this way, one can assume that the plastic effect cannot be neglected after these values.

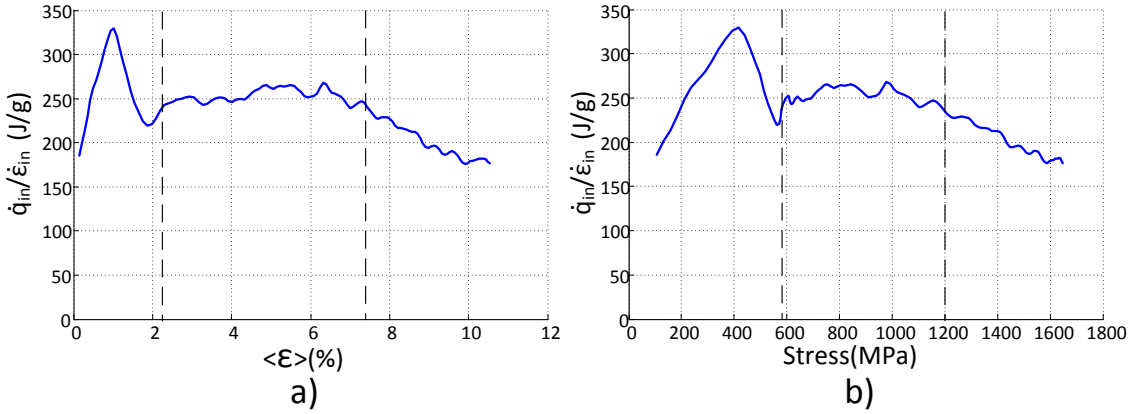

Figure 3.19: *Ratio $\dot{q}_{in}/\dot{\varepsilon}_{in}$ computed with Eq. 3.25 and experimental data, as a function of strain a) and as a function of nominal stress for the rupture test b).*

Figure 3.20a shows the nominal stress vs. true strain. This curve can be separated in three zones: I- from 0% to $\sim$ 2%, II- from $\sim$ 2% to $\sim$ 7.5% and III- from $\sim$ 7.5% until rupture. Zone I may be assumed as having predominantly elastic deformation while zone II shows mostly phase transformation. Finally zone III presents the beginning of a plastic deformation around $\sim$ 7.5%.

Fig. 3.20b presents the ratio $d\sigma/d\varepsilon$ in function of true strain. This ratio is used to analyze the evolution of the apparent modulus with deformation. One can observe that the ratio varies with true strain. Such result indicates that no pure elastic zone is present during the tensile test, otherwise, a constant value of $d\sigma/d\varepsilon$ would be observed. It is known that at the beginning of SIPT, with the material in austenite phase, the elastic modulus decreases during loading, reaching a minimum at about the middle of the stress vs. strain plateau, and restarts to increase again until reaches the martensite phase. With further increase of strain, the ratio $d\sigma/d\varepsilon$ tends to decrease due to the presence of plastic deformation. Because of that, in the Fig. 3.20b, the inflection point around $\sim$ 7.5% strain indicates the begin of plastic deformation. These results support the assumption that the zone between $\sim$ 2% and $\sim$ 7.5% strain contains only (or at least predominantly) phase transformation.

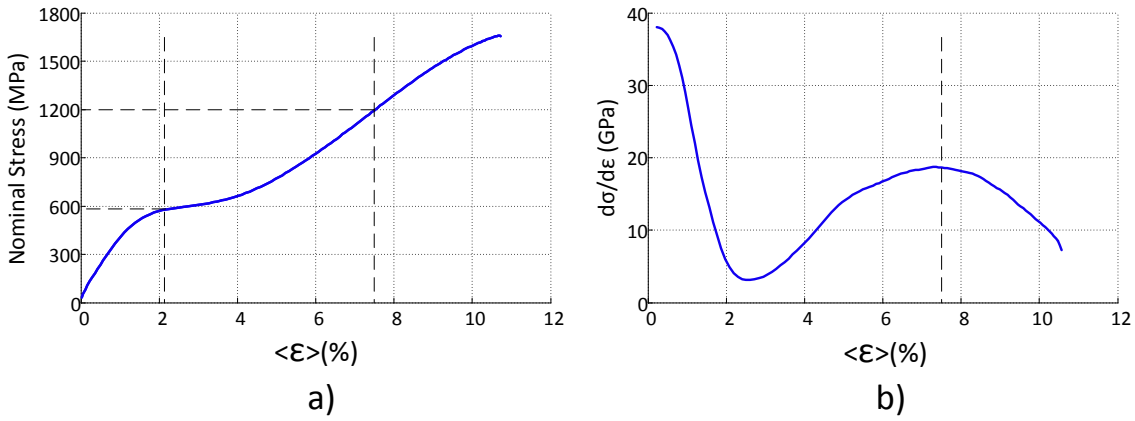

Figure 3.20: *a) Nominal stress vs. true strain. b) And ratio $d\sigma/d\varepsilon$ in function of true strain.*

Then, the specific latent heat (ΔH_{tr}) was treated constant on the interval between $\varepsilon = 2\%$ and $\varepsilon = 7.5\%$ strain. It was calculated using the experimental data shown in Fig. 3.19 and Eq. 3.25. The value $\Delta H_{tr}^{A-M} = 20.2 \pm 1.3 J/g$ was obtained for a transformation strain $\Delta\varepsilon_{tr} = 0.08$. This value agrees with the one obtained for the cyclic test.

3.5.3 Estimation of martensite fraction (f_m)

The martensite fraction was obtained only for the cyclic test, due to the absence of plastic effects. It was calculated by time integration of the martensite fraction rate deduced from Eqs. 3.23 and 3.26, where $\dot{f}_m = \dot{q}_{tr}/\Delta H_{tr}$. For that, the imposed values of $\Delta H_{tr}^{A-M} = 19.6$ J/g for the forward transformation (loading) and $\Delta H_{tr}^{M-A} = 14.9$ J/g for the reverse transformation (unloading) were used.

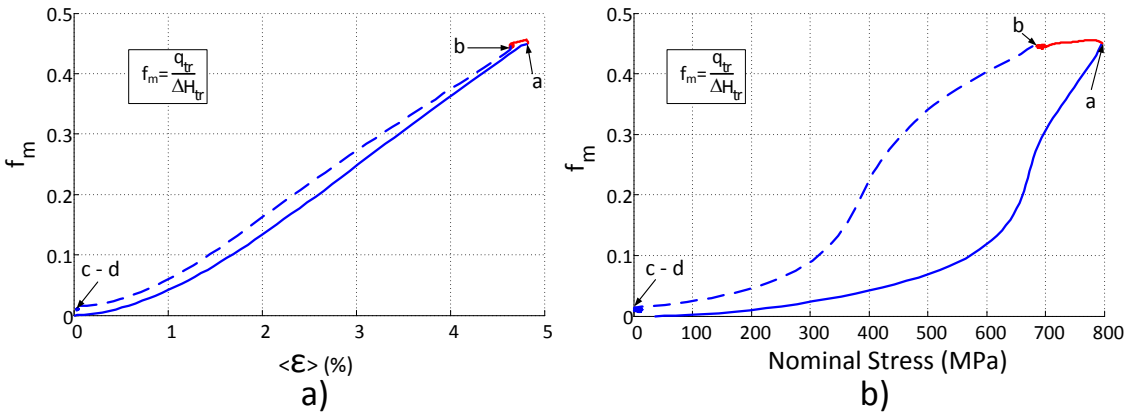

Figure 3.21: *a) Martensite fraction in function of strain. b) Martensite fraction in function of nominal stress.*

Figure 3.21 shows the evolution of the martensite fraction in function of strain (a) and in function of nominal stress (b). Loading is described by the solid line between 0% and point "a" noted in Fig. 3.21. The red-line delimited by points "a" and "b" represents the hold time at the end of loading. Finally, the dashed lines represent the martensite fraction during unloading.

In Fig. 3.21a, the solid curve shows that since the beginning of strain the $A - M$ phase transformation initiates, even before the superelastic plateau. Observing the Fig. 3.21b, during loading, around 5% of martensite is formed between 0 and 400 MPa and more than 10% at 600 MPa. This amount of martensite is present in the strain range of the tensile curve which is commonly considered to be purely elastic. This result ratifies the early increasing amount of thermal power observed at the Figs. 3.8, 3.9 and 3.12.

Between the points (a) and (b), a small decrease of the martensite fraction due to reverse transformation is observed. Such a weak decrease can be explained by the small decrease of the stress during this hold time due to relaxation associated with temperature decrease. In Fig. 3.21b at the beginning of the unloading, between the point (b) and 500 MPa , around 10 % of martensite transforms into austenite.

Despite the apparent full superelastic loop, a martensite fraction maximum of $f_m = 0.45$ is achieved at the end of loading. This behavior does not follow what is commonly assumed in literature that, at the end of superelastic plateau, all the parent phase microstructure is transformed into martensitic phase (Lagoudas, 2008).

New studies (Stebner et al., 2015; Pelton et al., 2015) using neutron diffraction to measure the crystal phase structure show results of the martensitic fraction during a stress induced phase transformation. The path described by the martensite fraction in Fig. 3.21, where its value is higher during unloading than loading, is shown in the work of Pelton et al., 2015. Stebner et al., 2015 obtained a maximum of $f_m = 0.95$, at $\varepsilon = 11\%$ strain, in a stress relieved $NiTi$ rod ($Ti - 50.8\,at\%\,Ni$). Such high value of martensite fraction is expected in stress relieved materials since the grain size tends to increase with the heat treatment and so the phase transformation.

However, numerous studies (Tsuchiya et al., 2006; Waitz et al., 2009; Glezer et al., 2003) reveal that for nanostructured materials, the reduced grain size tends to partially suppress the martensite phase transformation. It has been shown that the grain size reduction decreases exponentially the potency of grains as nucleation sites (Chen et al., 1985). In the present paper, the material used is assumed to have a nanoscale crystalline structure, since it was submitted to a severe cold work fabrication process and suffered a low magnitude heat treatment (Ahadi and Sun, 2014; Tsuchiya et al., 2006) at temperatures below recrystallization. The manufacture history associated with the absence of transformation peak in DSC curve (Tsuchiya et al., 2006) ratifies then the low level of martensite fraction achieved in Fig. 3.21.

3.6 Conclusion

A thermomechanical analysis was performed on a nanostructured cold-worked $Ti - 50.9\,at\%\,Ni$ wire submitted to a heat treatment of $598K$ for $30min$. Using a thermal field measurement (TFM) method it was possible to estimate thermal power and energy generated during a stress induced phase transformation. The same superelastic NiTi wire showed an inconclusive thermal response when tested via DSC technique.

Digital image correlation (DIC) allowed the estimation of mechanical power and energy from the kinematic field measurements. Moreover, it was possible to determine a thermal and mechanical power ratio ($\dot{q}_{in}/P_{mech-in}$) higher than 2, for both loading and unloading, which is evidence of the phase transformation presence.

With the use of a thermomechanical framework it was possible to determine the specific latent heat of phase transformation (ΔH_{tr}). The calculated values of specific latent heat were $\Delta H_{tr}^{A-M} = 19.6 \pm 0.4$ J/g for the forward and $\Delta H_{tr}^{M-A} = 14.9 \pm 0.2$ J/g for the reverse transformation. Values in the same range were found in literature for a fully annealed NiTi alloys tested via the DSC technique.

Finally, an estimation of the martensite fraction in function of strain and nominal stress was performed with the hypothesis of negligible plastic deformation. Under this condition, limiting the global strain to about 5%, a maximum of 45% martensite fraction was observed. It was also observed an increase from 0 to 5% of martensite fraction between 0 and 400 MPa on loading in a commonly said elastic region. Around 10% of martensite fraction recovered in the very beginning of unloading, between 680 MPa and 500 MPa, also in a supposedly elastic region. Such results put into evidence the premature phase transformation phenomenon on the stress induced phase transformation; and its presence along all the superelastic loop.

CHAPTER

FOUR

INFLUENCE OF HEAT TREATMENT ON THE SPECIFIC LATENT HEAT AND MARTENSITE FRACTION OF NANOSTRUCTURED NITI WIRES

This Chapter is written as a paper to be published soon.

ABSTRACT

Shape memory alloys are capable of inducing a considerable temperature change when they are mechanically charged. This phenomenon takes place due to an important thermal and mechanical coupling present during the phase transformation (PT). The latent heat along the PT mechanism corresponds to the energy responsible for the temperature increase. The determination of the specific latent heat (ΔH) of the phase transformation involved in the process, are generally performed by differential scanning calorimetry (DSC). However, depending on the fabrication history of the material, the obtained DSC response is useless on the determination of the ΔH. In this work, a method using digital image correlation (DIC) and thermal field measurements (TFM) is used to obtain this property. A cold worked $Ti - 50.9\,at.\%\,Ni$ wire was submitted to four different heat treatments namely $523K$, $548K$, $573K$ and $598K$ for 30 min. Kinematic and thermal full fields were acquired during superelastic tensile tests. From the experimental results and a thermal approach associated with a thermodynamic framework, it was possible to determine the specific latent heat ΔH for all the heat treated wire during loading and unloading. The ΔH calculated values during loading showed a rather constant behavior, however, the values calculated during unloading showed a decreasing trend with the increase of the heat treatment temperature. The martensite fractions (f_m) were also calculated and showed an evolution with the heat treatments. At the same stress level, 800 MPa for example, values from $f_m = 0.07$ to $f_m = 0.43$ were obtained among the different heat treatments.

Keywords: *Full-field kinematic and thermal approach, nanostructured NiTi wires, heat balance, enthalpy of transformation, martensite fraction.*

Contents

4.1 Introduction

Thermomechanical effects present in martensitic phase transformation in shape memory alloys (SMA) have attracted considerable attention of researchers for the application in elastocaloric cooling devices. Recently, many studies have been conducted and devices designed based on this phenomenon (Wu et al., 2017; Álvarez-Alonso et al., 2017; Pataky et al., 2015; Schmidt et al., 2016). The elastocaloric effect takes place due to entropy change during the phase transformation. An endothermic response happens during the reverse phase transformation and an exothermic response on the direct phase transformation. Under adiabatic conditions the endothermic effect absorbs heat from the surroundings, dropping the material temperature considerably, reaching cooling peaks of 18.2K for NiTi alloys (Wu et al., 2017; Pataky et al., 2015; Tušek et al., 2016a; Tušek et al., 2015; Ossmer et al., 2014; Schmidt et al., 2015b). As the elastocaloric effect is associated to the martensitic phase transformation, the amount of energy involved in this phenomenon depends directly on the volume of transformed phase.

Depending on the fabrication history and heat treatment submitted to SMA, the mechanical and thermal responses can be affected (Ahadi and Sun, 2014). NiTi SMA wires are commonly manufactured through a sequence of hot and cold working (Ahadi et al., 2012; Delville et al., 2010; Mitwally and Farag, 2009) followed by a final heat treatment to perform a recrystallization (Peterlechner et al., 2010; Shi et al., 2014; Sergueeva et al., 2003). The severe plastic deformation during cold working induces a grain size reduction (Ahadi and Sun, 2014) that may lead to a partial amorphization of NiTi SMA (Yu et al., 2016; Tsuchiya et al., 2006). This effect leads to a partial or total suppression of the DSC curve peaks (Ahadi and Sun, 2014; Li et al., 2008; Chang et al., 2006; Tsuchiya et al., 2006; Miller and Lagoudas, 2001). In this way, the use of DSC tests to determine the specific latent heat of phase transformation is useless. However, a superelastic loop is still observed and so a stress induced phase transformation (SIPT) is present (Ahadi and Sun, 2014).

In this case, the specific latent heat may be obtained through the analysis of the thermomechanical coupling during a SIPT. This complex interaction between thermal and mechanical phenomena has been studied by many authors (Ossmer et al., 2014; Zhang et al., 2010; Shaw, 1995; Yin and Sun, 2012; He and Sun, 2010). Heat sources were experimentally obtained through a thermal analysis in CuZnAl SMA by Peyroux et al., 1998b and Balandraud et al., 2005. A thermal approach on the determination of the power generation on a NiTi tube was presented by Favier et al., 2007. Further, Chrysochoos and Louche, 2000 and Schlosser et al., 2007 presented a study with a method to estimate heat sources from temperature fields observed by an infrared thermal camera.

In this context, this work aims to present an experimental and analytical study on the determination of the specific latent heat during a SIPT. Kinematic and thermal full fields measurement methods described in Chapter 3 were used. A thermomechanical analysis performed through the Gibbs free energy was used in the discussion. The tensile tests were performed on a NiTi cold worked wire submitted to heat treatments (HT) of 30 minutes at four different temperatures: 523K, 548K, 573K and 598K. Different levels of

heat sources and thermal and mechanical energies were estimated for each heat treated wire. The main results are discussed in the last part of this Chapter.

4.2 Material and experimental procedures

4.2.1 Material

The material used in the experimental campaign was a commercial NiTi wire of 0.5 mm diameter with a composition of $Ti - 50.9\,at.\%\,Ni$ provided by Fort Wayne Metals. The wire presents a hardened mechanical behavior due to its cold work manufacturing process. Wire specimens were submitted to four heat treatments at the following temperatures: $523K$, $548K$, $573K$ and $598K$ for 30 min in all cases. In the following, the wires are mentioned as $HT\,523K$, $HT\,548K$, $HT\,573K$ and $HT\,598K$, in reference to their respective HT temperature.

4.2.2 Differential scanning calorimetry analysis

Prior to the tensile tests, a DSC analysis was performed on the heat treated wires. The tests were carried out between $223K$ and $363K$ with a heating rate of $10K/min$ in a Q200 (TA Instruments) DSC testing machine.

4.2.3 Experimental setup

Superelastic tensile tests were performed by loading the NiTi wires at a pre-set global deformation of 6% at a strain rate of $10^{-2}s^{-1}$ with a further unloading at the same strain rate. During the complete load-unload cycle, two hold-time steps were performed (of 50 s each) at the end of loading and at the end of unloading, respectively. During all tests, thermal and kinematic full field data were acquired through IR and visible light cameras. The details of the experimental set-up and the data post-processing are explained in Chapter 2.

4.3 Results

4.3.1 DSC responses

Figure 4.1 shows the results of the DSC tests performed in all HT wires. The curves are plotted with an offset of $0.0125W/g$ in the ordinate scale in order to enable comparison, otherwise, the curves would be superimposed.

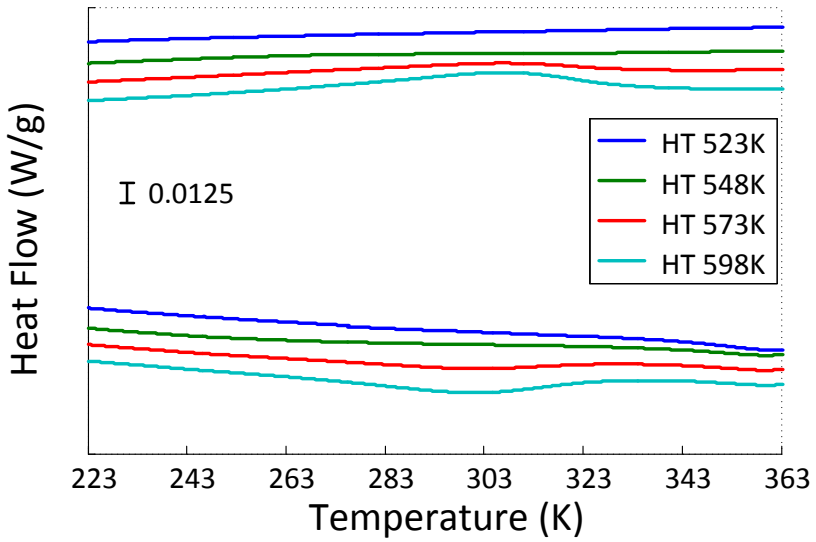

Figure 4.1: *DSC results for the wires with the different heat treatments (The curves are plotted with an offset of* $0.0125 W/g$*).*

For the wires $HT\,523K$, $HT\,548K$ and $HT\,573K$, one can observe that heat flow does not show any peak characterizing the presence of phase transformation. This absence is expected once the heat treatments were performed under the complete recrystallization temperature ($623K$) (Peterlechner et al., 2010; Shi et al., 2014; Sergueeva et al., 2003; Yu et al., 2016). The wire $HT\,598K$, however, shows a minor peak in the heat flow vs temperature curve. Despite its presence, the peak is not well pronounced and cannot be used on the determination of the specific latent heat nor phase transformations critical temperatures. Its use might lead to false conclusions. Such inconclusive DSC responses have already been reported in literature for cold worked materials showing an amorphous or nanosized polycrystalline structure (Tsuchiya et al., 2006; Ahadi and Sun, 2014).

4.3.2 Superelastic mechanical responses

Figure 4.2 shows the superelastic true stress - strain curves of the four wires submitted to different heat treatment temperatures. One can observe the stress level decreasing with the increasing heat treatment temperature. Also, a minor growth on the hysteresis loop can be noticed. Despite the pre-set strain value of 6% imposed to all tests, each sample achieved a different strain level. This is due to the not controllable sliding of the sample on the clamps surface. However, even though showing different strain levels, the further analysis was not compromised.

The curves referent to the results of $HT\,523K$ and $HT\,548K$ wires show a steep loop without any signal of plateau. A kind of "plateau" starts to appear for the $HT\,573K$ wire and is almost fully established for the $HT\,598K$. Finally, at the end of unloading it is

possible to observe the complete strain recovery of the material. Such a behavior ratifies the predominant presence of reversible elastic and phase transformation deformation mechanisms. Irreversible deformation mechanism such as plasticity can be neglected on the analysis.

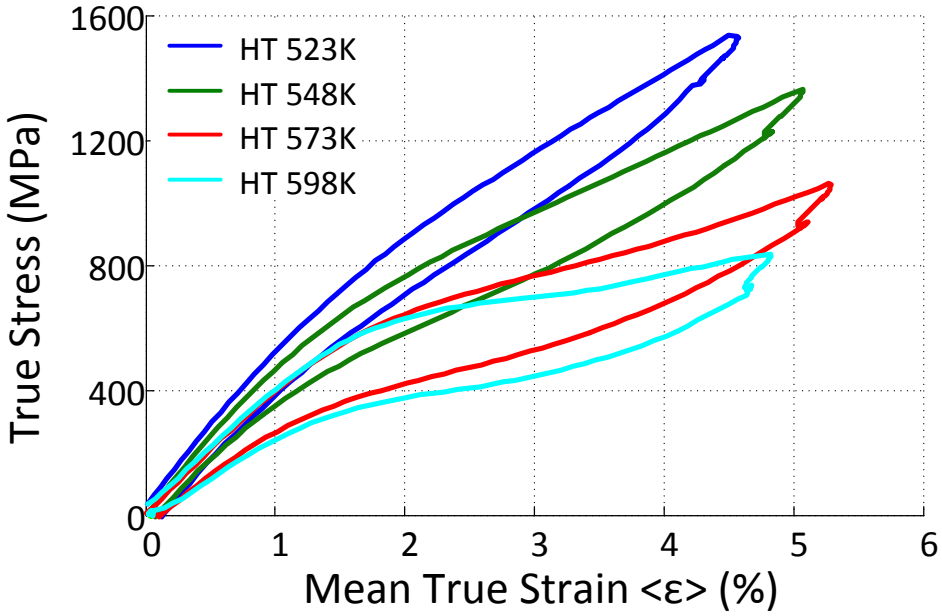

Figure 4.2: *Non-isothermal superelastic $\sigma - \langle\varepsilon\rangle$ tensile test responses for different heat treatment temperatures.*

4.3.3 Strain and temperature fields

Figure 4.3 shows the non-isothermal superelastic $\sigma - \langle\varepsilon\rangle$ tensile responses (a) with their respective strain (b) and temperature variation profiles (c) for each heat treatment temperature, i.e. $HT\,523K$, $HT\,548K$, $HT\,573K$ and $HT\,598K$.

Firstly, one can observe an uniformity on strain and temperature variation profiles. Such stable curves, without any peak nor gradient, point out the absence of localized deformation. From the wire $HT\,523K$, at 5% strain, the temperature increased $6K$ during loading. For almost the same level of strain (around 5%), the temperature increased $9K$ for the wire $HT\,548K$ and about $12K$ for the wires $HT\,573K$ and $HT\,598K$.

As the observed strain (Fig. 4.3b) and temperature (Fig. 4.3c) profiles were uniform, they had been averaged and treated as time dependent only. In this way, each strain point at the $\sigma - \langle\varepsilon\rangle$ curve (Fig. 4.3a) represents the mean value $\langle\varepsilon\rangle$ of each strain profile ε of curves in Fig. 4.3b. The same analysis can be done for the temperature variation profiles θ. They were computed as the difference between the absolute temperature T in the gauge length l_0 and the room temperature T_0, i.e. $\theta = T - T_0$.

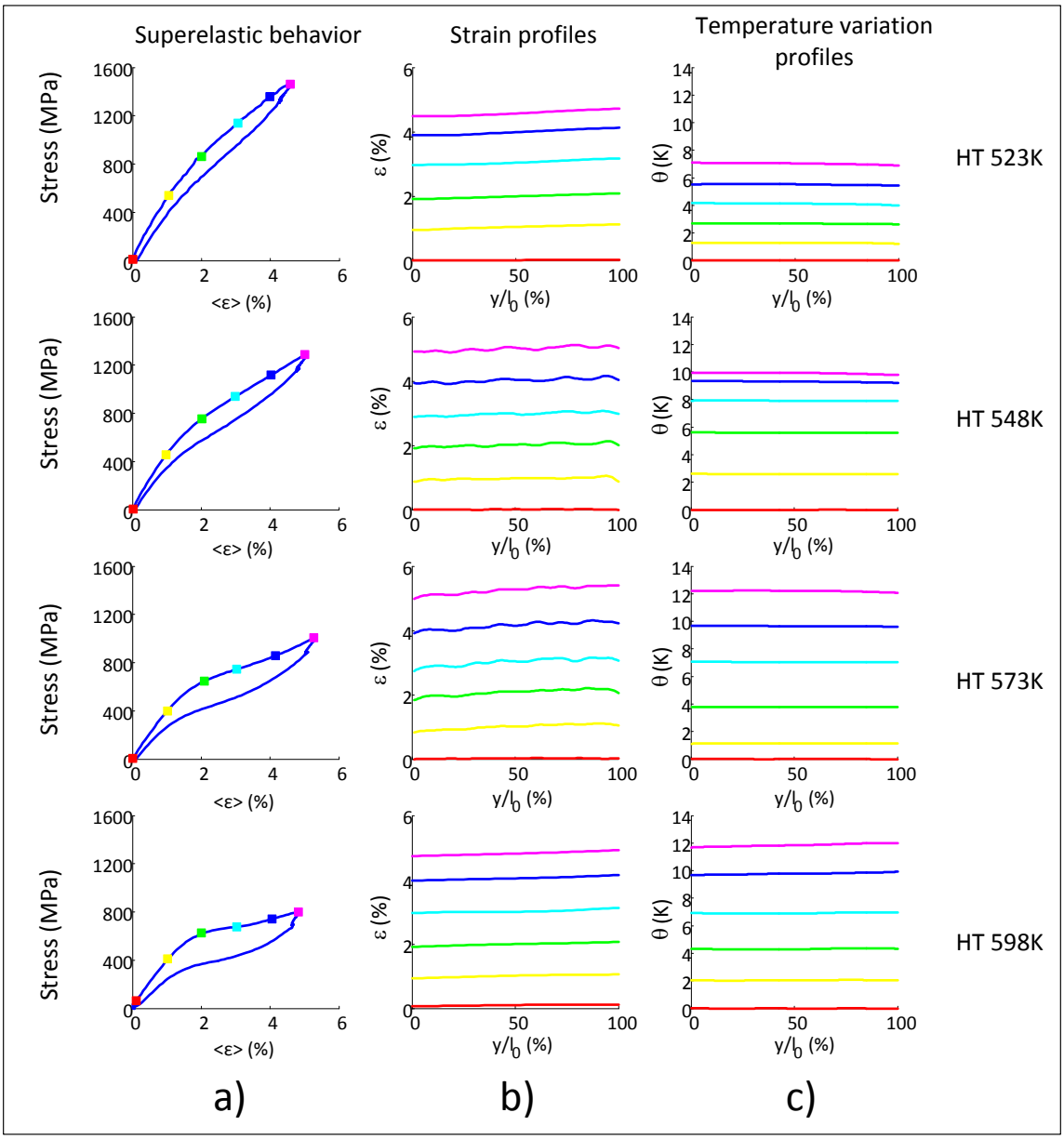

Figure 4.3: *a) Non-isothermal $\sigma - \langle\varepsilon\rangle$ superelastic tensile test responses, b) strain profiles and c) temperature variation profiles of the tensile test performed on the wires heat treated at $523K$, $548K$, $573K$ and $598K$. The strain and temperature profiles correspond to the loading points highlighted in figures of column a.*

Analogously Fig. 4.4 shows the same results of the strain profiles and temperature variation profiles during unloading of all performed tests.

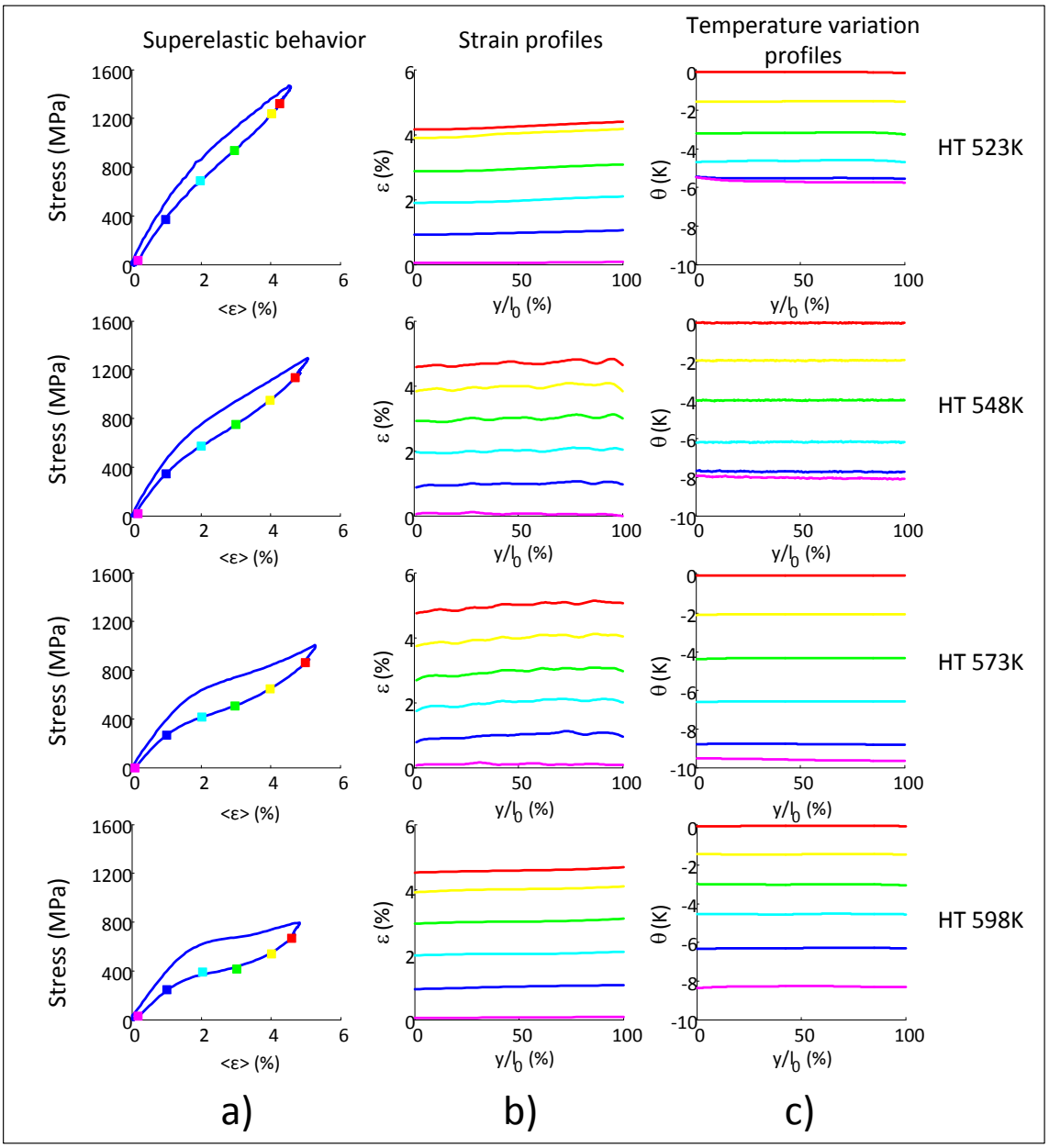

Figure 4.4: *a) Non-isothermal $\sigma - \langle\varepsilon\rangle$ superelastic tensile test responses, b) strain profiles and c) temperature variation profiles of the tensile test performed on the wires heat treated at $523K$, $548K$, $573K$ and $598K$. The strain and temperature profiles correspond to the unloading points highlighted in figures of column a.*

4.4 Thermomechanical analysis

In this Section the results of the thermal and mechanical powers and energies are presented and discussed. These results were obtained experimentally through the experimental data shown in previous section (4.3.3) and the thermal approach extensively discussed in Sections 3.2.4 and 3.2.5 of Chapter 3.

4.4.1 Thermal and mechanical powers

Figure 4.5 shows the mechanical response as well as the thermal ($\dot{q}$) and mechanical power (P_{mech}) responses for all heat treated wires: $HT\,523K$, $HT\,548K$, $HT\,573K$ and $HT\,598K$, in function of mean strain $\langle\varepsilon\rangle$. The green curves represent the stress vs. strain behavior (without data from hold time). The red and blue curves are the thermal and mechanical power, respectively. Finally, the solid dots represent the response during loading, while the hollow dots represent the response during unloading.

Observing the loading portion of thermal power for the different heat treatments, one can notice that the maximum thermal power increases as the heat treatment temperature increases. Also, the thermal power maximum is always present in a strain range of 2% to 4.5%, which implies that the most phase transformation occurs in this strain range. Such strain range covers the middle section of the stress strain curve, away from the initial linear deformation regions where the elastic deformation is supposedly predominant. Between 0 and 1% of strain, a linear increase on thermal power is observed. Despite the predominance of elasticity in this region, this behavior ratifies the presence of phase transformation even for the wire submitted to the lowest heat treatment ($HT\,523K$).

Due to cold work, the grain size reduction drastically decreases the nucleation of phase transformation (Ahadi and Sun, 2014). With the grain growth promoted by the heat treatment, the nucleation barrier to phase transformation decreases. In this way, the thermal power released shows a considerable increase since more material transforms as the grains grow. On loading, the thermal power peaks values increased from $1.1W/g$ for the wire $HT\,523K$ to $2.1W/g$ for the one $HT\,598K$, which represents a 91% increase. During unloading thermal power also showed an important decrease with the increasing heat treatment temperature. The difference observed reached 70% in the absolute value, from $-1.0W/g$ for the wire $HT\,523K$ to $-1.7W/g$ for the one $HT\,598K$.

During loading, the maximum values of mechanical power showed a slight decrease with the increasing heat treatment, from $1.5W/g$ for the wire $HT\,523K$ to $1.0W/g$ for the $HT\,598K$. During unloading the same variation observed was of $-1.3W/g$ for the wire $HT\,523K$ to $-0.8W/g$ for the $HT\,598K$.

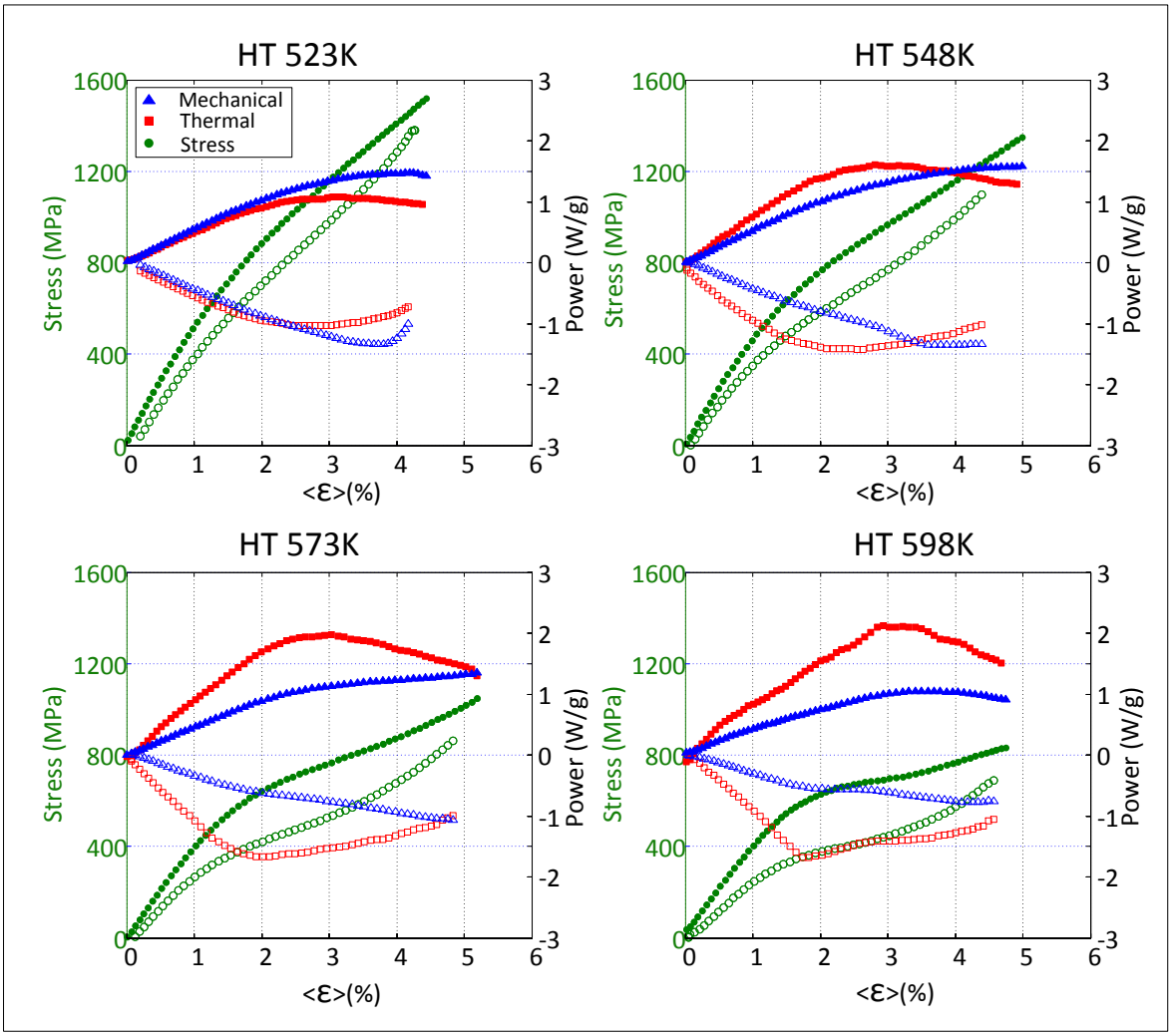

Figure 4.5: *Stress vs. true strain on the left ordinate axis represented by the green dots. Power vs. true strain on the right ordinate axis where the red dots represent thermal power ($\dot{q}$) and blue dots the mechanical power (P_{mech}). Dots represent the loading while the circles represent the unloading.*

In order to take into account the variation of the strain rate during test (because of the sliding of sample), thermal and mechanical powers were normalized by the strain rate.

Figure 4.6 shows the thermal $\dot{q}/\dot{\varepsilon}$ and mechanical $P_{mech}/\dot{\varepsilon}$ powers normalized by the strain rate in function of true strain. After normalization, one can observe the same qualitative response of thermal power. This result emphasizes the stronger presence of phase transformation after 2% strain observed for all heat treatments.

The Quinney-Taylor coefficient establishes the ratio between the inelastic heat source and the inelastic work invested in deforming a material. Rittel, 1999 measured this fraction and found for copper specimens a value in the order of 0.9. For SMA this coefficient tends to be bigger once the heat is induced by the phase transformation.

To investigate the relation between the thermal and mechanical powers, Fig. 4.6 shows in the right ordinate axis their ratio. One can observe the increasing behavior of the normalized thermal power over of the normalized mechanical one with the increase of heat treatment temperature. At 3% strain, the ratio increases from $\dot{q}/P_{mech} \cong 0.8$ to $\dot{q}/P_{mech} \cong 2.1$, between the $HT\,523K$ and $HT\,598K$ wires, respectively. These values quantify the increase of the phase transformation with the heat treatments. Previous results in the literature have shown a ratio of 10 for a polycrystalline CuZnAl SMA (Peyroux et al., 1998b).

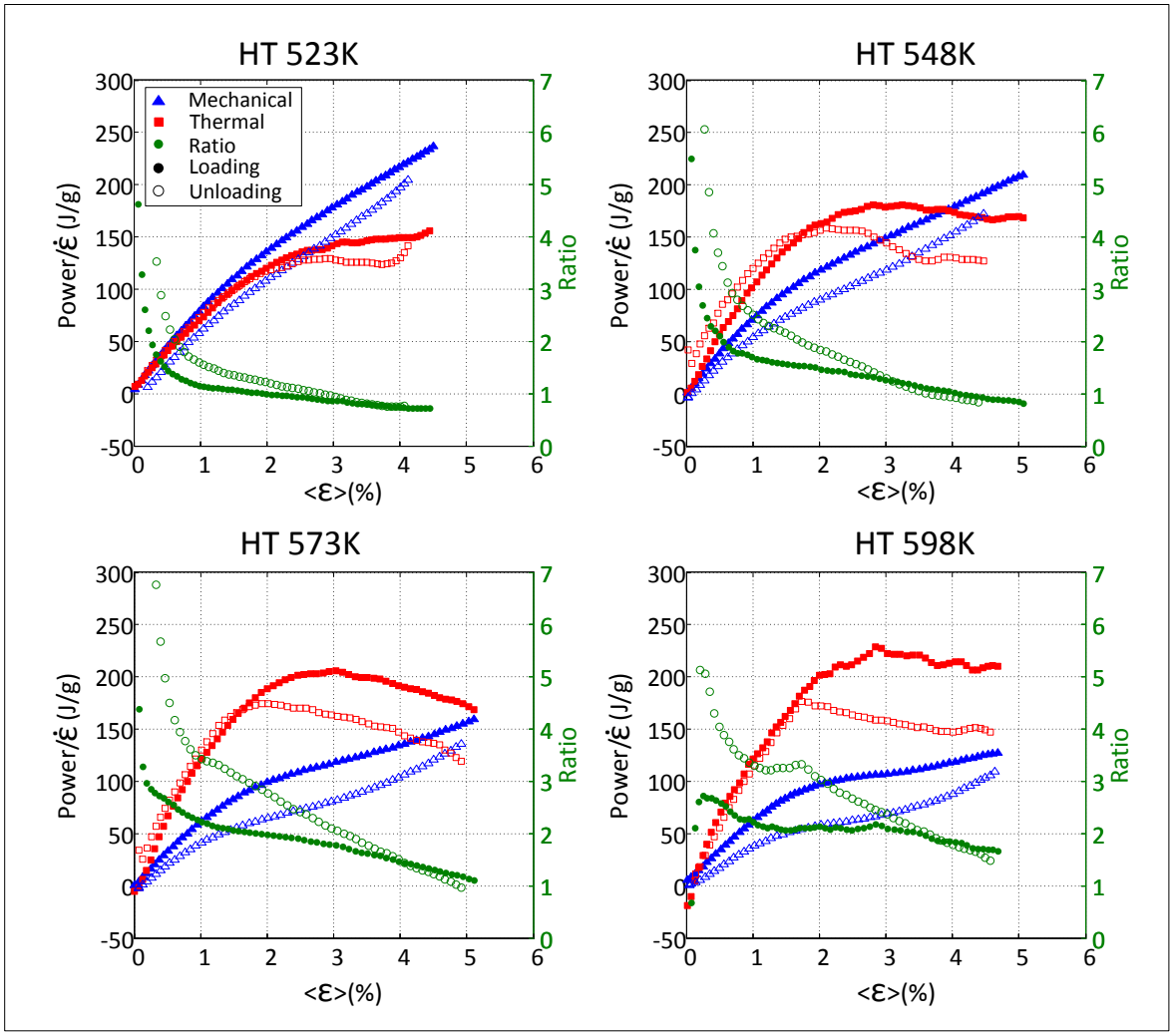

Figure 4.6: *Thermal and mechanical powers normalized by the strain rate ($\dot{q}/\dot{\varepsilon}$ and $P_{mech}/\dot{\varepsilon}$, respectively) on the left ordinate axis and Ratio between thermal and mechanical powers $\dot{q}/P_{mech}$, on the right ordinate axis.*

4.4.2 Thermal and mechanical energies

Figure 4.7 presents stress, thermal energy and mechanical energy in function of strain for all heat treated wires: $HT\,523K$, $HT\,548K$, $HT\,573K$ and $HT\,598K$. The stress vs.

strain curve is shown by green dots while thermal and mechanical energies are shown by red and blue dots, respectively. The solid dots represent the response during loading, while the hollow dots represent the response during unloading.

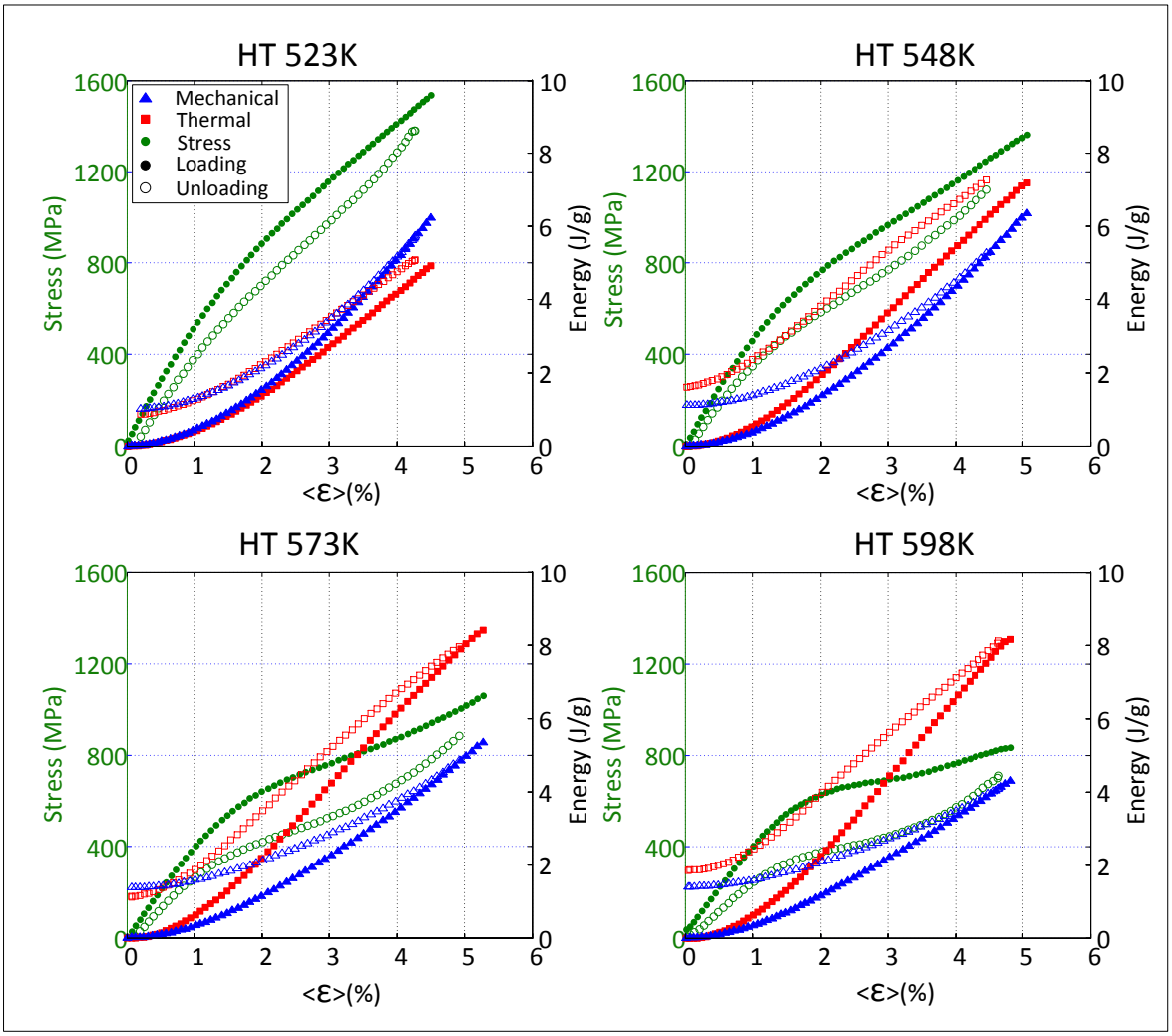

Figure 4.7: *Stress (on the left ordinate axis) and energy (on the right ordinate axis) vs. mean true strain. The green dots represent the stress-strain curve, while the red and blue dots represent thermal and mechanical energies, respectively. Dots are for loading and circles represent unloading.*

For all the heat treatments, the curves of the thermal energies increase regularly during all the loading path. This increasing behavior is even observed at the beginning of loading, in the strain range of 0 to 1%, where is often assumed to present only elastic effect. As noted before while observing the power responses, such positive values of energy can be explained by the presence of phase transformation very early in the deformation process. After 1%-1.5% the evolution of thermal energy is more important, showing an increase of the exothermic heat sources of phase transformation. The same analysis can be done during unloading, the thermal energy decrease is more pronounced up to 1% strain.

One can note also that thermal energy values increase with increasing temperature of heat treatment. As discussed in the previous section, as the grains grow due to the heat treatment magnitude, the amount of released/absorbed energy increases. The wire $HT\,523K$ showed a thermal energy at 4% strain of 4.3 J/g while the $HT\,598K$ showed 6.8 J/g for the same strain level, reaching 8.2 J/g at the end of loading.

The mechanical energy shows an opposite behavior. It shows a considerable decrease with the increase of heat treatment temperature, from 6 J/g for the $HT\,523K$ wire to 4.4 J/g for the $HT\,598K$ wire. However, the hysteresis area of the stress strain curve, increased from 1.0 J/g for the $HT\,523K$ wire to 1.4 J/g for the $HT\,598K$ wire. Both results agree with the fact that the increasing heat treatment temperature increases the grainsize which contribute to the SIPT. A similar result was obtained by Ahadi and Sun, 2014 when testing a Ni-rich NiTi sheet submitted to different heat treatments.

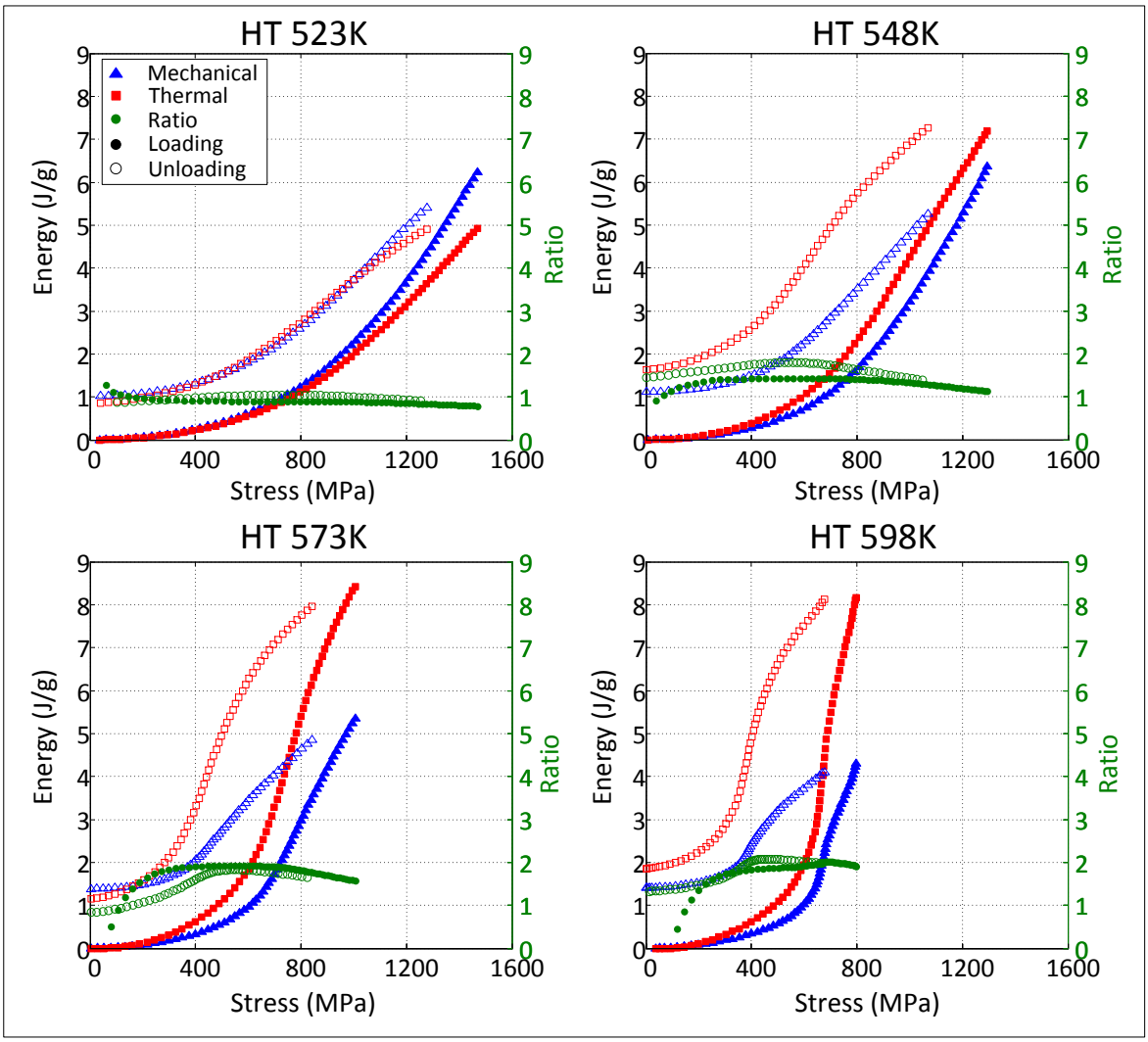

Figure 4.8: *Thermal (red curve) and mechanical (blue curve) energies in the left ordinate axis with their ratio (green curve) in right ordinate axis in function of stress.*

The thermal energy at the end of unloading, was 0.9 J/g for the $HT\,523K$ wire and 1.8 J/g for the $HT\,598K$ wire. These values close to the values of mechanical energies at the end of the cycle (hysteresis area) lead to the same result given in Chapter 3, i.e. the mechanical cycle was a thermodynamic cycle.

Figure 4.8 shows the thermal and mechanical energies per unit of mass in function of stress, represented by red and blue dots respectively. Green dots stands for the ratio between them. Thermal and mechanical energies show a nonlinear response with stress, differently from the observed in Fig. 4.7. This behaviour becomes more evident with the increase of heat treatment temperature. At the same stress level, 800 MPa for example, the $HT\,523K$ wire shows a thermal energy of 1.1 J/g while the wire $HT\,598K$ shows a value of 7.2 J/g. The same qualitative behaviour is observed for the mechanical energy but in a reduced magnitude.

Analogously to the Fig. 4.6, one can observe the increasing behavior of the ratio between thermal and mechanical energies with the increase of heat treatment temperature. An increase from $E_{therm}/E_{mech} \cong 0.8$ to $E_{therm}/E_{mech} \cong 2$, is observed between the $HT\,523K$ and $HT\,598K$ wires, respectively.

4.5 Influence of heat treatment temperature on latent heat and martensite fraction

4.5.1 The specific latent heat

4.5.1.1 Method to determine ΔH_{tr}

The specific latent heat was obtained from the results presented in the previous section computed through the thermodynamic framework based on the Gibbs free energy, presented more in detail in Chapter 3. However a succinct description is presented in the following.

In our analysis it is assumed that the deformation mechanism is composed only by elasticity and phase transformation. The effects of plasticity are neglected. Thus, the strain rate is written as:

$$\dot{\varepsilon} = \dot{\varepsilon}_{el} + \dot{\varepsilon}_{in} = \dot{\varepsilon}_{el} + \dot{\varepsilon}_{tr} \tag{4.1}$$

with $\dot{\varepsilon}_{el}$ standing for the elastic strain rate, $\dot{\varepsilon}_{in}$ standing for the inelastic strain rate and $\dot{\varepsilon}_{tr}$ the transformation strain rate. The elastic strain rate is calculated from the relation $\dot{\varepsilon}_{el} = \dot{\sigma}/E$. Where the stress rate ($\dot{\sigma}$) is experimentally obtained and the elastic modulus used is E=70 GPa (Šittner et al., 2014).

For any phase transformation, under tensile loading, the transformation strain rate

$\dot{\varepsilon}_{tr}$ is assumed to be proportional to the martensitic transformation fraction rate ($\dot{f}_m$) (McCormick et al., 1993):

$$\dot{\varepsilon}_{tr} = \dot{f}_m \Delta\varepsilon_{tr} \tag{4.2}$$

where $\Delta\varepsilon_{tr}$ stands for the transformation strain for a complete transformation where the martensite fraction is $f_m = 1$.

The heat source or thermal power released/absorbed during the tensile test reflects the manifestation of two mechanisms: thermoelasticity and phase transformation. Heat sources due to plasticity are neglected. Thus, thermal power is written in two components, a thermoelastic ($\dot{q}_{thel}$) and a phase transformation ($\dot{q}_{tr}$) one. Then, the thermal power shown in Subsection 4.4.1 can be written as:

$$\dot{q} = \dot{q}_{thel} + \dot{q}_{tr} = -\frac{\alpha T_0 \dot{\sigma}}{\rho} + \dot{q}_{tr} \tag{4.3}$$

where the α is the coefficient of thermal expansion ($\alpha = 1.1 \times 10^{-5} K^{-1}$), T_0 the test temperature, ρ the mass density and $\dot{\sigma} = d\sigma/dt$.

Finally, the specific latent heat ($\Delta H_{tr}(f_m)$) is calculated through the ratio between the transformation thermal power ($\dot{q}_{tr}$) and the transformation strain rate ($\dot{\varepsilon}_{tr}$), as described by Eq. 4.4:

$$\frac{\Delta H_{tr}(f_m)}{\Delta\varepsilon_{tr}} = \frac{\dot{q}_{tr}}{\dot{\varepsilon}_{tr}} \tag{4.4}$$

4.5.1.2 Calculating the ratio $\frac{\dot{q}_{tr}}{\dot{\varepsilon}_{tr}}$ in function of strain and stress

The ratio between the two experimental data, namely the transformation thermal power and the transformation strain rate ($\dot{q}_{tr}/\dot{\varepsilon}_{tr}$) is plotted in Fig. 4.9 in function of the true strain and stress, during loading (Fig. 4.9a) and unloading (Fig. 4.9b).

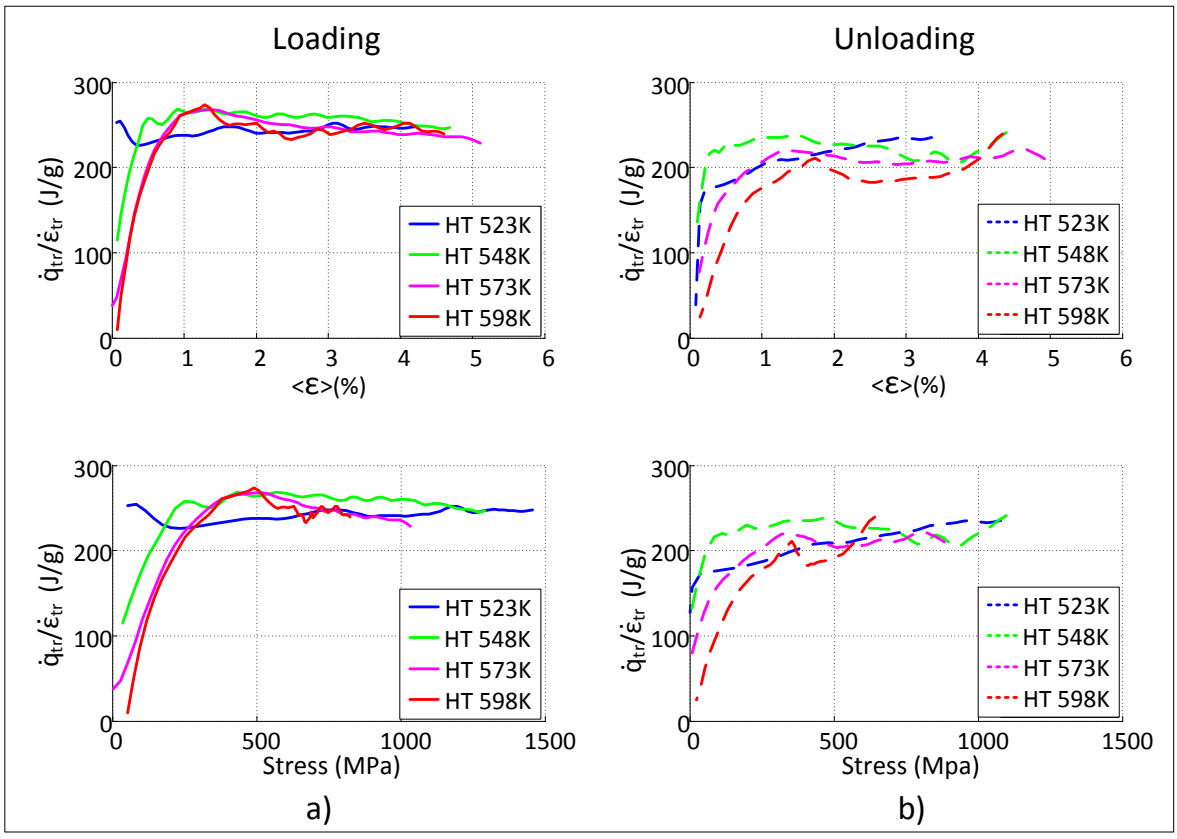

Figure 4.9: *Ratio $\dot{q}_{tr}/\dot{\varepsilon}_{tr}$, computed with experimental data and Eq. 4.4, as a function of strain and stress during a) loading and b) unloading for all heat treated wires.*

The ratio $\dot{q}_{tr}/\dot{\varepsilon}_{tr}$ in function of true strain during loading and unloading shows a rather constant trend between 1% and 5% strain. This behavior implies that the specific latent heat (ΔH_{tr}) is constant and not a function of the martensite fraction ($\Delta H_{tr}(f_m)$) in this strain interval. Thus, the specific latent heat can be computed thanks to this ratio and the knowledge of the transformation strain ($\Delta\varepsilon_{tr}$) on the strain interval between $\varepsilon = 1\%$ and $\varepsilon = 5\%$.

$$\Delta H_{tr} = (\dot{q}_{tr}/\dot{\varepsilon}_{tr})\Delta\varepsilon_{tr} \tag{4.5}$$

A value of $\Delta\varepsilon_{tr} = 0.08$, experimentally obtained in Section 3.5.1 of Chapter 3, was taken into account in the following.

4.5.1.3 Determination of ΔH_{tr} for all heat treatments

Table 4.1 shows the mean values of the specific latent heat calculated between $\varepsilon = 1\%$ and $\varepsilon = 5\%$, referent to the loading and unloading for all the heat treated wires. These values are in a good agreement with the ones obtained by Frenzel et al., 2015 from DSC

measurements. They showed that for fully annealed binary NiTi alloys, the values of specific latent heat decrease from about $30 J/g$ to $10 J/g$ with the increasing of at.% Ni. For alloys with a composition of $Ti-50.9\,at.\%\,Ni$ the values obtained were around $17 J/g$ (Frenzel et al., 2015).

Table 4.1: Mean values of the sçpecific latent heat during loading and unloading for all the heat treated wires.

	ΔH_{tr}^{A-M}	ΔH_{tr}^{M-A}
HT 523 **K**	19.6 ± 0.3 J/g	18.0 ± 0.7 J/g
HT 548 **K**	20.6 ± 0.4 J/g	17.9 ± 0.8 J/g
HT 573 **K**	19.6 ± 0.7 J/g	16.9 ± 0.4 J/g
HT 598 **K**	19.6 ± 0.4 J/g	14.9 ± 0.2 J/g

Figure 4.10a shows the obtained mean values and statistical data presented in Table 4.1. One can notice that the obtained values of specific latent heat (ΔH_{tr}^{A-M}) during loading (red curve) do not show any important variation with the increasing heat treatment temperature. Such a behavior is rather expected since it is known that the specific latent heat depends mostly on the alloy's composition. However, a decreasing behavior with the increasing HT temperature can be observed during unloading. So, the difference between loading (ΔH_{tr}^{A-M}) and unloading (ΔH_{tr}^{M-A}) specific latent heats increases with the increasing of HT temperature (see Fig. 4.10b).

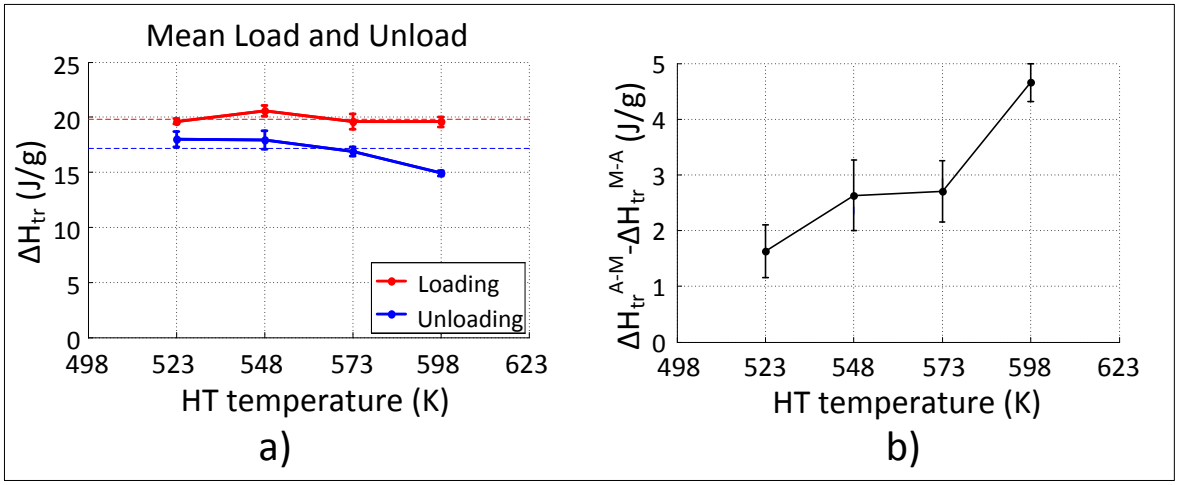

Figure 4.10: *a) Specific latent heat, with their respective standard deviation, determined for each wire during loading (red data) and unloading (blue data). Dashed line representing the total average values of specific latent heat (ΔH_{tr}) for loading and unloading. b) Evolution of the difference between the specific latent heat of loading and unloading ($\Delta H_{tr}^{A-M} - \Delta H_{tr}^{M-A}$) in function of heat treatment temperature.*

4.5.2 Analyzing the relation $\Delta H_{tr}^{A-M} - \Delta H_{tr}^{M-A} = W'^{A-M}_{mech} - W'^{M-A}_{mech}$

From the thermodynamic framework based on the Gibbs free energy (presented and discussed in chapter 3), ΔH_{tr} can be written as composed by a chemical enthalpy change (ΔH_c), an elastic energy (E_{st}) stored or released during the process of transformation and a mechanical work ($W'_{mech} = \frac{1}{\rho}\sigma\Delta\varepsilon_{tr}$) (see Eq.3.12), i.e:

$$\Delta H_{tr}(f_m)\dot{f}_m = (-\Delta H_c - E'_{st}(f_m) + W'_{mech}(f_m))\dot{f}_m \tag{4.6}$$

Analyzing then for a cycle, the chemical enthalpy change (ΔH_c) and the elastic energy (E_{st}) are assumed to be equal for loading and unloading, so the difference between forward and reverse transformation specific latent heat may be written only in function of the mechanical work (W'_{mech}). In this way, specific latent heat variation between loading and unloading ($\Delta H_{tr}^{A-M} - \Delta H_{tr}^{M-A}$) can also be calculated from the mechanical energy difference between loading and unloading ($W'^{A-M}_{mech} - W'^{M-A}_{mech}$). Then, rewriting Eq. 4.6, one has:

$$\Delta H_{tr}^{A-M} - \Delta H_{tr}^{M-A} = \frac{1}{\rho}\sigma^{A-M}\Delta\varepsilon_{tr} - \frac{1}{\rho}\sigma^{M-A}\Delta\varepsilon_{tr} \tag{4.7}$$

with σ^{A-M} and σ^{M-A} stand for the stress on forward ($A-M$) and reverse ($M-A$) transformations.

Table 4.2: Mean values of the mechanical work ($W'^{A-M}_{mech} - W'^{M-A}_{mech}$) and the specific latent heat ($\Delta H_{tr}^{A-M} - \Delta H_{tr}^{M-A}$) between loading and unloading for all the heat treated wires.

	$\Delta H_{tr}^{A-M} - \Delta H_{tr}^{M-A}$	$W'^{A-M}_{mech} - W'^{M-A}_{mech}$
HT 523 **K**	1.6 ± 1.0 J/g	2.2 ± 0.9 J/g
HT 548 **K**	2.7 ± 1.2 J/g	2.4 ± 0.6 J/g
HT 573 **K**	2.7 ± 1.1 J/g	2.8 ± 0.5 J/g
HT 598 **K**	4.7 ± 0.6 J/g	3.5 ± 0.7 J/g

The values of $\Delta H_{tr}^{A-M} - \Delta H_{tr}^{M-A}$ were computed from Table 4.1 and are shown in Table 4.2 for all heat treated wires. The values of $W'^{A-M}_{mech} - W'^{M-A}_{mech}$ were computed using the right member side of Eq. 4.7. The mean values of σ^{A-M} and σ^{M-A} and their respective standard deviations were calculated in a strain range between 1% and 1.5% of the transformation strain ε_{tr}. This range was used in order to perform an equivalent analysis between all the tested wires. The obtained results are presented in Table 4.2.

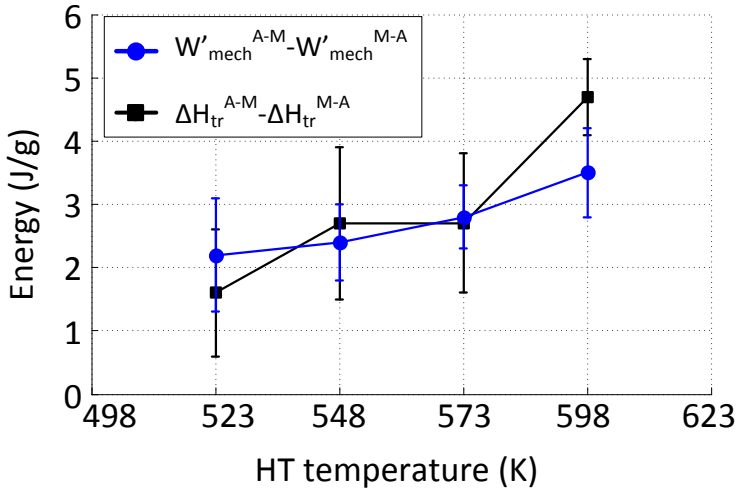

Figure 4.11: *Comparison between specific latent heat variation between loading and unloading calculated with thermal data* $\Delta H_{tr}^{A-M} - \Delta H_{tr}^{M-A}$ *(black curve) and mechanical hysteresis* $W_{mech}'^{A-M} - W_{mech}'^{M-A}$ *(blue curve).*

For a better analysis, the values presented in Table 4.2 were plotted in Fig. 4.11. Despite the slight difference between the thermal and mechanical values, one can observe the agreement between the difference of the specific latent heat variation between loading and unloading ($\Delta H_{tr}^{A-M} - \Delta H_{tr}^{M-A}$) and the mechanical work between loading and unloading ($W_{mech}'^{A-M} - W_{mech}'^{M-A}$). Such a result ratifies Eq. 4.7 and confirms the assumptions made to develop it.

4.5.3 Analyzing the friction energy variation $E_{fr}'^{A-M} - E_{fr}'^{M-A}$

From the Gibbs free energy (presented and discussed in chapter 3), the specific latent heat ΔH_{tr} can be written in terms of the entropy variation $-T\Delta S_c$ (with T standing for the test temperature) and a friction energy E_{fr}', see Eq. 3.11. From this statement, analyzing then the variation of the friction energy in a loading-unloading cycle, the Eqs. 3.28 and 3.29, can be written as follows:

$$\Delta H_{tr}^{A-M} - \Delta H_{tr}^{M-A} = -(\theta^{A-M} - \theta^{M-A})\Delta S_c + (E_{fr}'^{A-M} - E_{fr}'^{M-A}) \tag{4.8}$$

Figure 4.12 shows the difference of the temperature variation during loading and unloading ($\theta^{A-M} - \theta^{M-A}$) in function of the average transformation strain (ε_{tr}). The methodology used to determine these curves has been presented in Chapter 3 by the Fig. 3.18.

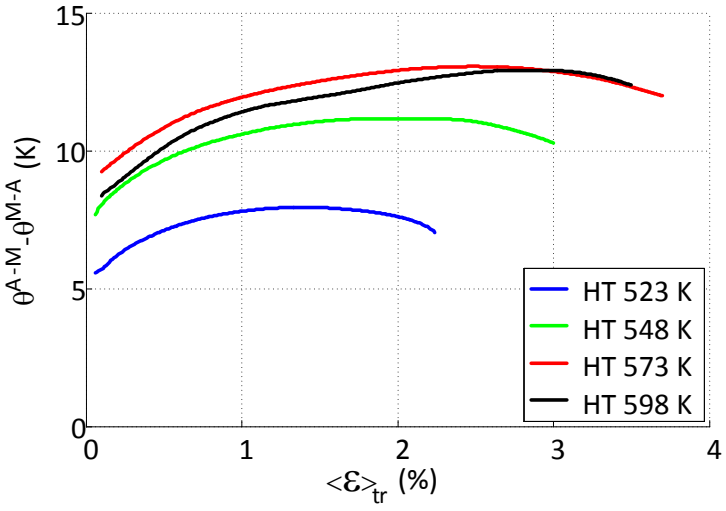

Figure 4.12: *Difference between the average temperature variation during loading and unloading $\theta^{A-M} - \theta^{M-A}$ in function of the average transformation strain ε_{tr} for all heat treatment temperatures.*

Calculating the mean values and their respective standard deviation from the curves showed in Fig. 4.12, one obtain for each test:

Table 4.3: Averaged temperature variation between loading and unloading $\theta^{A-M} - \theta^{M-A}$.

	$\theta^{A-M} - \theta^{M-A}$
HT 523 **K**	7.4 ± 0.6 K
HT 548 **K**	10.5 ± 0.8 K
HT 573 **K**	12.2 ± 0.9 K
HT 598 **K**	11.8 ± 1.2 K

Using the values of $\theta^{A-M} - \theta^{M-A}$ from Table 4.3, the specific latent heat variation $(\Delta H_{tr}^{A-M} - \Delta H_{tr}^{M-A})$ from Table 4.2 and considering an entropy variation $\Delta S_c = -63 \pm 0.2$ mJ/gK (Khalil-Allafi and Amin-Ahmadi, 2009), the values of the energies involved in a SIPT cycle were calculated for all heat treatment temperatures. The energies due to the temperature and entropy variations $(-(\theta^{A-M} - \theta^{M-A})\Delta S_c)$ and the friction energy variations $(E_{fr}'^{A-M} - E_{fr}'^{M-A})$ are shown in Table 4.4.

Table 4.4: Values of the energies due to the temperature and entropy variations ($-(\theta^{A-M} - \theta^{M-A})\Delta S_c$) and friction energies ($E'^{A-M}_{fr} + \left|E'^{M-A}_{fr}\right|$) between loading and unloading for all the heat treated wires.

	$-(\theta^{A-M} - \theta^{M-A})\Delta S_c$	$E'^{A-M}_{fr} + \left\|E'^{M-A}_{fr}\right\|$
HT 523 **K**	0.5 ± 0.04 J/g	1.1 ± 1.0 J/g
HT 548 **K**	0.7 ± 0.05 J/g	2.0 ± 1.2 J/g
HT 573 **K**	0.8 ± 0.06 J/g	1.9 ± 1.2 J/g
HT 598 **K**	0.7 ± 0.09 J/g	4.0 ± 0.6 J/g

The obtained values show that the dissipated energy present in the SIPT cycle are composed by a non-negligible parcel from the temperature and enthalpy variation ($-T\Delta S_c$) and a parcel from the friction energy (E'_{fr}). One can observe that the friction energy term increases with the increasing of the HT temperature while the energy due to the entropy contribution remains rather constant. It is observed that independently of the heat treatment temperature, the dissipated energy is mostly due to the friction energy rather then the temperature and entropy term. The increase of the energy friction term is justified by the increase of phase transformation with the heat treatment temperature. This phenomenon takes place due to the increase of the moving interfaces during phase transformation (Wollants et al., 1993).

4.5.4 Martensite fraction (f_m)

The martensite fraction was calculated by time integration of the martensite fraction rate ($\dot{f}_m$) deduced from Eq. 4.5. The values of the specific latent heat corresponding to loading (ΔH^{A-M}_{tr}) and unloading (ΔH^{M-A}_{tr}) used to calculate the fraction rate ($\dot{f}_m$) are the ones shown at Table 4.1.

Figure 4.13 shows the evolution of the martensite fraction in function of strain (a) and in function of stress (b). The solid lines represent the f_m evolution during loading, while the dashed lines represents the f_m evolution during unloading.

On Fig. 4.13a, the solid curves show that since the beginning of strain (around 0.1% strain) the f_m starts to increase. From 0 to 1% strain, an increase of almost 5% in f_m is observed. A steeper increase is observed from 1% until the end of loading. Such behavior is observed in all heat treated wires.

It is known that martensitic phase transformation occurs by nucleation and growth of crystals in the parent phase matrix. It has been shown that the grain size reduction decreases exponentially the potency of grains as nucleation sites (Chen et al., 1985). Numerous studies (Tsuchiya et al., 2006; Waitz et al., 2009; Glezer et al., 2003) reveal that nanostructured materials tend to partially suppress the martensite phase transformation. The heat treatment acts backwards to this process increasing the grainsize and

promoting the phase transformation.

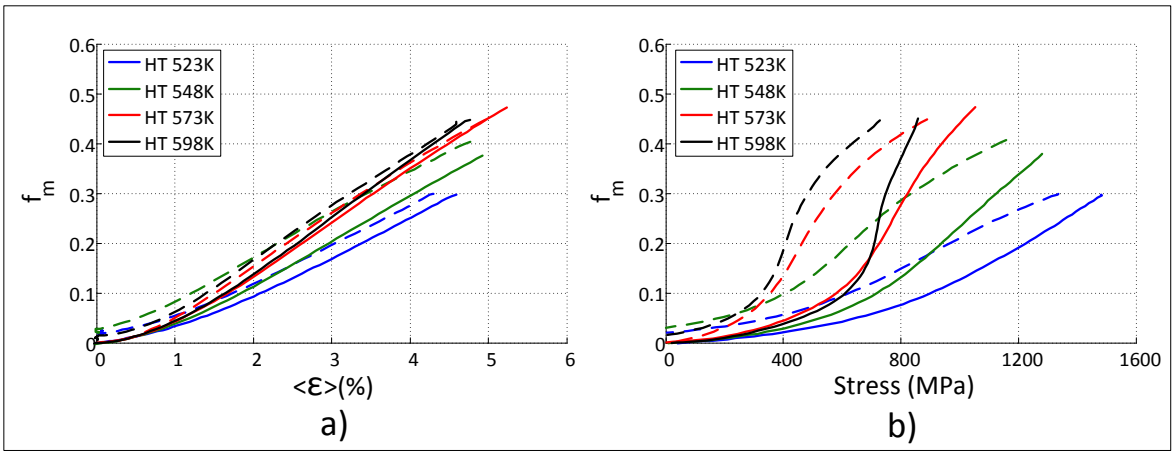

Figure 4.13: *Martensite fraction in function of strain (a) and stress (b) for all heat treated wires. Solid curves are for loading and dashed ones for unloading.*

The aforementioned behavior is then observed in Fig. 4.13 where at the same stress level, $800 MPa$ for example, the amount of martensite transformed in the wire $HT\,523K$ was $f_m^{HT\,523K} = 0.07$, $f_m^{HT\,548K} = 0.13$ for the $HT\,548K$, $f_m^{HT\,573K} = 0.27$ for the $HT\,573K$ and $f_m^{HT\,598K} = 0.38$ for the $HT\,598K$. Finally, despite the full superelastic loop, the $HT\,598K$ wire showed a martensite fraction maximum of $f_m^{HT\,598K} = 0.43$.

4.6 Conclusion

A thermomechanical investigation was performed on cold worked wires submitted to a heat treatment at four different temperatures: $523K$, $548K$, $573K$ and $598K$. Inconclusive DSC results were obtained for all heat treated wires since no thermal peaks were observed. Using an infrared thermal camera, uniform temperature profiles were obtained during tensile tests for all heat treated wires. With the increase of heat treatment temperature, the temperature variation of the wire during the tensile test increased.

Uniform strain fields were observed with digital image correlation (DIC) on all tensile tests. The uniformity on the temperature and strain profiles allowed a $0D$ approach for experimental data computing.

Through a heat balance applied on the experimental data, thermal power and thermal energy generated during the SIPT were obtained. A substantial increase on thermal power peak was observed rising from $1.1\,W/g$ for the wire $HT\,523K$ to $2.1\,W/g$ for the one $HT\,598K$. Also, the ratio between thermal power and mechanical power ($\dot{q}/P_{mech}$) increased from $\dot{q}/P_{mech} = 0.8$ to $\dot{q}/P_{mech} = 2.1$, for the wire $HT\,523K$ and $HT\,598K$, respectively.

Thermal energy also showed an important increase with the heat treatment temperatures. The wire $HT\,523K$ showed a thermal energy at the end of loading of $4.9\,J/g$ while the $HT\,598K$ presented a value of $8.2\,J/g$. Furthermore the hysteresis area of the stress strain curve increased from $1.0\,J/g$ for the wire $HT\,523K$ to $1.4\,J/g$ for the wire $HT\,598K$.

With the support of a thermodynamic framework, it was possible to estimate the specific latent heat of the $Ti50.8\%at.Ni$ wire during a stress induced martensitic transformation. Despite the differences on thermal energies shown for each heat treated wire, the specific latent heat obtained in the tensile tests showed a mean value with a rather small dispersion on loading. The obtained value were $\Delta H^{A-M}_{HT\,523K} = 19.6 \pm 0.3\,J/g$, $\Delta H^{A-M}_{HT\,548K} = 20.6 \pm 0.4\,J/g$, $\Delta H^{A-M}_{HT\,573K} = 19.6 \pm 0.7\,J/g$ and $\Delta H^{A-M}_{HT\,598K} = 19.6 \pm 0.4\,J/g$. During the unloading, the value obtained presented a decreasing behavior with the increase of HT temperature, they were $\Delta H^{M-A}_{HT\,523K} = 18.0 \pm 0.7\,J/g$, $\Delta H^{M-A}_{HT\,548K} = 17.9 \pm 0.8\,J/g$,$\Delta H^{M-A}_{HT\,573K} = 16.9 \pm 0.4\,J/g$ and $\Delta H^{M-A}_{HT\,598K} = 14.9 \pm 0.2\,J/g$. Values in the same range were found in literature for a fully annealed NiTi alloys tested via the DSC technique. Due to decreasing behavior during unloading the dissipated heat described as the difference between the specific latent heat on loading and unloading showed an increasing tendency. Such behavior was followed by the mechanical hysteresis showing rather the same values.

Moreover, it was possible to determine the martensite fraction for all the heat treated wires in function of strain and stress. It showed an important dependence with the heat treatment temperature. With the increase of the temperature heat treatment, more martensite was transformed for the same stress level. At approximately $800MPa$, the fraction of martensite transformed were: $f_m^{HT\,523K} = 0.07$, $f_m^{HT\,548K} = 0.13$, $f_m^{HT\,573K} = 0.27$ and $f_m^{HT\,598K} = 0.38$. Finally it was observed that for the $HT\,598K$ wire the maximum martensite fraction amount achieved was $f_m^{HT\,598K} = 0.43$, when it is usually assumed to be $f_m = 1$.

GENERAL CONCLUSION

This PhD thesis investigated the thermomechanical couplings associated with the tensile superelastic effect of a $Ti - 50.9\,at.\%\,Ni$ Shape Memory Alloy (SMA) nanocrystalline thin wire (diameter 0.5 mm), in a Cold Worked (CW) state. The wire was submitted to different heat treatment temperatures (HTT), ranging from 523 K to 598 K during 30 min. These heat treatments at low temperature promoted a fully superelastic loop without stress plateau and no Luders-like deformation. The main objectives were to measure and analyse the specific latent heat of phase transformation (ΔH_{tr}) and the martensite fraction (f_m) during a stress induced phase transformation (SIPT), for different HTT. In such a material, classic DSC tests show inconclusive results for the determination of ΔH_{tr}. To overcome this limitation, a method using digital image correlation (DIC) and thermal field measurement (TFM) associated with a thermodynamic analysis was proposed. These tasks were accomplished in several steps summarized in the following paragraphs.

The first chapter of this report presents a brief bibliography about the thermomechanical properties of the SMAs. Some potential engineering applications, using the effect of the thermomechanical coupling in superelasticity, are shown, as well as some experimental studies found in literature. A thermodynamic framework analysing the martensite transformation phenomenon is then given. Finally, this chapter discuss the influence: (1) of the microstructure on the superelasticity thermodynamic properties, (2) of the manufacturing process and heat treatment on thermomechanical responses.

The experimental aspects concerning the material, the applied heat treatments, the test procedure and the experimental issues are presented in chapter two. This chapter describes the methodology proposed to obtain and analyse the thermal and kinematic full field data.

Chapter three presents the results of the thermomechanical study of a NiTi wire, heat treated during 30 min at a single temperature (523 K), and submitted to a tensile loading. Thermal and mechanical powers are estimated from temperature variations and local strain fields measured with an infrared camera and a DIC system, respectively. The analysis of the thermal power shows that the phase transformation started since the beginning of deformation, rather than after reaching a critical stress, as it is usually described in literature.

Analysing these results, and using a thermodynamic framework based on the Gibbs free energy, the specific latent heat of phase transformation is determined during the direct (ΔH^{A-M}) and reverse (ΔH^{A-M}) phase transformations. The latent heat estimated during a SIPT is in good agreement with the ones given in the literature for a fully annealed $Ti - 50.9\,at.\%\,Ni$ alloy tested via DSC technique.

The martensite fraction f_m is also calculated in function of strain and stress. Variations of f_m up to 10% are estimated during the initial loading stage (before the upper plateau) and during the unloading (before the lower plateau) stage. This result ratifies the presence of phase transformation in these classical "elastic deformation stages". At the end of loading, a maximum of 45% of martensite fraction is obtained, for an imposed strain of 4.5%.

Chapter four studies the influence of HTT on the thermomechanical couplings observed during a SIPT on the same NiTi wire but submitted to four HTT (523 K, 548 K, 573 K and 598 K) during 30 min.

An increase of the magnitude of the thermal power and a decrease of the mechanical power were observed with an increase in HTT. Despite the differences between the obtained thermal powers, the specific latent heat values during loading (ΔH^{A-M}) show a rather small dispersion, around a mean value of 19.8 J/g. However, the specific latent heat values obtained during unloading (ΔH^{M-A}), show a decreasing trend with the increasing of HT temperature. Also f_m values, estimated for all HT wires at the same the same stress level, increase with the increase of HT temperature.

In general this work provided a method to determine the specific latent heat in SMAs which do not show any conclusive result when analyzed through DSC tests. It also contributed to give insights in the understanding of the thermomechanical couplings during a SIPT through the relation of the thermal and mechanical energies involved in the phenomenon.

PERSPECTIVES

A new field of investigation has been opened to study the thermomechanical behavior of superelastic Shape Memory Alloys. The used method allows the determination of the specific latent heat, as well as the amount of martensite transformation, using non contact measurements of temperature and displacement fields during a stress induced phase transformation.

As discussed in the present work, the specific latent heat is strongly dependent on the alloy composition. For binary NiTi Alloys the specific latent heat may vary from 10 J/g to 30 J/g. This variation is also strongly dependent on the composition for other ternary NiTi alloys (as NiTiV, NiTiCr, NiTiCu, etc.) or even for other SMA's compositions such as Cu based alloys (as CuAlMn, CuAlBe, CuAlNi). In this context the method used in this work could be applied to determine the specific latent heat in other compositions of superelastic SMA's.

Concerning the experimental analysis, thermal and mechanical results (i.e. powers and energies) are greatly sensitive to the geometry and size of the sample. From the thermal point of view, the determination of the τ_{eq} may be affected by the specimen size and geometry. This effect is due to the small thermal inertia of small specimens. In this context, several sizes of specimens could be used to take into account the geometry influence. From the mechanical point of view, the determination of the strain rate $\dot{\varepsilon}$ is also affected by small specimens when using the method of digital image correlation. In order to take into account this possible variation, larger specimens could be used. Also, a physical strain gauge attached to the specimen could be used.

Lastly, the determination of the specific latent heat during a stress induced phase transformation is very useful for elastocaloric cooling applications. With the use of this approach, more efficient devices can be designed with the determination of the amount of martensite phase transformation and thermal power and energies.

BIBLIOGRAPHY

Ahadi, A. and Q. Sun (2014). "Effects of grain size on the rate-dependent thermomechanical responses of nanostructured superelastic NiTi". In: *Acta Materialia* 76, pp. 186–197.

Ahadi, A., E Rezaei, and A Karimi Taheri (2012). "Effect of hot rolling on microstructure and transformation cycling behaviour of equiatomic NiTi shape memory alloy". In: *Mater. Sci. and Technol.* 28.000, pp. 727–732.

Alonso, T. (2015). *Caractérisation par essais DMA et optimisation du comportement thermomécanique de fils de NiTi - Application à une aiguille médicale pilotable.*

Álvarez-Alonso, P., C. O. Aguilar-Ortiz, E. Villa, A. Nespoli, H. Flores-Zúñiga, and V. A. Chernenko (2017). "Conventional and inverse elastocaloric effect in Ni-Fe-Ga and Ni-Mn-Sn ribbons". In: *Scripta Materialia* 128, pp. 36–40.

Amarante, F. P. and C. Cismasiu (2011). "Bridge hinge-restrainers built up of NiTi superelastic shape-memory alloys". In:

Antherieu, G. (2016). "L ' hypertrophie de la prostate et la ré- tention aiguë d ' urine : vers un stent urétral à base de bio-matériaux NiTi et silicone". PhD thesis.

Arbab-Chirani, R., V. Chevalier, S. Arbab-Chirani, and S. Calloch (2011). "Comparative analysis of torsional and bending behavior through finite-element models of 5 Ni-Ti endodontic instruments". In: *Oral Surgery, Oral Medicine, Oral Pathology, Oral Radiology and Endodontology* 111.1, pp. 115–121.

Balandraud, X., E. Ernst, and E. Sos (2005). "Monotone strain-stress models for shape memory alloys hysteresis loop and pseudoelastic behaviorx". In: *Zeitschrift fr angewandte Mathematik und Physik* 56.2, pp. 304–356.

Berthel, B., A. Chrysochoos, B. Wattrisse, and A. Galtier (2008). "Infrared image processing for the calorimetric analysis of fatigue phenomena". In: *Experimental Mechanics* 48.1, pp. 79–90.

Brinson, L. C., I. Schmidt, and R. Lammering (2004). "Stress-induced transformation behavior of a polycrystalline NiTi shape memory alloy: Micro and macromechanical investigations via in situ optical microscopy". In: *Journal of the Mechanics and Physics of Solids* 52.7, pp. 1549–1571.

Brown, L. C. (1981). "The Thermal Effect in Pseudoelastic Single Crystals of β-CuZnSn". In: *Metallurgical and Materials Transactions A* 12.8, pp. 1491–1494.

Chang, S., S. Wu, and G. Chang (2006). "Transformation sequence in severely cold-rolled and annealed Ti50Ni50 alloy". In: *Materials Science and Engineering: A* 438-440, pp. 509–512.

Chee Siong Loh, H. Yokoi, and T. Arai (2005). "New Shape Memory Alloy Actuator: Design and Application in the Prosthetic Hand". In: *2005 IEEE Engineering in Medicine and Biology 27th Annual Conference*. Vol. 7. 16360118. IEEE, pp. 6900–6903.

Chen, I.-W., Y.-H. Chiao, and K Tsuzaki (1985). "Statistics of martensitic nucleation". In: *Acta Metallurgica* 33.10, pp. 1847–1859.

Chrysochoos, A., H. Pham, and O. Maisonneuve (1996). "Energy balance of thermoelastic martensite transformation under stress". In: *Nuclear Engineering and Design* 162.1, pp. 1–12.

Chrysochoos, A, V Huon, F Jourdan, J.-M. Muracciote, R Peyroux, and B Wattrisse (2010). "Use of full-field digital image correlation and infrared thermography measurements for the thermomechanical analysis of material behaviour". In: *Strain* 46, pp. 117–130.

Chrysochoos, A. and H. Louche (2000). "An infrared image processing to analyse the calorific effects accompanying strain localisation". In: *International Journal of Engineering Science* 38.16, pp. 1759–1788.

Cismasiu, C. (2010). *Shape Memory Alloys*. Ed. by C. Cismasiu. Sciyo.

Cui, J., Y. Wu, J. Muehlbauer, Y. Hwang, R. Radermacher, S. Fackler, M. Wuttig, and I. Takeuchi (2012). "Demonstration of high efficiency elastocaloric cooling with large ΔT using NiTi wires". In: *Applied Physics Letters* 101.7, p. 073904.

Delobelle, V., D. Favier, and H. Louche (2013). "Heat Estimation from Infrared Measurement Compared to DSC for Austenite to R Phase Transformation in a NiTi Alloy". In: *Journal of Materials Engineering and Performance* 22.6, pp. 1688–1693.

Delobelle, V., D. Favier, H. Louche, and N. Connesson (2015). "Determination of Local Thermophysical Properties and Heat of Transition from Thermal Fields Measurement During Drop Calorimetric Experiment". In: *Experimental Mechanics* 55.4, pp. 711–723.

Delobelle, V. (2012). "Contribuitions à l'étude thermomécanique des alliages à memoire de forme NiTi et à la réalisation par soudage e matériaux architecturés NiTi". In:

Delpueyo, D., M. Grédiac, X. Balandraud, and C. Badulescu (2012). "Investigation of martensitic microstructures in a monocrystalline Cu-Al-Be shape memory alloy with the grid method and infrared thermography". In: *Mechanics of Materials* 45, pp. 34–51.

Delville, R., B. Malard, J. Pilch, P. Sittner, and D. Schryvers (2010). "Microstructure changes during non-conventional heat treatment of thin Ni–Ti wires by pulsed electric current studied by transmission electron microscopy". In: *Acta Materialia* 58.13, pp. 4503–4515.

Dieng, L., G. Helbert, S. A. Chirani, T. Lecompte, and P. Pilvin (2013). "Use of Shape Memory Alloys damper device to mitigate vibration amplitudes of bridge cables". In: *Engineering Structures* 56, pp. 1547–1556.

Favier, D., H. Louche, P. Schlosser, L. Orgéas, P. Vacher, and L. Debove (2007). "Homogeneous and heterogeneous deformation mechanisms in an austenitic polycrystalline Ti-50.8 at.% Ni thin tube under tension. Investigation via temperature and strain fields measurements". In: *Acta Materialia* 55.16, pp. 5310–5322.

Frenzel, J., A. Wieczorek, I. Opahle, B. Maaß, R. Drautz, and G. Eggeler (2015). "On the effect of alloy composition on martensite start temperatures and latent heats in Ni–Ti-based shape memory alloys". In: *Acta Materialia* 90, pp. 213–231.

Gheorghita, V., P. Gümpel, J. Strittmatter, C. Anghel, T. Heitz, and M. Senn (2013). "Using Shape Memory Alloys in Automotive Safety Systems". In: vol. 200. Lecture Notes in Electrical Engineering. Berlin, Heidelberg: Springer Berlin Heidelberg, pp. 909–917.

Glezer, A., E. Blinova, V. Pozdnyakov, and A. Shelyakov (2003). "Martensite Transformation in Nanoparticles and Nanomaterials". In: *Journal of Nanoparticle Research* 5.5/6, pp. 551–560.

Gur, S., S. K. Mishra, and G. N. Frantziskonis (2016). "Thermo-mechanical strain rate-dependent behavior of shape memory alloys as vibration dampers and comparison to conventional dampers". In: *Journal of Intelligent Material Systems and Structures* 27.9, pp. 1250–1264.

Hamilton, R. F., H. Sehitoglu, Y. Chumlyakov, and H. J. Maier (2004). "Stress dependence of the hysteresis in single crystal NiTi alloys". In: *Acta Materialia* 52.11, pp. 3383–3402.

He, Y. J. and Q. P. Sun (2010). "Frequency-dependent temperature evolution in NiTi shape memory alloy under cyclic loading". In: *Smart Materials and Structures* 19.11, p. 115014.

He, Y. and Q. Sun (2011). "On non-monotonic rate dependence of stress hysteresis of superelastic shape memory alloy bars". In: *International Journal of Solids and Structures* 48.11-12, pp. 1688–1695.

He, Y., H. Yin, R. Zhou, and Q. Sun (2010). "Ambient effect on damping peak of NiTi shape memory alloy". In: *Materials Letters* 64.13, pp. 1483–1486.

Kan, Q., C. Yu, G. Kang, J. Li, and W. Yan (2016). "Experimental observations on rate-dependent cyclic deformation of super-elastic NiTi shape memory alloy". In: *Mechanics of Materials* 97, pp. 48–58.

Khalil-Allafi, J. and B. Amin-Ahmadi (2009). "The effect of chemical composition on enthalpy and entropy changes of martensitic transformations in binary NiTi shape memory alloys". In: *Journal of Alloys and Compounds* 487.1-2, pp. 363–366.

Khmelevskaya, I., E. Ryklina, S. Prokoshkin, G. Markossian, E. Tarutta, and E. Iomdina (2008). "A shape memory device for the treatment of high myopia". In: *Materials Science and Engineering: A* 481-482, pp. 651–653.

Koike, J., D. M. Parkin, and M. Nastasi (1990). "Crystal-to-amorphous transformation of NiTi induced by cold rolling". In: *Journal of Materials Research* 5.07, pp. 1414–1418.

Lagoudas, D. C. (2008). *Shape Memory Alloys*. Texas, USA, p. 435.

Leo, P., T. Shield, and O. Bruno (1993). "Transient heat transfer effects on the pseudoelastic behavior of shape-memory wires". In: *Acta Metallurgica et Materialia* 41.8, pp. 2477–2485.

Li, C.-H., L.-J. Chiang, Y.-F. Hsu, and W.-H. Wang (2008). "Cold Rolling-Induced Multistage Transformation in Ni-Rich NiTi Shape Memory Alloys". In: *MATERIALS TRANSACTIONS* 49.9, pp. 2136–2140.

Louche, H. (1999). "Analyse pas thermographie infrarouge des effets dissipatifs de la localisation dans des aciers". PhD thesis, p. 272.

Louche, H. and A. Chrysochoos (2001). "Thermal and dissipative effects of accompanying Lüders band propagation". In: *Materials Science and Engineering A* 307.1-2, pp. 15–22.

Louche, H., P. Vacher, and R. Arrieux (2005). "Thermal observations associated with the Portevin-Le Châtelier effect in an Al-Mg alloy". In: *Materials Science and Engineering A* 404.1-2, pp. 188–196.

McCormick, P., Y. Liu, and S. Miyazaki (1993). "Intrinsic thermal-mechanical behaviour associated with the stress-induced martensitic transformation in NiTi". In: *Materials Science and Engineering: A* 167.1-2, pp. 51–56.

McNichols, J. L. and J. S. Cory (1987). "Thermodynamics of Nitinol". In: *Journal of Applied Physics* 61.3, pp. 972–984.

Messner, C., G. Reisner, Q. P. Sun, and E. Werner (2000). "On instabilities and autocatalytic effects associated with the nucleation of martensite bands in polycrystalline SMA flat tensile specimens". In: *Computational Materials Science* 19.1-4, pp. 313–319.

Miller, D. a. and D. C. Lagoudas (2001). "Influence of cold work and heat treatment on the shape memory effect and plastic strain development of NiTi". In: *Materials Science and Engineering: A* 308.1-2, pp. 161–175.

Mitwally, M. E. and M. Farag (2009). "Effect of cold work and annealing on the structure and characteristics of NiTi alloy". In: *Materials Science and Engineering: A* 519.1-2, pp. 155–166.

Miyazaki, S., T. Imai, K. Otsuka, and Y. Suzuki (1981). "Lüders-like deformation observed in the transformation pseudoelasticity of a TiNi alloy". In: *Scripta Metallurgica* 15.8, pp. 853–856.

Miyazaki, S., S. Kimura, K. Otsuka, and Y. Suzuki (1984). "The habit plane and transformation strains associated with the martensitic transformation in Ti-Ni single crystals". In: *Scripta Metallurgica* 18.9, pp. 883–888.

Mohd Jani, J., M. Leary, A. Subic, and M. a. Gibson (2013). "A review of shape memory alloy research, applications and opportunities". In: *Materials & Design* 56, pp. 1078–1113.

Mukherjee, K., S. Sircar, and N. B. Dahotre (1985). "Thermal effects associated with stress-induced martensitic transformation in a TiNi alloy". In: *Materials Science and Engineering* 74.1, pp. 75–84.

Orgéas, L. and D. Favier (1998). "Stress-induced martensitic transformation of a NiTi alloy in isothermal shear, tension and compression". In: *Acta Materialia* 46.15, pp. 5579–5591.

Ortín, J and A Planes (1988). "Thermodynamic analysis of thermal measurements in thermoelastic martensitic transformations". In: *Acta Metallurgica* 36.8, pp. 1873–1889.

Ortín, J. and A. Planes (1989). "Thermodynamics of thermoelastic martensitic transformations". In: *Acta Metallurgica* 37.5, pp. 1433–1441.

Ortín, J and A Planes (1991). "THERMODYNAMICS AND HYSTERESIS BEHAVIOUR OF THERMOELASTIC MARTENSITIC TRANSFORMATIONS". In: *Le Journal de Physique IV* 01.C4, pp. C4–13–C4–23.

Ossmer, H, F Lambrecht, M Gultig, C Chluba, E Quandt, and M Kohl (2014). "Evolution of temperature profiles in TiNi films for elastocaloric cooling". In: *Acta Materialia* 81, pp. 9–20.

Ossmer, H., S. Miyazaki, and M. Kohl (2015). "Elastocaloric heat pumping using a shape memory alloy foil device". In: *2015 Transducers - 2015 18th International Conference on Solid-State Sensors, Actuators and Microsystems, TRANSDUCERS 2015*, pp. 726–729.

Otsuka, K. and X. Ren (2005). "Physical metallurgy of Ti-Ni-based shape memory alloys". In: *Progress in Materials Science* 50.5, pp. 511–678.

Otsuka, K. and C. Wayman (1998). *Shape memory materials*. Vol. 1. Published by the press syndicate of the University of Cambridge.

Pan, Q. and C. Cho (2007). "The Investigation of a Shape Memory Alloy Micro-Damper for MEMS Applications". In: *Sensors* 7.9, pp. 1887–1900.

Pataky, G. J., E. Ertekin, and H. Sehitoglu (2015). "Elastocaloric cooling potential of NiTi, Ni2FeGa, and CoNiAl". In: *Acta Materialia* 96, pp. 420–427.

Patel, J. R. and M. Cohen (1953). "Criterion for the action of applied stress in the martensitic transformation". In: *Acta Metallurgica* 1.5, pp. 531–538.

Pelton, A. R., B. Clausen, and A. P. Stebner (2015). "In Situ Neutron Diffraction Studies of Increasing Tension Strains of Superelastic Nitinol". In: *Shape Memory and Superelasticity* 1.3, pp. 375–386.

Peterlechner, M., J. Bokeloh, G. Wilde, and T. Waitz (2010). "Study of relaxation and crystallization kinetics of NiTi made amorphous by repeated cold rolling". In: *Acta Materialia* 58.20, pp. 6637–6648.

Peyroux, R, A Chrysochoos, C Licht, and M Lobel (1998a). "Thermomechanical coupling and pseudoelasticity of shape memory alloys". In: *International Journal of Engineering Science* 36.4, pp. 489–509.

Peyroux, R., A. Chrysochoos, C. Licht, and M. Löbel (1998b). "THERMOMECHANICAL COUPLINGS AND PSEUDOELASTICITY OF SHAPE MEMORY ALLOYS". In: *International Journal of Engineering Science* 36.4, pp. 489–509.

Pieczyska, E. (2010). "Activity of stress-induced martensite transformation in TiNi shape memory alloy studied by infrared technique". In: *Journal of Modern Optics* 57.18, pp. 1700–1707.

Qian, S., Y. Wang, Y. Geng, J. Ling, J. Muehlbauer, Y. Hwang, R. Radermacher, and I. Takeuchi (2016a). "Experimental Evaluation of a Compressive Elastocaloric Cooling System". In: *16th International Refrigeration and Air Conditioning Conference at Purdue*, p. 2385.

Qian, S., Y. Geng, Y. Wang, J. Ling, Y. Hwang, R. Radermacher, I. Takeuchi, and J. Cui (2016b). "A review of elastocaloric cooling: Materials, cycles and system integrations". In: *International Journal of Refrigeration* 64, pp. 1–19.

Quan, G.-z., Y.-p. Mao, G.-s. Li, W.-q. Lv, Y. Wang, and J. Zhou (2012). "A characterization for the dynamic recrystallization kinetics of as-extruded 7075 aluminum alloy based on true stress–strain curves". In: *Computational Materials Science* 55, pp. 65–72.

Rittel, D. (1999). "On the conversion of plastic work to heat during high strain rate deformation of glassy polymers". In: *Mechanics of Materials* 31.2, pp. 131–139.

Rodriguez, C. and L. C. Brown (1980). "The thermal effect due to stress-induced martensite formation in -CuAlNi single crystals". In: *Metallurgical Transactions A* 11.1, pp. 147–150.

Roh, J.-H. (2014). "Thermomechanical Modeling of Shape Memory Alloys with Rate Dependency on the Pseudoelastic Behavior". In: *Mathematical Problems in Engineering* 2014, pp. 1–9.

Salzbrenner, R. and M. Cohen (1979). "On the thermodynamics of thermoelastic martensitic transformations". In: *Acta Metallurgica* 27.5, pp. 739–748.

Schlosser, P. (2008). "Influence of thermal and mechanical aspects on deformation behaviour of NiTi alloys". PhD thesis.

Schlosser, P., H. Louche, D. Favier, and L. Orgéas (2007). "Image Processing to Estimate the Heat Sources Related to Phase Transformations during Tensile Tests of NiTi Tubes". In: *Strain* 43.3, pp. 260–271.

Schmidt, I. (2006). "A Phenomenological Model for Superelastic NiTi Wires Based on Plasticity With Focus on Strain-Rate Dependency Caused by Temperature". In: *Journal of Engineering Materials and Technology* 128.3, p. 279.

Schmidt, M., A. Schütze, and S. Seelecke (2015a). "Scientific test setup for investigation of shape memory alloy based elastocaloric cooling processes". In: *International Journal of Refrigeration* 54, pp. 88–97.

Schmidt, M., J. Ullrich, A. Wieczorek, J. Frenzel, A. Schütze, G. Eggeler, and S. Seelecke (2015b). "Thermal Stabilization of NiTiCuV Shape Memory Alloys: Observations During Elastocaloric Training". In: *Shape Memory and Superelasticity*, pp. 132–141.

Schmidt, M., S.-M. Kirsch, S. Seelecke, A. Schütze, and S. Seelecke (2016). "Elastocaloric Cooling: from Fundamental Thermodynamics to Solid State Air Conditioning". In: *Science and Technology for the Built Environment* 22.5, pp. 475–488.

Sergueeva, A., C Song, R. Valiev, and A. Mukherjee (2003). "Structure and properties of amorphous and nanocrystalline NiTi prepared by severe plastic deformation and annealing". In: *Materials Science and Engineering: A* 339.1-2, pp. 159–165.

Shaw, J (1995). "Thermomechanical aspects of NiTi". In: *Journal of the Mechanics and Physics of Solids* 43.8, pp. 1243–1281.

Shaw, J. A. and S. Kyriakides (1997a). "Initiation and propagation of localized deformation in elasto-plastic strips under uniaxial tension". In: *International Journal of Plasticity* 13.10, pp. 837–871.

Shaw, J. and S Kyriakides (1997b). "On the nucleation and propagation of phase transformation fronts in a NiTi alloy". In: *Acta Materialia* 45.2, pp. 683–700.

Shi, X., L. Cui, D. Jiang, C. Yu, F. Guo, M. Yu, Y. Ren, and Y. Liu (2014). "Grain size effect on the R-phase transformation of nanocrystalline NiTi shape memory alloys". In: *Journal of Materials Science* 49.13, pp. 4643–4647.

Sittner, P, Y Liu, and V Novak (2005). "On the origin of Lüders-like deformation of NiTi shape memory alloys". In: *Journal of the Mechanics and Physics of Solids* 53.8, pp. 1719–1746.

Šittner, P., M. Landa, P. Lukáš, and V. Novák (2006). "R-phase transformation phenomena in thermomechanically loaded NiTi polycrystals". In: *Mechanics of Materials* 38.5-6, pp. 475–492.

Šittner, P., L. Heller, J. Pilch, C. Curfs, T. Alonso, and D. Favier (2014). "Young's modulus of austenite and martensite phases in superelastic NiTi wires". In: *Journal of Materials Engineering and Performance* 23.7, pp. 2303–2314.

Stebner, A. P., H. M. Paranjape, B. Clausen, L. C. Brinson, and A. R. Pelton (2015). "In Situ Neutron Diffraction Studies of Large Monotonic Deformations of Superelastic Nitinol". In: *Shape Memory and Superelasticity* 1.2, pp. 252–267.

Sun, Q. P. and Z. Q. Li (2002). "Phase transformation in superelastic NiTi polycrystalline micro-tubes under tension and torsion - From localization to homogeneous deformation". In: *International Journal of Solids and Structures* 39, pp. 3797–3809.

Tsuchiya, K., M. Inuzuka, D. Tomus, A. Hosokawa, H. Nakayama, K. Morii, Y. Todaka, and M. Umemoto (2006). "Martensitic transformation in nanostructured TiNi shape memory alloy formed via severe plastic deformation". In: *Materials Science and Engineering: A* 438-440, pp. 643–648.

Tušek, J., K. Engelbrecht, L. P. Mikkelsen, and N. Pryds (2015). "Elastocaloric effect of Ni-Ti wire for application in a cooling device". In: *Journal of Applied Physics* 117.12.

Tušek, J., K. Engelbrecht, and N. Pryds (2016a). "Elastocaloric effect of a Ni-Ti plate to be applied in a regenerator-based cooling device". In: *Science and Technology for the Built Environment* 22.5, pp. 489–499.

Tušek, J., K. Engelbrecht, L. Mañosa, E. Vives, and N. Pryds (2016b). "Understanding the Thermodynamic Properties of the Elastocaloric Effect Through Experimentation and Modelling". In: *Shape Memory and Superelasticity* 2.4, pp. 317–329.

Waitz, T, K Tsuchiya, T Antretter, and F. D. Fischer (2009). "Phase Transformations of Nanocrystalline Martensitic Materials". In: *MRS Bulletin* 34.11, pp. 814–821.

Wollants, P, J. Roos, and L Delaey (1993). "Thermally- and stress-induced thermoelastic martensitic transformations in the reference frame of equilibrium thermodynamics". In: *Progress in Materials Science* 37.3, pp. 227–288.

Wu, Y., E. Ertekin, and H. Sehitoglu (2017). "Elastocaloric cooling capacity of shape memory alloys – Role of deformation temperatures, mechanical cycling, stress hysteresis and inhomogeneity of transformation". In: *Acta Materialia* 135, pp. 158–176.

Xiao, Y., P. Zeng, and L. Lei (2017). "Grain size effect on mechanical performance of nanostructured superelastic NiTi alloy". In: *Materials Research Express*.

Xie, X., Q. Kan, G. Kang, F. Lu, and K. Chen (2016). "Observation on rate-dependent cyclic transformation domain of super-elastic NiTi shape memory alloy". In: *Materials Science and Engineering A* 671, pp. 32–47.

Yang, S., J. Han, and I. Lee (2006). "Characteristics of smart composite wing with SMA actuators and optical fiber sensors". In: *International Journal of Applied Electromagnetics and Mechanics* 23, pp. 177–186.

Yin, H. and Q. Sun (2012). "Temperature Variation in NiTi Shape Memory Alloy During Cyclic Phase Transition". In: *Journal of Materials Engineering and Performance* 21.12, pp. 2505–2508.

Yin, H., Y. He, and Q. Sun (2014). "Effect of deformation frequency on temperature and stress oscillations in cyclic phase transition of NiTi shape memory alloy". In: *Journal of the Mechanics and Physics of Solids* 67, pp. 100–128.

Yu, C., B. Aoun, L. Cui, Y. Liu, H. Yang, X. Jiang, S. Cai, D. Jiang, Z. Liu, D. E. Brown, and Y. Ren (2016). "Synchrotron high energy X-ray diffraction study of microstructure evolution of severely cold drawn NiTi wire during annealing". In: *Acta Materialia* 115, pp. 35–44.

Zaera, R., J. A. Rodríguez-Martínez, A. Casado, J. Fernández-Sáez, A. Rusinek, and R. Pesci (2012). "A constitutive model for analyzing martensite formation in austenitic steels deforming at high strain rates". In: *International Journal of Plasticity* 29.1, pp. 77–101.

Zaera, R., J. A. Rodríguez-Martínez, and D. Rittel (2013). "On the Taylor-Quinney coefficient in dynamically phase transforming materials. Application to 304 stainless steel". In: *International Journal of Plasticity* 40, pp. 185–201.

Zhang, X., P. Feng, Y. He, T. Yu, and Q. Sun (2010). "Experimental study on rate dependence of macroscopic domain and stress hysteresis in NiTi shape memory alloy strips". In: *International Journal of Mechanical Sciences* 52.12, pp. 1660–1670.

Zhu, S. and Y. Zhang (2007). "A thermomechanical constitutive model for superelastic SMA wire with strain-rate dependence". In: *Smart Materials and Structures* 16.5, pp. 1696–1707.